SAPIENZA
UNIVERSITÀ DI ROMA

Geolocating Low-Earth-Orbit satellite data from next-generation millimeter-wave radiometers using natural targets

DOTTORATO DI RICERCA - PHD IN INFORMATION AND COMMUNICATIONS TECHNOLOGIES (ICT)

Dipartimento di Ingegneria dell'Informazione, Elettronica e Telecomunicazioni
Curriculum: Radar and Remote sensing
Ciclo: XXXIII

Candidate
Mario Papa

Advisor
Frank Silvio Marzano

Academic Year 2019/2020

Abstract - The main goal of this work is to perform the geolocation error assessment of the channel imagery at 183.31 GHz of the Special Sensor Microwave Imager/Sounder (SSMIS). The frequency around 183.31 GHz still represents the highest channel frequency of current spaceborne microwave and millimeter-wave radiometers. The latter will be extended to frequencies up to 664 GHz, as in the case of EUMETSAT Ice Cloud Imager (ICI). This use of submillimeter observations unfortunately prevents a straightforward geolocation error assessment using landmark-based techniques. This work uses SSMIS data at 183.31 GHz as a submillimeter proxy to identify the most suitable targets for geolocation error validation in very dry atmospheric conditions, as suggested by radiative transfer modeling. Using a yearly SSMIS dataset, 3 candidates landmark targets are selected: i) high-altitude lakes and high-latitude bays using a coastline reference database; ii) Antarctic ice shelves and Arctic shorelines using coastlines derived from Sentinel-1 Synthetic Aperture Radar (SAR) imagery; iii) high altitude mountains using digital elevation model as reference. Data processing is carried out by using spatial cross-correlation methods in the spatial frequency domain and performing a numerical sensitivity analysis to contour displacement. Cloud masking, based on a fuzzy-logic approach, is applied to automatically selected clear-air days. Results show that the average geolocation error is about 6.2 km for mountainous lakes and sea bays and 5.4 km for ice shelves, respectively, with a standard deviation of about 2.7 and 2.0 km. Results are in line with SSMIS previous estimates, whereas annual clear-air days are about 10% for mountainous lakes and sea bays and 18% for ice shelves. The second goal of this work is to investigate ICI channels, focusing on 243 GHz at horizontal polarization (ICI-4). The results of the simulations using radiative transfer model and artificial neural network (ANN) confirm that ICI-4 will be the best candidate to validate the geolocation of the future ICI radiometer. At 243 GHz the atmosphere is less opaque and the surface could be more visible with respect to other frequencies. This work proposes an artificial neural network to reconstruct the 243 GHz starting from real data at 150 GHz and 183 GHz. ANN provides an average value of about 5.8 km with a standard deviation of about 2.7 km. These numbers are in line with those obtained for 183 GHz, but at 243 GHz the number of images that contains visible surface targets are much more with respect to 183 GHz.

INDEX

1. INTRODUCTION

The next generation of sub-millimetre wave radiometers will encompass the EPS-SG Ice Cloud Imager (ICI) mission, a sub-millimetre (sub-mm) wave conical imager that is part of the EUMETSAT Polar System – Second Generation (EPS-SG) [1],[2] system. ICI will be on board of the Metop-SG satellite B series, to span a total operational lifetime over 21 years. ICI will represent a very important source of data for weather and climate applications. Its channels from 183.31 to 664 GHz will provide observations of ice clouds, supporting the validation and improvement of ice microphysics models adopted within numerical weather prediction (NWP) and climate models [3]. The use of sub-mm frequencies for observation of cloud ice properties has been investigated for more than two decades, e.g. [4]-[8]. In this respect, being the first operational radiometer with sub-millimeter channels, ICI is opening new application domains, but also new technological and technical issues.

Much experience has been accumulated so far on the geolocation error validation for satellite-based microwave radiometers at lower microwave frequencies (10-50 GHz, outside the absorption bands) by exploiting their strong difference in terms of surface emissivity between land and ocean. Global-scale coastlines are used as surface landmarks with a significant contrast in terms of measured brightness temperature (BT). Comparing the latter with a reference coastline database [9], it is possible to assess the spaceborne sensor geolocation error. In [9], Purdy et al. compared the shoreline obtained from WindSat satellite imagery with the World Vector Shoreline Data Bank II (WVS II). The position of the coastline is obtained taking the peak of the first derivative of radiometric data along scan and cross scan direction, after a cubic spline interpolation to obtain a more smoothed curve. Poe et al. [10] applied a similar method on Special Sensor Microwave Imager/Sounder (SSMIS) using data provided by spacecraft F-16. To assess the geolocation error of AMSR-E at 89 GHz, Wiebe et al [11] and Heygster et al. [12], exploited the fact that, when geolocation errors are present, the projected footprints have different shifts considering ascending or descending swaths. These differences are high along coastlines, optimizing the geolocation by retrieving the offset parameters that minimize the absolute values of the differences.

Berg et al. [13] used the BT difference between ascending and descending swaths to obtain the attitude error for SSM/I spacecraft. Bellerby et al. [14] also had a coastal-zone technique for attributing BT from the SSMI. Finally, Moradi et al. [15] corrected the pitch, yaw and roll angles for Advanced Microwave Sounding Unit (AMSU) and Microwave Humidity Sounders (MHS) minimizing the differences in brightness temperature between ascending and descending

swathes. Along coastlines, the measured signal consists of radiation received from both land and water surfaces and Bennartz [16] proposed to use a high-resolution land–sea mask to infer the fraction of water surface for each measurement. He has developed a method to validate the geolocation accuracy using the convolution of land-sea masks that allows for channels that are sensitive to land/sea contrast. Han et al. [17] adapted this so-called "Land/sea Fraction Method" for the NOAA 16-18 satellites and also for ATMS on SNPP.

At frequencies beyond 150 GHz, the gaseous absorption can be so strong that the atmospheric transmittance, even in clear air, tends to be nearly zero. Moreover at sub-mm frequencies the simulated emissivity of the surface water increases with frequency reaching values up to 0.65 around 400 GHz for horizontal polarization, surface winds around 20 m/s and 50° incidence angle [18]. Therefore, the BT contrast between surface water and land bodies significantly diminishes thus preventing conventional geolocation validation approaches based on surface landmarks. A way to circumvent these issues is to select areas (and periods) with very low atmospheric water vapor concentration. Such surface landmarks, which should also exhibit a relatively large edge to be useful for geolocation assessment, are quite rare on the Earth planet.

Within the open issues above mentioned, the goals of this work are:

i) to exploit current spaceborne radiometric channels around 183.31 GHz to experimentally look for water coastline and high-altitude surface targets that can be used for geolocation purposes;

ii) to propose landmark reference contours extracted not only from cartographic databases, but also from high-spaceborne resolution synthetic aperture (SAR) radar imagery. At 183-GHz frequency, useful surface landmarks can be found in very dry atmospheric conditions such as the polar Arctic and Antarctic areas in their winter time. In particular, the Antarctic region can provide relatively long edges less affected by the sea-ice formation. Polar regions are also very frequently sampled by Sun-synchronous satellites thus offering a larger set of observations with respect to other regions, a feature quite critical for SAR missions.

iii) to find a relation between different channels in order to simulate 243 GHz starting from real images at 150 GHz and 183 GHz.

In order to satisfy these objectives, we have organized the work as follows. In chapter 2, we give a general overview of the principal aspects of earth observation and radiative transfer theory.

Chapter 3 contains general information about the proposed methodology, including the criteria regarding the search of landmark targets and the cloud-masking defuzzification step to filter the available dataset from cloud coverage contamination. In addition it describes the 9 selected targets, among

the list of those which have been explored, by dividing the list for the northern and southern hemisphere in order to guarantee a good temporal coverage during the driest seasons. For each target this section resumes the results, using data from SSMIS channel at 183 GHz, in terms of mean value and standard deviation of the geolocation error both in northern hemisphere and southern hemisphere.

Chapter 4 approaches the problem of the sensitivity analysis of the proposed geolocation error assessment methodology to the most critical free parameters as a proxy to the error budget estimate. The latter, as a matter of fact, is not easily defined for the lack of an absolute reference (we are here estimating not the geolocation error but its accuracy or the error of the geolocation error correction procedures). Finally, chapter 3 aims at evaluating how the analysis, carried out using SSMIS channel at 183 GHz, can be extended to ICI channels at 183 GHz, 243 GHz and beyond if possible. The discussion uses both an analysis of SSMIS imagery at 150 GHz and 183 GHz and a radiative transfer simulation of brightness temperatures and slant-path attenuation from available radiosounding profiles and from ERA5 reanalysis atmospheric profiles near the selected targets.

At the end, chapter 5 draws the main conclusions and paves the way to the geolocation error assessment for ICI channels using the landmark targets.

CHAPTER 2

2. PASSIVE REMOTE SENSING FUNDAMENTALS

This chapter is devoted to the description of the atmosphere and some basic concepts of electromagnetic waves. In addition it provides a characterization of the radiative transfer equation and its solution. The final part describes microwave radiometers.

2.1 Basic concepts

The Sun provides the main part of the electromagnetic radiation arriving on the Earth. The atmosphere absorbs and/or scatters a part of this electromagnetic radiation and the other part is transmitted to Earth's surface. Also at the Earth's surface it is scattered and absorbed. This last part is transformed into thermal energy with consequent increase of surface temperature. In the following sub-section, to understand the thermal electromagnetic energy radiated by the bodies it is necessary to introduce radiometry. field of science that studies the thermal electromagnetic energy radiated by the bodies. Instead, the radiometers are the instruments that measure the power emitted by a body.

2.1.1 Electromagnetic waves

The electromagnetic (EM) waves, composing the electromagnetic radiation, can be imagined as a self-propagating transverse oscillating wave of electric and magnetic fields. Fig. 2.1.1.1 shows a plane linearly polarized EM wave propagating along the x axis. The electric field is in a vertical plane (*z axis*) and the magnetic field in a horizontal plane (*y axis*).

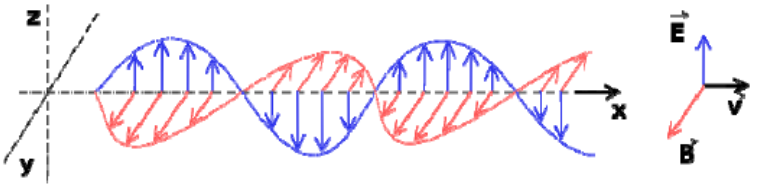

Figure 2.1.1.1 Atmospheric layers.

Considering a monochromatic plane wave of frequency f e pulsation $\omega = 2\pi f$, travelling along x, it is possible to express it as follows:

$$\overline{E}(x,t) = \left|\overline{E}_0\right| \hat{z}\, e^{-\alpha x} cos(\omega t - \beta x) = Re[\overline{E}_0\, e^{j(\omega t - \beta x)} e^{-\alpha x}] \qquad (2.1.1.1)$$

where:

- $\left|\overline{E}_0\right| \hat{z}$ is the polarization vector [V/m]
- β : propagation constant [m^{-1}]
- α : specific attenuation constant [m^{-1}]

The phase velocity can be written as follows:

$$\omega\, dt - \beta\, dz = 0 \Rightarrow u = \frac{dz}{dt} = \frac{\omega}{\beta} = \frac{2\pi f}{\beta} = \frac{2\pi f}{2\pi/\lambda} = \lambda f \qquad (2.1.1.2)$$

Note that the electric field, can be divided in two orthogonal polarization:

$$\overline{E}(x,t) = \overline{E}_h(x,t) + \overline{E}_v(x,t) \qquad (2.1.1.3)$$

It is also possible to define the Poynting Vector defined in Eq. 2.1.1.4:

$$\overline{P} = \frac{1}{2}\, \overline{E}\, x\, \overline{H} \qquad (2.1.1.4)$$

where $\overline{H}$ is the magnetic field. The real part or the Poynting vector is the power density P(W/m^2) transported by EM. Fig. 2.1.1.2 shows the electromagnetic spectrum.

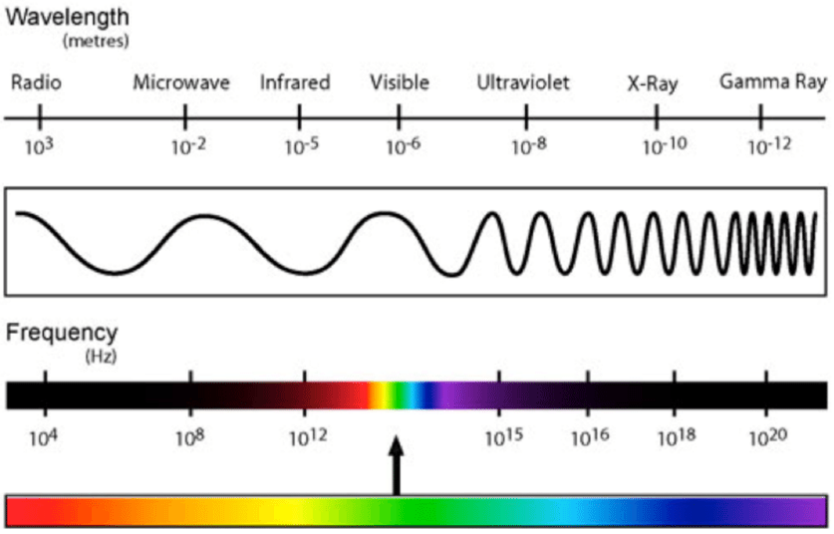

Figure 2.1.1.2 Electromagnetic spectrum

2.1.2 Atmospheric structure and composition

The atmospheric pressure and density decrease approximately exponentially with increasing height. The same happens to the water vapor density, although its variation with height is somewhat irregular and strongly dependent on time of day, season, geographic location, and atmospheric activity. On the other hand, the variation of atmospheric temperature with height exhibits a cyclic pattern, which can be used to subdivide the Earth's atmosphere into different atmospheric layers according to their thermal structure [19]. The Figure 2.1.2.1 shows the U. S. Standard Atmosphere atmospheric model, which describes the variation with height of atmospheric parameters of a "standard" or "reference" atmosphere and defines the atmospheric layers.

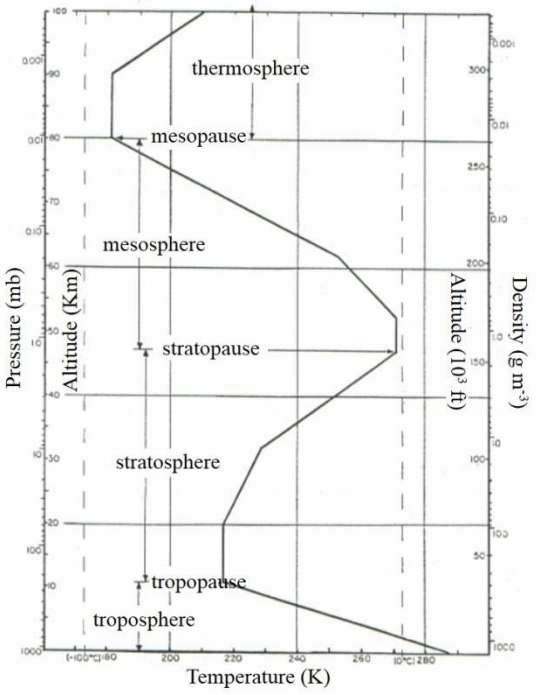

Figure 2.1.2.1 Atmospheric layers.

The boundaries of each atmospheric layer or shell are usually defined by the change in sign of the temperature gradient with height, dT/dz, where T is the atmospheric temperature and z is the geometrical height. The layers are characterized as follows.

The lowermost layer is the troposphere where dT/dz ≈ -6.5 $\frac{K}{km}$. At its upper boundary, the tropopause, the temperature's gradient changes sharply to zero. The height of the tropopause varies with latitude, season and weather activity. Generally, it is between 8 and 10 km in arctic regions in winter and between 16 and 18 km in the tropical and equatorial regions.

The second layer is the stratosphere, which goes from the tropopause to the stratopause, at a height of about 47 km. In the first 10 km of the stratosphere, the temperature is approximately constant and then increases with height with two different gradients: dT/dz ≈ 1 $\frac{K}{km}$ between 20 and 32 km and dT/dz ≈ 2.8 $\frac{K}{km}$ between 32 and 47 km above sea level. According to the U. S. Standard Atmosphere, the atmospheric temperature at the stratopause is about 270.5 K.

The third layer, which goes from the stratopause to the mesopause, at a height of about 80 to 90 km, is the mesosphere. At the mesopause the temperature reaches its lowest value of about 183 K. The atmospheric

composition and the molecular weight of air are approximately constant up to the mesopause. Above it there is the last layer, the thermosphere and no upper limit is defined for the thermosphere.

According to the concepts just exposed, we can point out the models in Table 2.1.2.1 for the profiles of the meteorological variables [20]. The profile of each variable is function of z, which is the height above sea level (in km), and of the value of the variable at sea-level (in this case, we consider the values used by the U. S. Standard Atmosphere):

Table 2.1.2.1 Model for vertical profile of several atmospheric variables

Temperature profile, T(z) [K]	
$T(z) = T(0) + g_T z$	when $0 \leq z \leq 11\ km$
$T(z) = T(11)$	when $11 \leq z \leq 20\ km$
$T(z) = T(11) + (z - 20)$	when $20 \leq z \leq 32\ km$
where: T(0) is the sea level atmospheric temperature (288.15 K) T(11) is the atmospheric temperature at z = 11 km, in kelvins. g_T is the gradient of the temperature in the troposphere (- 6.5 $\frac{K}{km}$).	
Density profile of dry air, $\rho_a(z)$ [$\frac{kg}{m^3}$]	
$\rho_a(z) = \rho_a(0)\, e^{(-z/H_1)}$	
where: $\rho_a(0)$ = 1.225 $\frac{kg}{m^3}$ is the density of air at sea level H_1 = 9.5 km is the density scale height	
Pressure profile, p(z) [Pa]	
$P(z) = P(0)\, e^{(-z/H_2)}$	
where: $P(0)$ = 1013.25 mbar is sea level pressure H_2 = 7.7 km is the density scale height	

Except for water-vapor variations, the atmospheric composition can be considered constant up to 90 km above sea level (Table 2.1.2.2). The principal constituent of the atmosphere are:

- Gas mixture (dry component of air): Table 2.1.2.2 reports the sea-level composition of clean air containing no water vapor used by the U. S. Standard Atmosphere;
- H_20 at gaseous state (water vapor);
- Hydrosols (water drops constituting clouds, haze and fog);
- Aerosols (water-soluble or silicate-based);
- Liquid or iced precipitating hydrometeors in rainy clouds (rain drops, precipitating ice, graupel, snow);
- Non-precipitating ice (convective clouds and cirrus)

Table 2.1.2.2 Normal composition of clean, dry atmospheric air near sea level [19]

Constituent gas	Gas symbol	Content (% by volume)	Molecular weight
Nitrogen	N_2	78.084	28.0134
Oxygen	O_2	20.9476	31.9988
Argon	Ar	0.934	39.948
Carbon dioxide*	CO_2	0.0314	44.00995
Neon	Ne	0.001818	20.183
Helium	He	0.000524	4.0026
Krypton	Kr	0.000114	83.80
Xenon	Xe	0.0000087	131.30
Hydrogen	H_2	0.00005	2.01594
Methane*	CH_4	0.0002	16.04303
Nitrous oxide	N_2O	0.00005	44.0128
Ozone*	O_3	Summer: 0 to 0.000007 Winter: 0 to 0.000002	47.9982 47.9982
Sulfur dioxide*	SO_2	0 to 0.0001	64.0628
Nitrogen dioxide*	NO_2	0 to 0.000002	46.0055
Ammonia*	NH_3	0 to trace	17.03061
Carbon monoxide	CO	0 to trace	28.01055
Iodine	I_2	0 to 0.000001	253.8088

*The content of these gases may undergo significant variations from time to time or from place to place relative to the normal

2.2 Radiative transfer through atmosphere

Each body with a temperature T > 0 K, radiates incoherent electromagnetic energy in each direction and frequency band of the electromagnetic spectrum.

The brightness or radiance is a quantity used to quantify the incoherent electromagnetic energy emitted by a body. Consider a transmitting antenna at a distance R from a receiving antenna of equivalent area $E_r(\theta,\varphi)$ and oriented each other in the maximum directivity direction. Supposing to be in the far field region, if P_i is the power density incident on the receiving antenna and (θ,φ) is the direction of propagation, the received power is:

$$W_r = P_i(R,\theta,\varphi)A_r \qquad [W] \tag{2.2.1}$$

We can define the brightness B as the distribution, within the solid angle $d\Omega_t$, of the intensity of the poynting vector:

$$B(\theta,\varphi) = dP_i(R,\theta,\varphi)/d\Omega_t \qquad [W\ sr^{-1}m^{-2}] \tag{2.2.2}$$

At the microwave frequencies, the brightness can be replaced with the brightness temperature T_B of a body:

$$T_B(\theta,\varphi) = eT \qquad [K] \tag{2.2.3}$$

where e is the emissivity of the body [adim]: $0 \leq e \leq 1$. The emissivity depends on the observation angle, frequency, surface characteristics and composition of the body. In conditions of local thermodynamic equilibrium for a body, its emissivity is equal to its absorption: the body emits as much radiation is absorbed.

2.2.1 Wave-matter interaction coefficient

For frequencies f > 5-10 GHz, is affected by:

i) scattering due to precipitating or suspended hydrometeors,

ii) absorption and emission effects due to gases and liquid water clouds and.

As concerning the scattering, we can distinguish three phenomena:

- *Raman scattering*: the scattered radiation exhibits a frequency shift with respect to the incident radiation; the shift depends on the characteristics of the scattering molecules

- *Mie scattering*: the scattered wave has the same frequency of the incident wave; it happens when the dimension of the scattering particles are of the same order of magnitude of the incident wavelength.

- *Rayleigh scattering*: it is a particular case of the Mie scattering for particles with dimensions much smaller than the incident wavelength (of the order of λ-4).

As concerning the gas absorption and emission, we have the atmospheric absorption coefficient that describes the energy transfer from the wave to the molecule. The acquired energy makes the molecule go to a higher energy level and then return to the lower energy level by emitting energy in the form of an electromagnetic wave. In the condition of local thermodynamic equilibrium, the absorption and emission coefficients have the same value. As we can see from the Fig. 2.2.1.1., in the microwave region, the water vapor and oxygen absorption lines provide some atmospheric windows (or transmission windows) around 35, 94 and 140 GHz. A last, less pronounced window, is around 225 GHz.

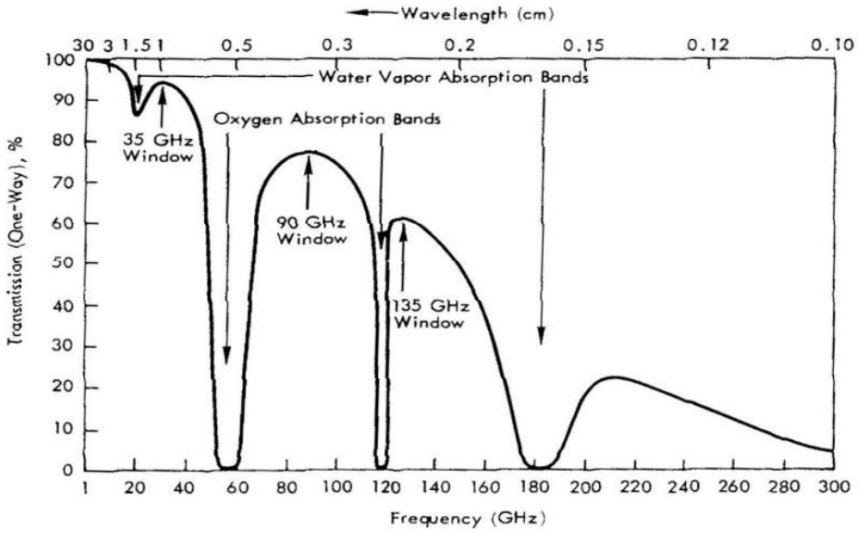

Figure 2.2.1.1 Atmospheric transmissivity: three transmission windows around 35, 94 and 140 GHz. A last, less pronounced window, is around 225 GHz.

The radiative transfer theory starting point is the energy transportation through a medium of scattering particles randomly distributed. The basic concepts are:

- the polarization effects of the electromagnetic wave and the relationships between the phases of the signals are considered secondary with respect to energy flux (scalar formulation);
- the contributions to the electromagnetic field are assumed to be uncorrelated, thus the relative power are added together;
- the radiative transfer theory describes the spatial evolution of the radiation intensity (described in terms of brightness or radiance), which propagates in an absorbing, emitting and scattering medium;

- the brightness (or radiance) is the instantaneous power that passes through a direction, per unit of area orthogonal to the propagation direction and per unit of solid angle.

Let us consider an infinitesimal volume dV of length *dr*, dissipating and scattering, and an incident power density P_i (cf. Figure 2.2.1.2). If *dWs* and *dWa* are the scattered and absorbed power by the little volume, we can define the extinguished power as:

$$dW_e = dW_s + dW_a \qquad [W] \tag{2.2.1.1}$$

In the radiative transfer theory, we can define the following coefficients:

- *Absorption coefficient* k_a [m^{-1}]: describes the brightness attenuation due to the absorption:

$$k_a(\theta_i, \varphi_i; p_i) = \frac{dW_a}{dV\, P_i(\theta_i, \varphi_i; p_i)} \qquad [m^{-1}] \tag{2.2.1.2}$$

- *Scattering coefficient* k_s [m^{-1}]: describes the brightness attenuation due to the scattering:

$$k_s(\theta_i, \varphi_i; p_i) = \frac{dW_s}{dV\, P_i(\theta_i, \varphi_i; p_i)} \qquad [m^{-1}] \tag{2.2.1.3}$$

- *Extinction coefficient* k_e [m^{-1}]: describes the brightness attenuation due to both the scattering and the absorption effects:

$$k_e = k_a + k_s \qquad [m^{-1}] \tag{2.2.1.4}$$

where (θ_i, φ_i) is the incident direction and p_i is the incident polarization.

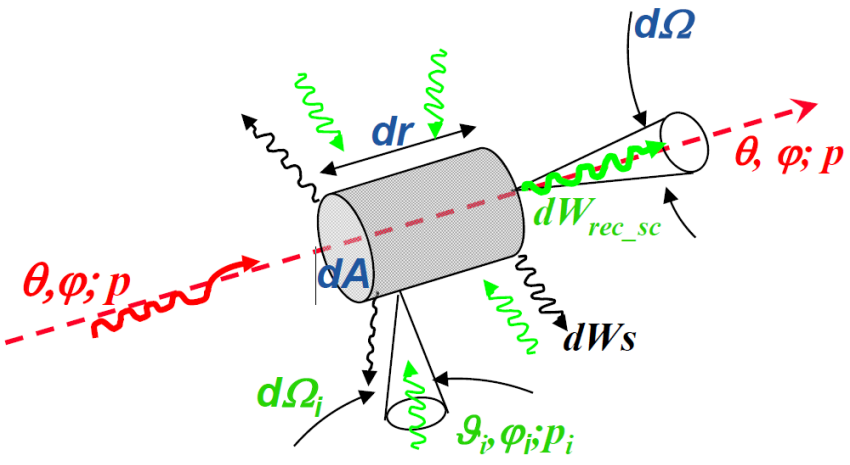

Figure 2.2.1.2 Infinitesimal volume dV of length dr, dissipating and scattering: $(\theta_{i/s}, \varphi_{i/s})$ and $p_{i/s}$ are the incident/scattering direction and the incident/scattering polarization within the solid angle $d\Omega_{i/s}$ [21].

2.2.2 Radiative transfer equation and solutions

The radiative transfer equation (RTE) is an integro-differential equation that allows computing the brightness increment *dB(r)* in the propagating direction *r*.

Let us consider a small cylindrical volume, aligned with *r*, of section area *dA* and length *dr* as in the Fig. 2.2.2.1

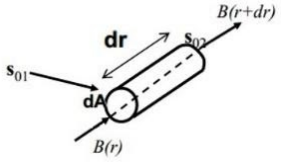

Figure 2.2.2.1: Small cylindrical volume, aligned with the propagating direction r, of section area dA and length dr. $r=rs_{02}$, where s_{02} is the unit vector of the observing direction. s_{01} is the generic incident direction for the radiation coming from directions different from the observed direction r [21].

We must consider three contributions:

- negative increment (*extinction*), dB_e: is the loss in brightness by extinction due to propagation over the thickness *dr*. The energy lost from the incident radiation may have been absorbed by the volume, or scattered, or both. By *absorption loss*, we mean that the energy is transformed into another form of energy (such as heat); by *scattering loss*, we mean that the energy is caused to travel in different directions than the direction of the incident radiation:

$$dB_e = k_e B(r) dr \qquad (2.2.2.1)$$

- positive increment due to *recovery in scattering,* dB_s: a part of the radiation incident on the volume comes from the surrounding volumes and from directions that are different from the observed direction ***r*** (in the Figure 2.2.2.1 we consider the generic direction defined by the unit vector $\boldsymbol{s}_{01}$) and is scattered in the observed direction $\boldsymbol{s}_{02}$:

$$dB_s = k_s J_s dr \qquad (2.2.2.2)$$

where J_s is the source function that includes all the contributions coming from each possible direction. Thus, we have to integrate in the solid angle the brightness coming from the generic direction $\boldsymbol{r}_i = r_i \cdot \boldsymbol{s}_{0i}$, weighted with the coefficient $k_d(\boldsymbol{r},\boldsymbol{r}_i)$ that quantify the portion of energy scattered from $\boldsymbol{r}_i$ to $\boldsymbol{r}$:

$$J_s = \frac{1}{k_s} \int_{4\pi} B(r_i)\, k_d(r, r_i) d\Omega \qquad (2.2.2.3)$$

where $1/k_s$ is a normalizing factor;

- positive increment due to *thermal emission* in the direction $\boldsymbol{r}$, dB_e : the energy absorbed by the volume causes an increase in temperature; to maintain the thermic equilibrium with the surrounding medium, the volume must emit the same quantity of energy that has absorbed:

-

$$dB_r = k_a J_a dr \qquad (2.2.2.4)$$

where J_a is the source function for the thermal emission and coincides with the black body brightness B_{CN} given by the Planck low: $J_a = B_{CN}$.

The differential form of the RTE is:

$$dB = -dB_e + dB_s + dB_r = -k_e B(r) dr + k_s J_s dr + k_a J_a dr \qquad (2.2.2.5)$$

If we define the albedo ($w = k_s/k_e$) and the total source function $J = wJ_s+(1-w)J_a$ we have:

$$\frac{dB}{dr} = -k_e B + k_e J \qquad (2.2.2.6)$$

The solution of the equation is:

$$B(r) = B(0)e^{-\tau(0,r)} + \int_0^r k_e(r')J(r')e^{-\tau(r',r)} dr' \qquad (2.2.2.7)$$

where, with respect to the Figure 2.2.2.2, we have:

- $\tau(r_1, r_2) = \int_{r_1}^{r_2} k_e(r) dr$: optical thickness between r_1 and r_2
- $t(r_1, r_2) = e^{-\tau(r_1, r_2)}$: transmittance
- $B(0)e^{-\tau(0,r)}$: brightness, in the source point, attenuated by the extinction produced by the crossed medium

- $\int_0^r k_e(r')J(r')e^{-\tau(r',r)}dr'$: sum of the infinite contributions of the medium (that is a source of thermal emission and recovery of scattering) produced by the generic infinitesimal segments *dr'*, each of them attenuated by the relative extinction of the path from the source point ***r'*** to the observing point ***r***.

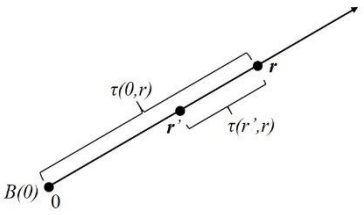

Figure 2.2.2.2: Brightness extinction with respect to eq. (2.2.2.7).

At the microwave frequencies, we can replace the brightness with the brightness temperature:

$$B = (2k/\lambda^2)eT\cdot\Delta f = (2k/\lambda^2)T_B\cdot\Delta f \qquad (2.2.2.8)$$

where k is the propagation constant and e is the emissivity of the medium.
Thus, we have that the apparent brightness temperature at the point r is:

$$T_{AP}(r) = T_B(0)e^{-\tau(0,r)} + \\ + \int_0^r k_e(r')\left[(1-w)T(r') + wT_{SC}(r')\right]e^{-\tau(r',r)}dr' \qquad (2.2.2.9)$$

where, at the microwave frequencies, we have considered the following source functions:

$$J_a = (2k/\lambda^2)T\cdot\Delta f \qquad (2.2.2.10)$$

$$J_s = (2k/\lambda^2)T_{SC}\cdot\Delta f \qquad (2.2.2.11)$$

$$T_{SC} = \frac{1}{k_s}\int_{4\pi} T_{AP}(r_i)\,k_d(r,r_i)d\Omega \qquad (2.2.2.12)$$

In the case of a non-scattering atmosphere, it is $w = 0$ and $k_e = k_a$. In the microwave bandwidth, this is the case of clear air and we have:

$$T_{AP}(r) = T_B(0)\, e^{-\tau(0,r)} + \int_0^r k_a(r')\, T(r')\, e^{-\tau(r',r)} dr' = \\ = T_{Bs} e^{-\tau(0,r)} + T_{atm}(r) \tag{2.2.2.13}$$

where T_{Bs} is the brightness temperature emitted by the surface and T_{atm} is the contribution of the atmosphere to T_{AP}.

After these considerations, we can define the apparent brightness temperature in the two cases: upwelling and downwelling radiation.

Assuming the following parameters (with respect to the Figure 2.2.2.3):

$\mu = cos\theta$
θ = zenith angle [deg]
T_s = surface temperature [K]
e_s = surface emission [adim]

For the upwelling radiation, under the hypothesis of non-scattering atmosphere, we have three contributions to T_{AP}:

- The upwelling brightness emitted by the atmosphere T_{UP}:

$$T_{UP} = \frac{1}{\mu} \int_0^A k_a(z') T(z') e^{-\tau(z',A)/\mu} dz' \tag{2.2.2.14}$$

- The downwelling brightness emitted by the atmosphere T_{DN}, scattered by the surface and then attenuated by the atmosphere itself;

$$T_{DN} = \frac{1}{\mu} \int_0^A k_a(z') T(z') e^{-\tau(0,z')/\mu} dz' \tag{2.2.2.15}$$

- The brightness emitted by the surface T_{Bs} and attenuated by the atmosphere

$$T_{Bs} = e_s T_s \tag{2.2.2.16}$$

Thus, we can write:

$$T_{AP} = e_s T_S e^{-\tau(0,A)/\mu} + T_{DN}(1 - e_s) e^{-\tau(0,A)/\mu} + T_{UP} \tag{2.2.2.17}$$

where *(1-e_s)* is the surface reflectivity. Note that both e_s and k_a depend on the frequency.

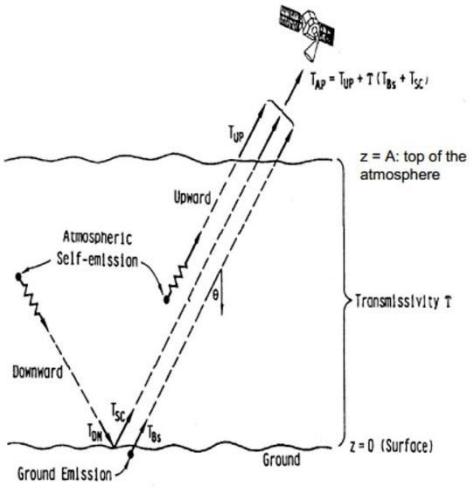

Figure 2.2.2.3: Upwelling radiation. Stratified atmosphere: T and ka depend on the height z. μ = cos θ, Ts = surface temperature, es = surface emissivity. Both es and ka depend on the frequency. z = A: top of the atmosphere.

Finally, for the downwelling radiation, we have:

$$T_{AP} = T_{DN} + T_{extra}t \tag{2.2.2.18}$$

where $t = e^{-\tau(0,\infty)}$ is the atmospheric transmittance and T_{extra} is the extraterrestrial radiation (cosmic background and galactic emission):

$$T_{extra} = T_{cos} + T_{gal} \tag{2.2.2.19}$$

where: T_{cos} = 2.7 K is the cosmic background radiation (that does not depend on frequency and zenith angle) and T_{gal} is the interstellar radiation that depends on the zenith angle and on the frequency and is negligible for frequencies higher than 5 GHz).

2.3 Microwave radiometer

A radiometer is a receiver that measures the electromagnetic radiation emitted by an object in a given frequency band.

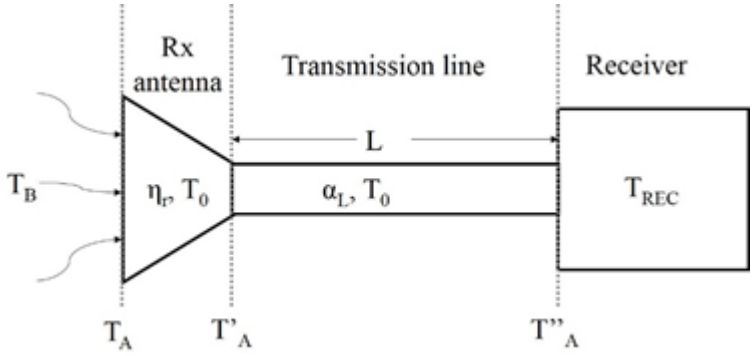

Figure 2.3.1 Receiving system: Receiving antenna + transmission line +receiver. The brightness temperature incident on the receiving antenna and the noise temperatures at the different sections of the system (T_A, T'_A, T''_A) are shown.

As concerning T_{sys} : it is the equivalent noise temperature at the receiver input. If we characterize the receiving system as in Figure 2.3.1, we can identify three sections (dotted lines in the figure). At each section, there is an equivalent noise temperature: T_A, T'_A, T''_A (for a transmitting system the scheme is specular) [22]. The first section is the input of the receiving antenna. The antenna noise temperature T_A is given by the receiving antenna collected ground noise (T_{gr}) and by the brightness temperature (also known as atmospheric equivalent noise temperature or sky-noise temperature) incident on the antenna from different directions, $T_B(\theta,\varphi)$, weighted with the directivity of the antenna $D(\theta,\varphi)$:

$$T_A = T_{gr} + \frac{1}{4\pi}\int_0^{2\pi}\int_0^{\pi} T_B(\theta,\varphi)D(\theta,\varphi)sin\theta d\theta d\varphi \qquad [K] \qquad (2.3.1)$$

where (θ,φ) are the spherical coordinates that indicate the direction of the incident wave (Figure 2.3.2).

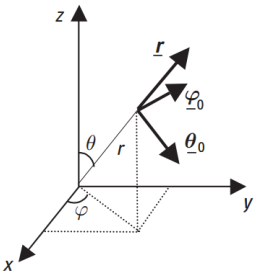

Figure 2.3.2 Spherical coordinates: usually the center of the reference system coincides with the center of the antenna aperture with the xy-plane lying on the aperture plane.

The antenna, which has a radiation efficiency η_r and a temperature T_0, generates some losses. Thus, the noise temperature at the output of the antenna T'_A is:

$$T'_A = \eta_r T_A + T_0(1 - \eta_r) \qquad [K] \tag{2.3.2}$$

The antenna and the receiver are connected through a transmission line of temperature T_0, length L, and power specific attenuation α_L [1/m]. Thus, the noise power that goes through the line is attenuated and the line itself generates noise. The antenna temperature at the receiver input T_A'' is:

$$T''_A = T'_A e^{-2\alpha_L L} + T_0(1 - e^{-2\alpha_L L}) \qquad [K] \tag{2.3.3}$$

where the loss factor $e^{-2\alpha_L L}$ can be also expressed as: $e^{-2\alpha_L L} = 10^{-\frac{L_f^{dB}}{10}} = L_{ant}$ where L_f^{dB} represents the antenna feed losses expressed in dB.

If there is an equivalent noise temperature T_{REC} at the input of the receiver, due to the thermal noise of its components, the overall equivalent noise temperature at the input of the receiving system is:

$$T_{sys} = T''_A + T_{REC} \qquad [K] \tag{2.3.4}$$

In ideal conditions: $\eta_r = 1$, $\alpha_L = 0$ and $T_A'' = T_A' = T_A$.

If we assume that the incident brightness temperature is uniform and does not depend on the incident direction, $T_B(\theta,\varphi) = T_B$ and the (2.3.1) becomes:

$$T_A = T_{gr} + \frac{T_B}{4\pi} \int_{4\pi} D(\theta,\varphi) d\Omega = T_{gr} + T_B \qquad [K] \tag{2.3.5}$$

where $\Omega = sen\theta d\theta d\varphi$ is the solid-angle element and $\int_{4\pi} D(\theta,\varphi)d\Omega = 4\pi$.

Thus, the (2.3.4) can be written as:

$$T_{sys} = \eta_r(T_{gr} + T_B)L_{ant} + T_0(1-\eta_r)L_{ant} + T_0(1-L_{ant}) + T_{RE} \quad [K] \tag{2.3.6}$$

Which, assuming $\eta_r = 1$, converts into:

$$T_{sys} = (T_{gr} + T_B)L_{ant} + T_0(1-L_{ant}) + T_{REC} \tag{2.3.7}$$

In the previous equations (2.3.6) and (2.3.7), all the parameters belong to the receiving antenna specifics except for the brightness temperature T_B. Thus, the problem of computing T_{sys} reduces to the T_B computation.

The brightness temperature emitted by a vertically-stratified atmosphere within the antenna pattern at elevation angle γ and frequency f is expressed by:

$$T_B(f,\gamma) = T_c 10^{-(L_{atm}^{dB}(f,\gamma)/10)} + T_m(f,\gamma)(1-10^{-(L_{atm}^{dB}(f,\gamma)/10)}) \quad [K] \tag{2.3.8}$$

where T_c is the cosmic background temperature (2.73 K), T_m is the mean radiative temperature (or mean effective temperature) in Kelvin, and L_{atm}^{dB} is the atmospheric path attenuation, expressed in dB. Note that, in general, it holds the following equality:

$$10^{-(L_{atm}^{dB}/10)} = e^{\frac{-L_{atm}^{dB}}{4{,}343}} = e^{-\tau} \tag{2.3.9}$$

2.3.1 The Total Power Radiometer

The Total Power Radiometer (TPR) is the simplest type of radiometer; Its block diagram is shown in Figure 2.3.1.1, on the left the functional blocks are shown, while the measured voltage and the signal spectrum are plotted in the center and on the right, respectively.

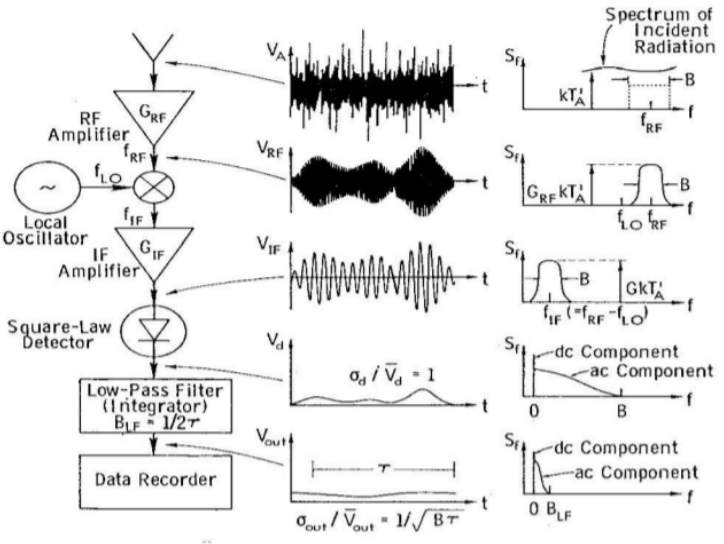

Figure 2.3.1.1: A Total Power radiometer block diagram. from (Ulaby et al. 1982)

$$V_{out} = k\,\Delta f\,G\,(T_A + T_N) \tag{2.3.1.1}$$

is dependent on the radiometer gain G and noise temperature T_N. Gain variations are inherent to the performance of both gain and lossy microwave components, so TPR are not stable enough unless frequent calibrations are performed. The sensitivity of these radiometers is given by:

$$\Delta T = \frac{T_A + T_N}{\sqrt{\Delta f\,\tau_R}} \tag{2.3.1.2}$$

being τ_r the integration time. It is the maximum than can be achieved if gain variations are neglected

2.3.2 Dicke radiometer

The Dicke radiometer was proposed to solve the stability problems of total power radiometers. A Dicke radiometer views the scene during half the cycle and a matched load during the other half of the cycle. In this case, instead of the antenna temperature the difference between the antenna temperature and a known reference value T_R is measured:

$$V_{out} = c\, G\, (T_A - T_R) \tag{2.3.2.1}$$

Note that this radiometer is more stable than TPR since the output does not depend on T_N and the weight of G can be diminished by choosing T_R values in the range of T_N. However, neglecting the gain fluctuations, the sensitivity of this configuration is:

$$\Delta T = 2\frac{T_A + T_R}{\sqrt{\Delta f\, \tau_R}} \tag{2.3.2.2}$$

It is degraded by a factor of 2 as compared to total power radiometers. The 2 factor arises from the fact that the scene is measured only half of the time.

2.3.3 Noise Injection radiometer

Noise injection radiometers (NIR) are a modification of Dicke radiometers to obtain an output independent of G and T_N. As shown in Figure 2.3.3.1, the configuration uses as input to the Dicke radiometer the signal $T_{0A} = T_A + T_I = (T_R - T_I) + T_I = T_R$, where T_I is a variable noise temperature. Since T_{0A} has the same value as T_R, then the radiometer output is zero:

$$V_{out} = c\, G\, (T'_A - T_R = 0) \tag{2.3.3.1}$$

The sensitivity of noise injection radiometers is given by:

$$\Delta T = 2\frac{T_N + T_R}{\sqrt{\Delta f\, \tau_R}} \tag{2.3.3.2}$$

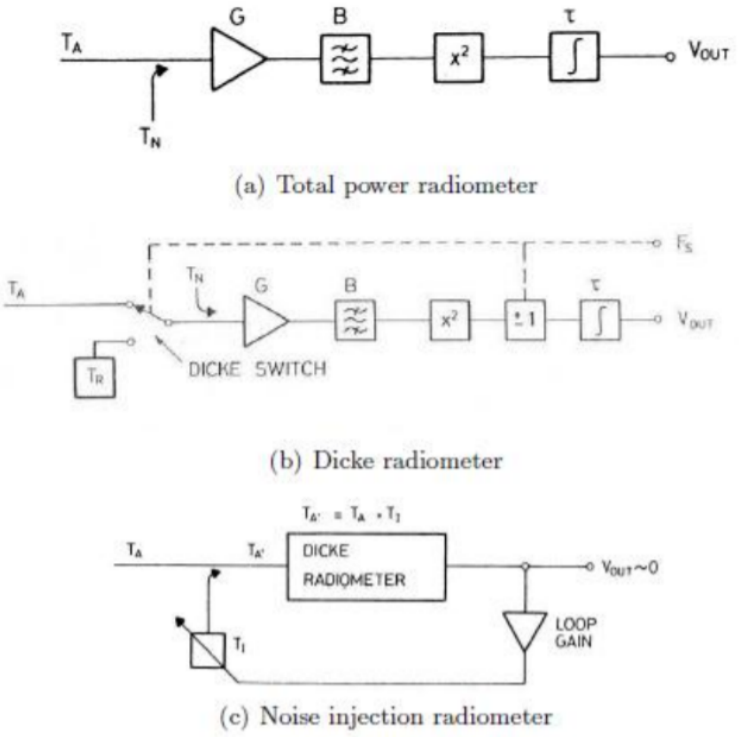

Figure 2.3.3.1: (a) total power, (b) Dicke, and (c) noise injection radiometer schematic [23]

2.4 Geolocation assessment

Geolocation of satellite data is a standard part of the post-launch calibration process. For the data to be of value, it is critical that the measured parameters be correctly mapped to the surface of the Earth. To validate the geolocation error for satellite-based microwave radiometers at 10-50 GHz (outside the absorption bands) it is possible to observe the surface, exploiting the strong difference in terms of surface emissivity between land and ocean. Fig. 2.4.1 shows an example of satellite data over Libya coastline at 19 GHz. At this frequency the land surface emissivity is in the order of 0.8 (mainly depending on geographical coordinate) and sea surface is about 0.4 (mainly depending on salinity, surface temperature, wind speed and angle of view). The brightness temperature contrast along the coastline is used to extract the shoreline contours from satellite images. The black line in Fig. 2.4.1 represents the shoreline database from GSHHG database [24]. Correlating the black line with the extracted radiometric contour it is possible to estimate the mutual shift along, obtaining

the final geolocation error in km.

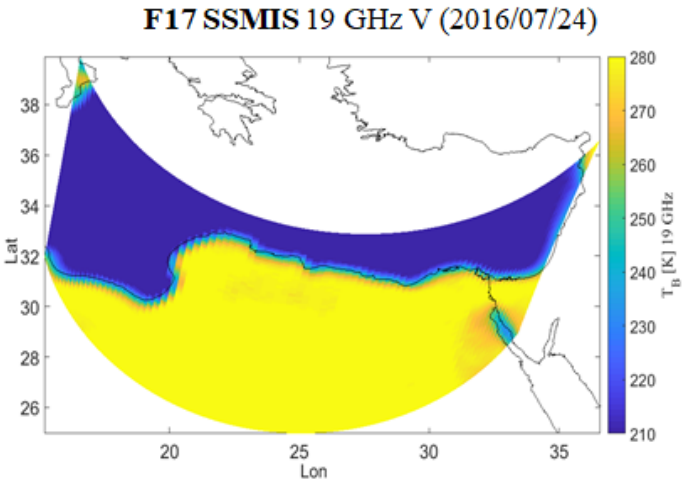

Figure 2.4.1: Example of SSMIS F17 data over Libya coastline at 19 GHz in vertical polarization (2016/07/24)

Considering several images (N) for a long time period, the geolocation error for provided by each image (ε_i) can be put together calculating the average value (ε_m)

$$\varepsilon_m = \frac{1}{N}\sum_{i=1}^{N}\varepsilon_i \tag{2.4.1}$$

and the relative standard deviation (δ_ε):

$$\delta_\varepsilon = \sqrt{\frac{\sum_{i=1}^{N}(\varepsilon_i-\varepsilon_m)^2}{N}} \tag{2.4.2}$$

The values in Eq. 2.4.1 and 2.4.2 represent the output of the geolocation validation assessment and could be used to correct the error or to correct the attitude of the satellite. In [9], Purdy et al. compared the shoreline obtained from WindSat satellite imagery with the World Vector Shoreline Data Bank II (WVS II). In this work the position of the coastline is obtained taking the peak of the first derivative of radiometric data along scan and cross scan direction, after a cubic spline interpolation to obtain a more smoothed curve. An alternative way to obtain the coastline is to exploit the difference between ascending and descending swaths. Berg et al. [13] used this method to obtain the attitude error for SSM/I spacecraft.

Unfortunately, at frequencies beyond 150 GHz, the gaseous absorption increases and the atmospheric transmittance tends to be nearly zero and the surface becomes invisible. In the chapter 3 will be described a methodology to overcome this problem and to validate the geolocation at 183 GHz.

CHAPTER 3

3. SATELLITE RADIOMETER GEOLOCATION ASSESSMENT

The Chapter contains the description of proposed methodology for the validation of the geolocation error validation for spaceborn radiometers.

3.1 Target-contour matching block diagram and data flow

The proposed target-contour matching (TCM) algorithm is shown in the following block diagram. The proposed scheme generalizes the conventional geolocation assessment method because it has some differences according to the selected target and used reference.

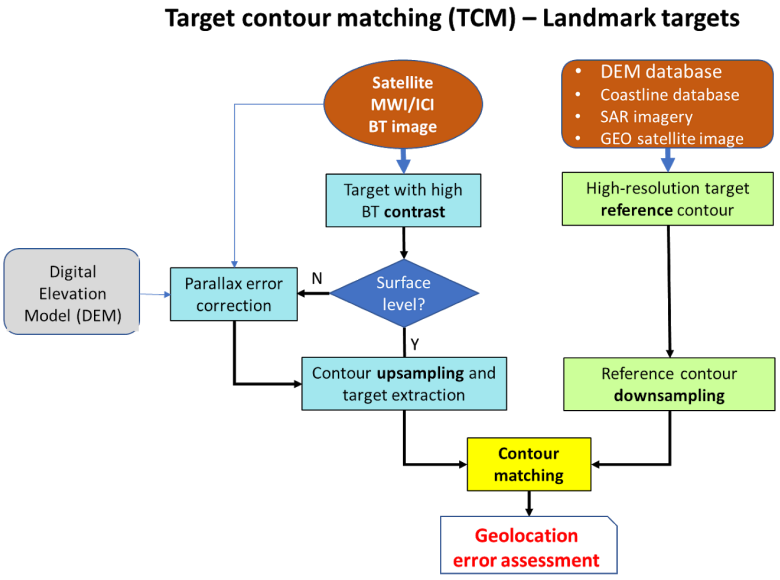

Figure 3.1.1: Logical scheme of proposed methodology to validate the geolocation using landmark targets (target-contour matching algorithm).

The inputs to the TCM methodology are the satellite radiometric imagery containing the landmark target, highlighted by the blue ellipse. To select target images with a sufficient BT contrast to extract a contour, we use a fuzzy-logic approach, as described in subsection 3.3.

Following the left branch in Fig. 3.1.1, there is a control whether the target is at sea level or not, because the satellite data are projected on terrestrial ellipsoid, as shown by point A in Fig. 3.1.2. If the target is located above sea-level, the line of sight intercepts the Earth at point C so that the corrected coordinates are those of point B. This step represents the parallax error correction and the Digital Elevation Model (DEM) is used to find the intersection between the satellite line of sight and the orography.

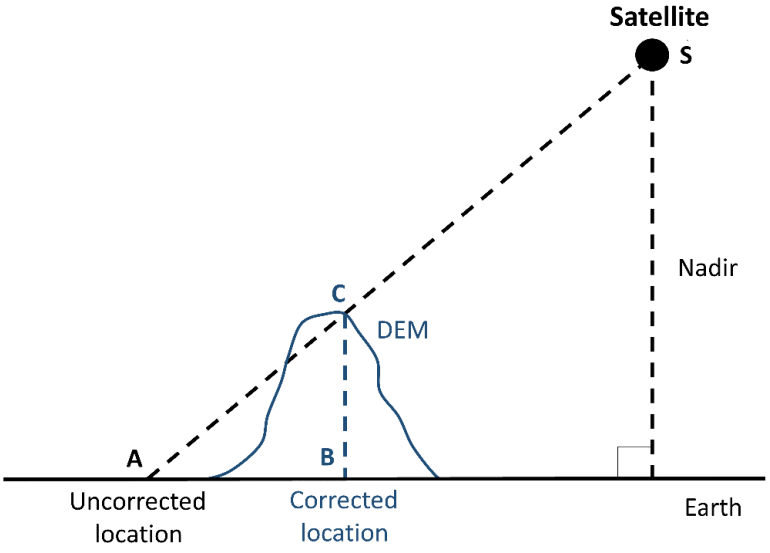

Figure 3.1.2: Digital Elevation Model correction problem

Satellite microwave radiometric images have a low spatial resolution, e.g. SSMIS F17 has about 13 km of spatial resolution. In order to fictitiously increase the resolution of a BT scenario, data are generally interpolated using a cubic interpolation, obtaining a finer spatial resolution than the nominal one. The sensitivity to the parameters of this arbitrary step is discussed in subsection 3.5.

The next step of the target-contour matching algorithm is the extraction of a contour that can be carried out by applying (e.g. see Appendix A for details):

- Canny approach [25] to obtain a line;

- Sobel filter [26] to obtain an image gradient map.

The extracted contour can be cross-correlated with a reference to estimate the geolocation accuracy using the normalized cross-correlation function $\gamma(u,v)$. Picking the maximum of (u,v) it is possible to obtain the lat-lon pixel displacements, that can be converted into shifts along x and y direction. In order to have an accuracy of about 0.1 pixel, the maximum is fitted with a polynomial of 4th order. From these pixel displacements it is possible to obtain the related latitude and longitude error and the corresponding distance error in km. An alternative way to obtain directly a displacement with sub-pixel accuracy is to use the Fast Normalized Cross-correlation (FNC) technique [27].

As mentioned, the reference contour can be different depending on the type of landmark target. The following Tab. 3.1.1 summarizes the different possible sources of contour references.

Table 3.1.1: Summary of proposed reference

Reference source	**Original source**	**Spatial resolution**	**Pre-processing needed**
SAR	Level-1 GRD	10-40 m	yes
GSHHG	GSHHG with full resolution	40 m	no
DEM	GTOPO 30	30 arc seconds (~1 km)	no

As shown in Tab. 3.1.1 we can have 3 different types of reference source, showing their original spatial resolution. In particular, for SAR images some preliminary pre-processing is necessary before using them as reference, as it is explained in Appendix C.

3.2 Criteria for landmark target selection

Considering homogeneous isothermal (constant temperature and interaction parameters) atmospheric layer of thickness H with a small albedo (thus neglecting the multiple scattering contribution), it is possible to derive the analytical solution of the radiative transfer equation for the upwelling BT as follows:

$$T_B = e_s\, T_s\, e^{-(k_e L)} + (1 - w) T_0 [1 - e^{-(k_e L)}] \quad (3.2.1)$$

where the symbols are
e_s : *surface emissivity* (adim.)
T_s : *surface temperature* (K)
$T_0 = T(z)$: *constant atmospheric temperature* (K)
k_e : *atmospheric extinction coefficient* (km^{-1})
w : *atmospheric albedo* (adim.)
L : *atmospheric slant path* ($H = L\cos\theta$ *with* θ *the nadir angle*) (km)
$e^{-(k_e L)} = t(L)$: *atmospheric transmittance* (adim.)

Considering two different close pixels p_1 and p_2 and assuming a similar atmospheric layer with the same transmittance $t(L)$, the BT contrast:

$$\Delta T_B = T_B(p_1) - T_{B2}(p_2) = T_{B1} - T_{B2} \quad (3.2.2)$$

can be written as follows:

$$\begin{aligned} \Delta T_B = {} & e_{s_1}\, T_{s_1} e^{-(k_e L)} + (1 - w) T_0 [1 - e^{-(k_e L)}] + \\ & - e_{s_2}\, T_{s_2} e^{-(k_e L)} - (1 - w) T_0 [1 - e^{-(k_e L)}] \end{aligned} \quad (3.2.3)$$

thus

$$\Delta T_B = t(L)\, [e_{s_1}\, T_{s_1} - e_{s_2}\, T_{s_2}] \quad (3.2.4)$$

Therefore, in order to have a sufficiently high BT contrast, from eq. (3.2.4) we can essentially consider areas with different surface emissivity and/or surface temperature, such as sea/lake/ice coastlines or mountain chains. In the latter case we have a surface temperature variability due to the height difference between plain and mountain as well as a different atmospheric optical thickness (i.e., transmittance of the mountain pixel larger than the plain one) entailed by the different heights of the pixels themselves. A further feature to play with is the natural variability of surface emissivity.

Taking into account these concepts, for landmark target search we have basically considered the following two major types:

a) surface water bodies (liquid or ice) sufficiently large (wrt satellite FOV);

b) mountain areas with strong slopes (altitude gradients) in relatively dry regions.

3.3 Fuzzy-logic approach to target cloud-masking

The cloud-masking analysis was performed to improve the selection of useful satellite overpasses over the selected test sites, that is in this case those SSMIS overpasses where cloud coverage may cause a larger atmospheric opacity at 183 GHz. Along a period of one year there are several satellite passes, depending on the latitude and swath width, but these can be included in the geolocation error assessment analysis in the case of:

- clear sky or limited cloudy conditions in the selected areas;
- very dry conditions with little amount of water vapour;
- enough BT contrast of the target to extract a contour.

The approach under investigation for developing, as much as possible, an automated procedure for the selection of instrument overpasses of the target area consist in using a relatively simple fuzzy-logic approach to select only useful passes, as shown in in Fig. 3.3.1.

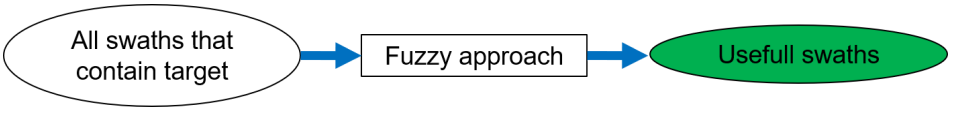

Figure 3.3.1: Fuzzy-logic approach to cloud masking

In the proposed fuzzy-logic approach, the idea is to use the estimated geolocation error and brightness temperature contrast of a specific target to understand if an overpass can be correctly used. For this purpose we use the membership functions M_1 and M_2, shown in Fig. 3.3.2. If the geolocation error is greater than a selected threshold or the BT contrast is lower than a specific threshold, the membership functions are linearly weighted. Thresholds are, to some extent, arbitrarily or empirically defined mainly depending on the channel spatial resolution at ground.

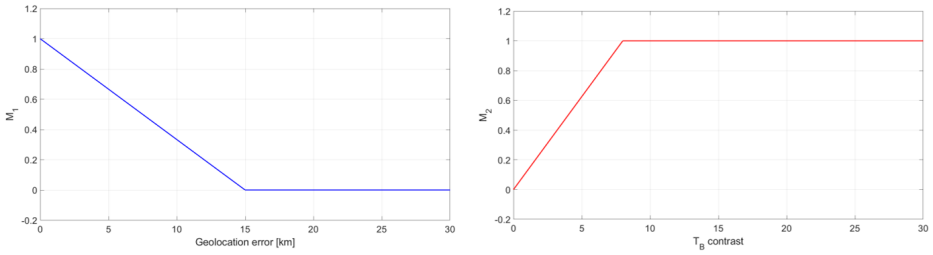

$$M_1 = \begin{cases} linear & Error \leq Error_{threshold} \\ 0 & Error > Error_{threshold} \end{cases} \qquad M_2 = \begin{cases} linear & \Delta T_B \leq \Delta T_{B\ threshold} \\ 1 & \Delta T_B > \Delta T_{B\ threshold} \end{cases}$$

Figure 3.3.2: Proposed function for fuzzy approach

After the definition of the membership functions M_1 and M_2, the inference function $I(x)$ is constructed by a multiplicative rule of the 2 membership functions:

$$I(x_1, x_2) = M_1(x_1) M_2(x_2) \tag{3.3.1}$$

where x_1 and x_2 are arbitrary variables. Finally, an image can be used to evaluate the geolocation error if it satisfies the following defuzzification step:

$$I(x_1, x_2) \geq I_{threshold} \tag{3.3.2}$$

where $I_{threshold}$ is typically set to 0.3 for all targets (see Appendix A, B and C). After a sensitivity analysis over the whole available dataset, the proposed inference function is:

$$I\left(\Delta T_{Bm}, \varepsilon\right) = M_1(\varepsilon)\, M_2(\Delta T_{Bm}) \tag{3.3.3}$$

where:

- $I(x)$ = inference function
- ΔT_{Bm} = mean BT contrast around target
- ε = geolocation error
- $M_1(\varepsilon)$ = membership function depending on the geolocation error
- $M_2\left(\Delta T_{Bm}\right)$ = membership function depending on the BT contrast

The membership functions M and their parameters are provided in the Appendix A for high-altitude lake targets, in Appendix B mountain-chain targets and in Appendix for ice-shelf targets.

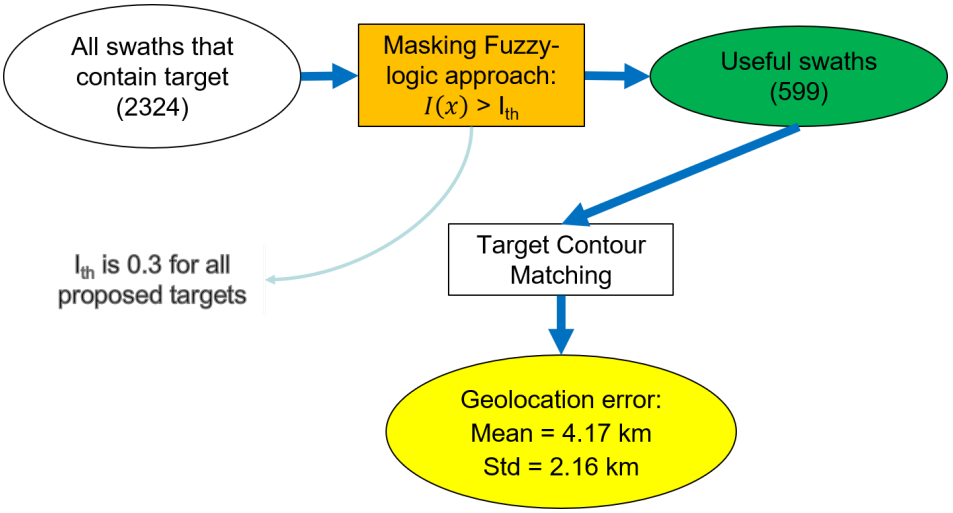

Figure 3.3.3: Logical scheme to evaluate the geolocation error starting from all swaths along time period. Numbers refer to the example of the Ross ice shelf target (see text).

As an example of the possible impact of this fuzzy-logic approach, we have considered the Ross ice shelf as a target during 2016. Fig. 3.3.3 shows the block diagram that allows evaluating the geolocation error starting from all available swaths during the selected one-year period.

This block diagram can, in principle, be extended to all satellite channels and all targets of interest, by properly setting the free parameters in the fuzzy-logic approach expressed by previous equations. Within 2016, there are 5118 SSMIS swaths, but only 2324 overpass the target. By applying the fuzzy-logic approach to select useful passes, the total number of passes has been reduced to 999. The overall mean geolocation error has been estimated to be about 4.5 km with a standard deviation of 2.1 km.

3.4 Target selection and geolocation error assessment

This section is devoted to landmark target selection and geolocation error assessment.

3.4.1 List and features of landmark targets

The following section contains the description of the results for all target and listed in the following:

Northern hemisphere

- Qinghai lake
- Karakorum mountains
- Hudson Bay
- Nares Strait

Southern hemisphere

- Ross Antarctic ice shelf
- Filchner-Ronne Antarctic ice shelf
- Amery Antarctic ice shelf
- Titicaca lake
- Andean mountains

For the geolocation assessment test we use SSMIS F17 speceborne radiometer data. Its main specifications are reported in Fig. 3.4.1.1. In particular, considering the ICI application, we have selected the 183±6.6 GHz channel in horizontal polarization, downloaded from the following web site:

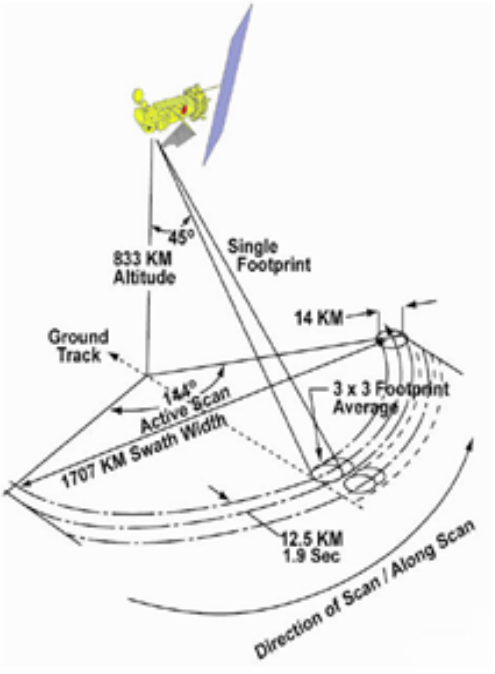

Figure 3.4.1.1a: SSMIS characteristics

Radiometric characteristics of the SSMIS (H: horizontal; V: vertical; RC: right circular).

Frequency (GHz)	Polarization (V, H, and RC)	Along-track resolution (km)	Cross-track resolution (km)	Spatial sampling (km×km)	Instrument noise (K)
19.35	H, V	73	47	45×74	0.35
22.235	V	73	47	45×74	0.45
37.0	H, V	41	31	28×45	0.22
50.3	H	17.6	27.3	37.5×37.5	0.34
52.8	H	17.6	27.3	37.5×37.5	0.32
53.596	H	17.6	27.3	37.5×37.5	0.33
54.4	H	17.6	27.3	37.5×37.5	0.33
55.5	H	17.6	27.3	37.5×37.5	0.34
57.29	RC	17.6	27.3	37.5×37.5	0.41
59.4	RC	17.6	27.3	37.5×37.5	0.40
63.283248 ± 0.285271	RC	17.6	27.3	75×75	2.7
60.792668 ± 0.357892	RC	17.6	27.3	75×75	2.7
60.792668 ± − 0.357892 ± 0.002	RC	17.6	27.3	75×75	1.9
60.792668 ± 0.357892 ± 0.005	RC	17.6	27.3	75×75	1.3
60.792668 ± 0.357892 ± 0.016	RC	17.6	27.3	75×75	0.8
60.792668 ± 0.357892 ± 0.050	RC	17.6	27.3	75×75	0.9
91.665	H, V	14	13	13×16	0.19
150	H	14	13	13×16	0.53
183.311 ± 1	H	14	13	13×16	0.38
183.311 ± 3	H	14	13	13×16	0.39
183.311 ± 6.6	H	14	13	13×16	0.56

Figure 3.4.1.1b: SSMIS channels description

For each target we provide further information about its features in the following tables. The variability of the detection per day is mainly due to the latitude of the landmark targets (near-polar targets are observed with a higher repetitivity).

Table 3.4.1.1: Summary of proposed targets, reference source and daily detectability

Landmark target	**Contour reference source**	**Detectability/day**
Northern hemisphere		
Qinghai lake	GSHHG	1
Karakorum mountains	DEM	1
Hudson Bay	GSHHG	1
Nares Strait	SAR	4-6
Southern hemisphere		
Ross Antarctic ice shelf	SAR	4-6
Filchner-Ronne Antarctic ice shelf	SAR	4-6
Amery Antarctic ice shelf	SAR	3-5
Titicaca lake	GSHHG	1
Andean mountains	DEM	1

Along 2016, we have 5118 swaths and the Tab. 3.4.1.1 reports the all available samples for each target before and after the defuzzification step. In particular, the samples after this step represent the used dataset to validate the geolocation accuracy for each target.

Table 3.4.1.2: Summary of proposed targets, reference source and daily detectability within the year 2016

Landmark target	SSMIS samples	Cloud-masked samples	Cloud-masked samples (percentage)
Northern hemisphere			
Qinghai lake	629	84	13.4 %
Karakorum mountains	707	51	7.2 %
Hudson Bay	454	62	13.6 %
Nares Strait	2140	560	26.2 %
Southern hemisphere			
Ross Antarctic ice shelf	2324	599	25.7%
Filchner-Ronne Antarctic ice shelf	2335	387	16.6%
Amery Antarctic ice shelf	1244	153	12.3%
Titicaca lake	532	41	7.7%
Andean mountains	555	125	22.5%

3.4.2 Qinghai lake in the northern hemisphere

Qinghai lake is a large lake in China with a surface of about 4500-6000 km^2 and an altitude of about 3200 m (see Fig 3.4.2.1). Its maximum length is about 105 km and the width is about 65 km so that it is larger with respect to SSMIS pixel at 183 GHz and it is possible to successfully detect it and extract its contour.

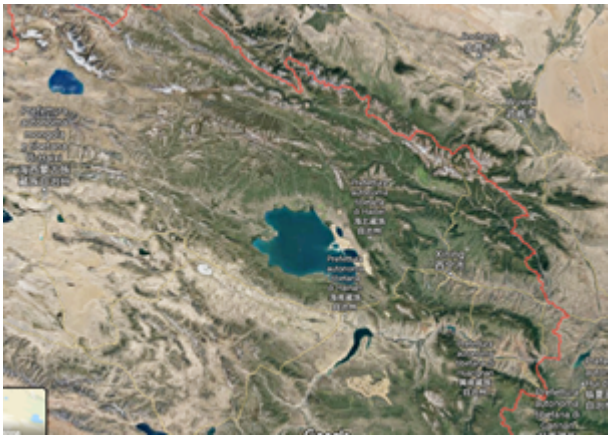

Figure 3.4.2.1: Qinghai lake from Google Maps

We have focused on the following box:

- Latitude = [36.2 ; 37.7];
- Longitude = [99.3 ; 101.0];

Tab. 3.2.1 shows the coordinates for the five points used to calculate the BT contrast following the eq. A.2.

The description of the proposed geolocation assessment methodology for this target class is provided in the Appendix A. Note that the mean BT contrast ΔT_B is derived from the following Eq. 3.4.2.1 using points in Tab. 3.4.2.1:

$$\Delta T_{Bm} = \frac{(T_B - T_A)+(T_C - T_A)+(T_D - T_A)+(T_E - T_A)}{4} \quad (3.4.2.1)$$

Table 3.4.2.1.: Coordinates of five points used to calculate the BT contrast for Qinghai lake following the eq. A.2.

Points	**Latitude** [deg]	**Longitude** [deg]
A	36.9500	100.1793
B	37.3719	100.1793
C	36.9500	100.7655
D	36.5750	100.1793
E	36.9500	99.5345

Fig. 3.4.2.2 shows two examples for Qinghai lake with SSMIS F17 at 183±6.6 GHz H.

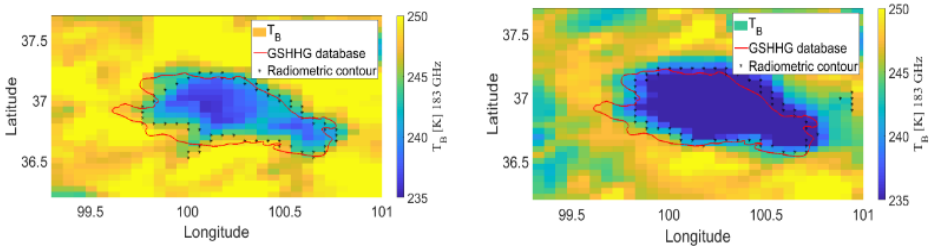

Figure 3.4.2.2: Brightness temperature image at 183±6.6 GHz H over Qinghai lake with SSMIS F17 on 2016/12/01 (left) and 2016/12/02 (right). The red line represents the GSHHG shoreline database and black markers are provided by Canny edge detection from the radiometric image.

The following Tab. 3.4.2.2 describes the number of samples in which the lake is visible from SSMIS F17 at 183 ± 6.6 GHz during 2016 applying the cloud-masking algorithm.

Table 3.4.2.2.: Number of visible days during 2016 for Qinghai lake applying the cloud-masking algorithm

Jan	Feb	Mar	Apr	May	Jun	Jul	Aug	Sep	Oct	Nov	Dec	**Total**
5	1	5	13	5	0	0	0	0	6	22	27	84

From Tab. 3.4.2.2 the total number of SSMIS available images in 2016 is 84 with geolocation assessment results summarized in Tab. 3.4.2.3.

Table 3.4.2.3: Result for Qinghai lake in 2016

Geolocation assessment parameter	**Value [km]**
Geolocation accuracy average [km]	5.86
Geolocation accuracy standard deviation [km]	2.59

3.4.3 Karakorum mountains in the northern hemisphere

It is a large mountain range spanning the borders between Pakistan, India and China with the northwest extremity of the range extending to Afghanistan and Tajikistan, as shown in Fig. 3.4.3.1.

Figure 3.4.3.1: Karakorum mountains from Google Maps

Its range is about 500 km, so we have focused on the following sub-box:

- Latitude = [35.5 ; 38.5];
- Longitude = [76.0 ; 80.0];

The BT contrast for Karakorum mountains is derived following the Eq. 3.4.3.1 with points in Tab. 3.4.3.1

$$\Delta T_{Bm} = \frac{(T_B - T_A)+(T_D - T_C)+(T_F - T_E)+(T_H - T_G)}{4} \qquad (3.4.3.1)$$

Table 3.4.3.1.: Coordinates of eight points used to calculate the BT contrast for Karakorum mountains following the eq. B.2.

Points	**Latitude** [deg]	**Longitude** [deg]
A	36.8385	76.3944
B	37.5308	76.3944

C	36.6538	77.4648
D	37.2077	77.4648
E	36.3769	78.5915
F	37.0692	78.5915
G	36.1462	79.6056
H	36.7462	79.6056

Fig. 3.4.3.2 shows an example for Karakorum mountains with SSMIS F17 at 183±6.6 GHz H.

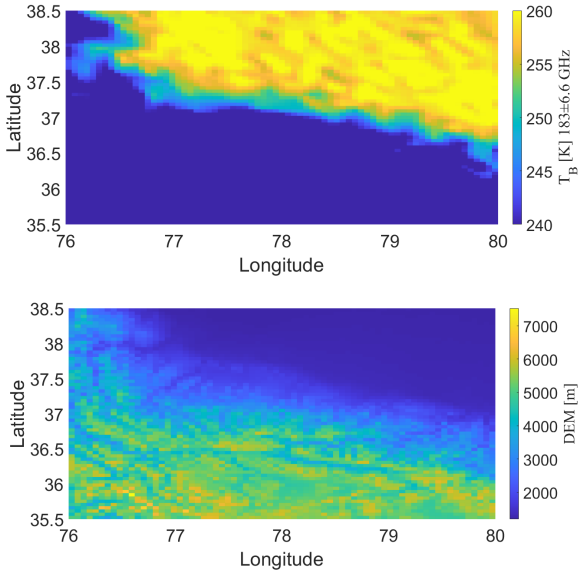

Figure 3.4.3.2: In the left there is the brightness temperature image with SSMIS F17 at 183±6.6 GHz H over Karakorum mountains on 2016/10/19 In the right there is the reference digital elevation model.

The description of the proposed geolocation assessment methodology for this target class is provided in the Appendix B.

Table 3.4.3.2: Number of visible days during 2016 for Karakorum mountains applying the cloud-masking algorithm

Jan	Feb	Mar	Apr	May	Jun	Jul	Aug	Sep	Oct	Nov	Dec	**Total**
6	7	6	4	3	0	1	1	3	7	6	7	51

From Tab. 3.4.3.2 the total number of SSMIS available images in 2016 is 51 with geolocation assessment results summarized in Tab. 3.4.3.3.

Table 3.4.3.3: Result for Karakorum mountains in 2016

Geolocation assessment parameter	**Value [km]**
Geolocation accuracy average [km]	5.62
Geolocation accuracy standard deviation [km]	2.60

3.4.4 Hudson Bay in the northern hemisphere

It is a large body of saltwater in northeastern Canada with a surface area of 1,230,000 km^2, as shown in Fig. 3.4.4.1.

Figure 3.4.4.1: Hudson Bay from Google Maps

We have focused on the following box:

- Latitude = [56.0 ; 62.0];
- Longitude = [-96.0 ; -87.0];

Tab. 3.4.4.1 shows the coordinates for the eight points used to calculate the BT contrast for Hudson Bay following the Eq. 3.4.4.1 and points in Tab. 3.4.4.1

$$\Delta T_{Bm} = \frac{(T_B - T_A)+(T_D - T_C)+(T_F - T_E)+(T_H - T_G)}{4} \quad (3.4.4.1)$$

Table 3.4.4.1.: Coordinates of eight points used to calculate the BT contrast for Hudson Bay following the eq. B.2.

Points	**Latitude** [deg]	**Longitude** [deg]
A	61,4091	-94,8545
B	61.4091	-92,8091
C	59.1364	-95,4273
D	59.1364	-93,7909
E	57.3182	-92,9727
F	57.7727	-91,9909
G	56.4091	-89,1273
H	57.0909	-88,7182

Fig. 3.4.4.2 shows two examples for Hudson Bay with SSMIS F17 at 183±6.6 GHz H.

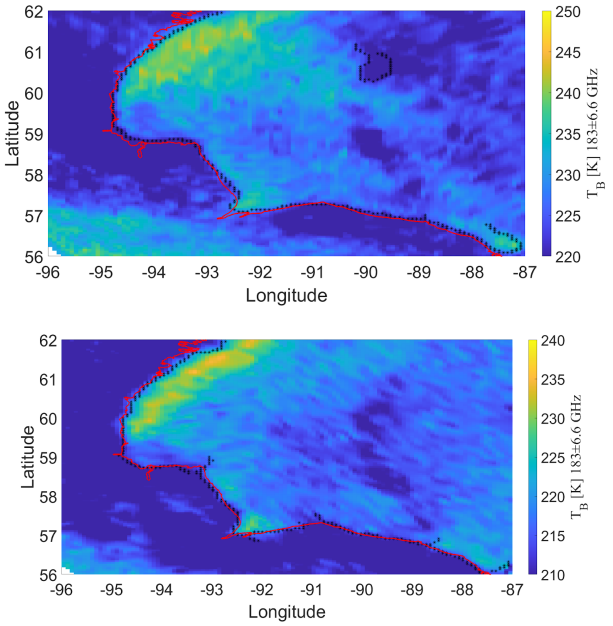

Figure 3.4.4.2: Brightness temperature image at 183±6.6 GHz H over Hudson Bay with SSMIS F17 on 2016/01/27 (left) and 2016/02/11 (right). The red line represents the GSHHG shoreline database and black markers are provided by Canny edge detection from radiometric image.

The description of the proposed geolocation assessment methodology for this target class is provided in the Appendix A.

The following Tab. 3.4.4.2 describes the number of samples in which the lake is visible from SSMIS F17 at 183 ± 6.6 GHz during 2016 applying the cloud-masking algorithm.

Table 3.4.4.2: Number of visible days during 2016 for Hudson Bay applying the cloud-masking algorithm

Jan	Feb	Mar	Apr	May	Jun	Jul	Aug	Sep	Oct	Nov	Dec	**Total**
13	17	10	3	0	0	0	0	0	0	0	19	62

From Tab. 3.4.4.2 the total number of SSMIS available images in 2016 is 62 with geolocation assessment results summarized in Tab. 3.4.4.3.

Table 3.4.4.3: Result for Hudson Bay in 2016

Geolocation assessment parameter	Value [km]
Geolocation accuracy average [km]	6.29
Geolocation accuracy standard deviation [km]	2.89

3.4.5 Nares Strait in the northern hemisphere

Fig. 3.4.5.1 shows the Nares Strait, that is a waterway between Ellesmere Island and Greenland that connects the northern part of Baffin Bay with the Lincoln Sea (see Fig. 3.4.5.1).

Figure 3.4.5.1: Nares Strait from Google Maps

Fig. 3.4.5.2 reports an example of radiometric image in the left and SAR image in the right.

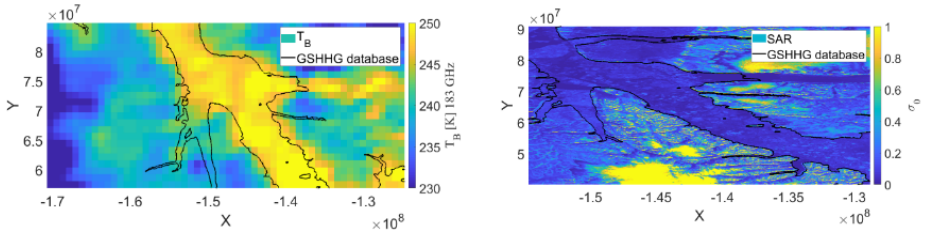

Figure 3.4.5.2: Brightness temperature image at 183±6.6 GHz H over Nares Strait from SSMIS F17 on 2016/11/02 (left), the black line is provided by GSHHG shoreline database. SENTINEL 1 IW-GRD on 2017/01/12 (right)

We have focused on the following box:

- Latitude = [80.0 ; 82.5];
- Longitude = [-66.0 ; -63.0];

The description of the proposed geolocation assessment methodology for this target class is provided in the Appendix B with two main differences:

- instead of the DEM gradient that is used as reference for mountain chain, in the case of Nares Strait we proposed to use the spatial horizontal gradient of the SAR image as reference. Therefore to calculate the geolocation accuracy we correlated the gradient of the BT with the gradient of SAR image.

- since we have a complex variable orography, in order to mitigate the "orographic noise" in the cross-correlation between BT and SAR gradient, the following inference function is adopted:

$$I(\varepsilon) = M_1(\varepsilon)\, M_2(\varepsilon) \qquad (3.4.5.1)$$

where:

- $I(\varepsilon)$ = inference function
- ε = geolocation error
- $M_1(\varepsilon)$ = term that considers the geolocation error with 5 km of spatial resolution
- $M_2(\varepsilon)$ = term that considers the geolocation error with 6 km of spatial resolution

The following Tab. 3.4.5.1 describes the number of samples in which the lake is visible from SSMIS F17 at 183 ± 6.6 GHz during 2016 applying the cloud-masking algorithm.

Table 3.4.5.1: Number of visible days during 2016 for Nares Strait applying the cloud-masking algorithm

Jan	Feb	Mar	Apr	May	Jun	Jul	Aug	Sep	Oct	Nov	Dec	**Total**
32	32	50	16	72	12	33	7	31	103	112	60	560

From Tab. 3.4.5.1 the total number of SSMIS available images in 2016 is 688 with geolocation assessment results summarized in Tab. 3.4.5.2.

Table 3.4.5.2: Result for Nares Strait in 2016

Geolocation assessment parameter	**Value [km]**
Geolocation accuracy average [km]	4.74
Geolocation accuracy standard deviation [km]	2.02

3.4.6 Antarctic ice shelves in the southern hemisphere

Antarctic ice shelves are thick suspended platforms of ice that forms where a glacier or ice sheet flows down to a coastline and onto the ocean surface. The ice covers the ground (grounded ice) and it extends into the ocean, with the lower part that detaches from the ground (grounding line), creating a suspended platform of ice (ice shelf), as shown in Fig. 3.4.6.2.

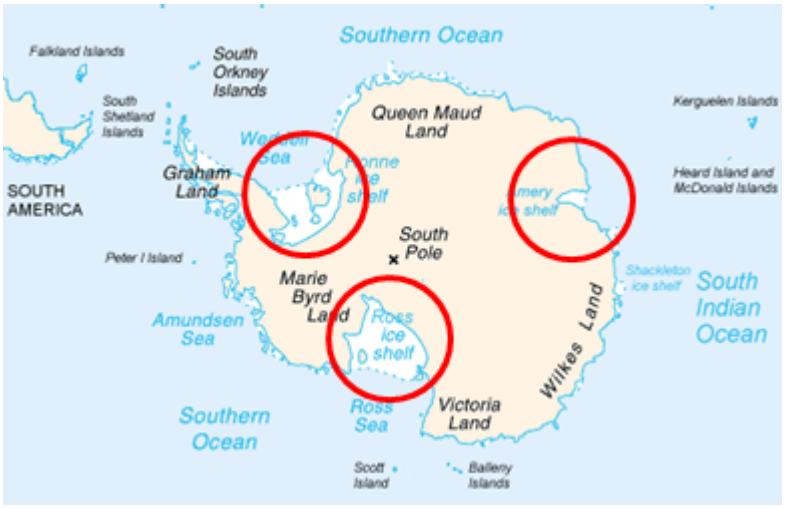

Figure 3.4.6.1: Antarctic ice shelves

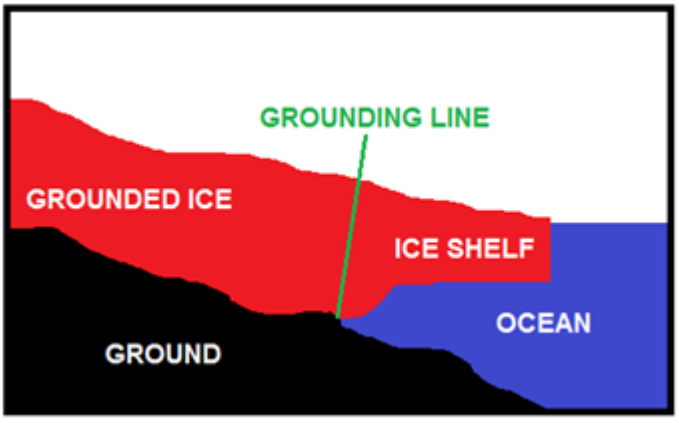

Figure 3.4.6.2: Scheme of shelves coastline

For this type of landmark target, we propose to use SAR images as reference, because they have very high spatial resolution (10-40 m). The adopted SAR data are the Level-1 Ground Range Detected (GRD) products, those consist of focused SAR data that has been detected, multi-looked and projected to ground range using an Earth ellipsoid model. The resulting product has approximately square spatial resolution pixels and square pixel spacing with reduced speckle and three possible spatial resolution: Full Resolution (FR), High Resolution (HR), Medium Resolution (MR). See Appendix C for more information on used SAR data.

3.4.6.1 Ross ice shelf

The Ross ice shelf is the largest ice shelf of Antarctica (as of 2013 an area of roughly 500,809 km^2 and about 800 km across.

For this target we use a SAR image, as shown in Fig. 3.4.6.1.2. SAR data are preprocessed, as explained in Appendix C. As explained in Appendix C, at polar areas it is preferable to use a polar stereographic projection to reduce distortion in the image. Fig. 3.4.6.1.3 shows the same SAR image contained in the Fig. 3.4.6.1.2 projected in this reference system. The red markers show the contour obtained with Canny algorithm on SAR image.

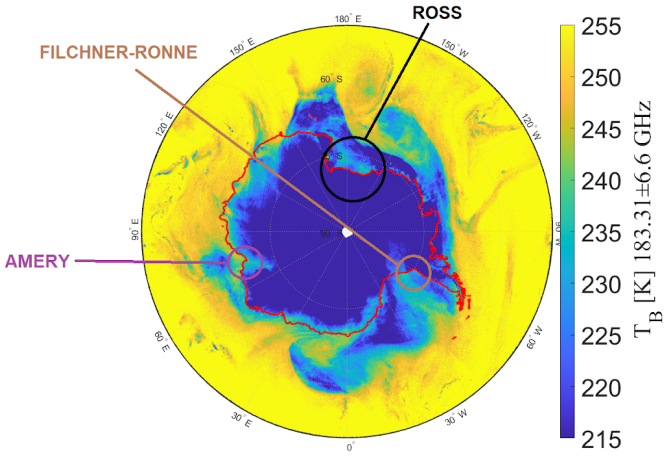

Figure 3.4.6.1.1: BT at 183±6.6 GHz H from F17 SSMIS. The black circle indicates the Ross ice shelf and the red highlights the Filchner.Ronne ice shelf.

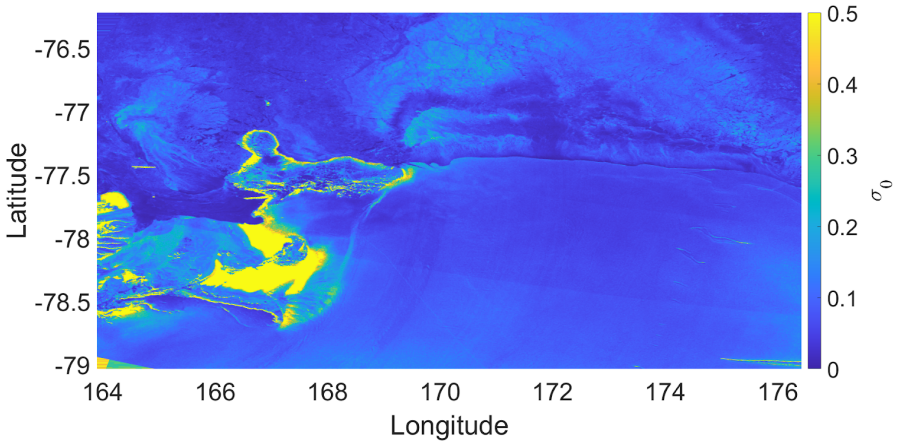

Figure 3.4.6.1.2: Example of SAR images used as reference for Ross ice shelf

The ice coastline can change its shape along season or it is possible that a big piece of coast can collapse creating an iceberg with a consequently big change in shape. As reports in [28] the ice velocity ranges from a few meters per year to several hundred meters per year in ice streams. Ice velocity increases as the ice moves seaward, reaching 1 km per year in the central portions of the ice front. We do not focus on the center of the shelf and its movement is much lower than geometrical resolution of radiometric imagery, indeed comparing SAR image in winter season and SAR image in summer, we obtain the same reference contour when we project the ice contour in the grid with 5 km of special resolution, as explained in the Appendix C. Therefore we must only monitor the formation of icebergs and to do this we compared SAR images on January 2016 with an image on 2017, observing the absence of significant variations in shape.

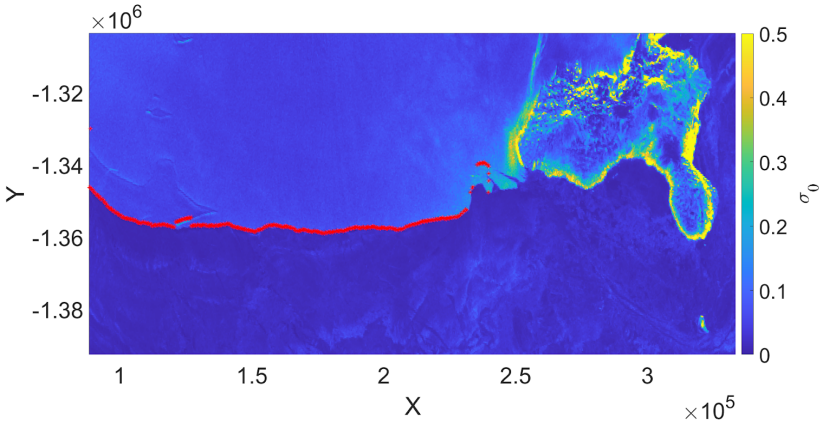

Figure 3.4.6.1.3: SAR contour extracted with Canny algorithm

We have focused on the following box:

- Latitude = [-78.5 ; -76.5];
- Longitude = [170.6 ; 178.5];

BT contrast for Ross ice shelf has been calculated with the Eq. 3.4.6.1.1 with points in Tab. 3.4.6.1.1, expressed on polar stereographic map

$$\Delta T_{Bm} = \frac{(T_B - T_A)+(T_D - T_C)+(T_F - T_E)+(T_H - T_G)}{4} \quad (3.4.6.1.1)$$

Table 3.4.6.1.1: Polar stereographic coordinates of eight points used to calculate the BT contrast for Ross ice shelf following the eq. C.2.

Points	X	Y
A	6.3796 10^4	-1.3149 10^6
B	6.3796 10^4	-1.3763 10^6
C	1.0524 10^5	-1.33 10^6
D	1.0524 10^5	-1.4070 10^6
E	1.6222 10^5	-1.3303 10^6
F	1.6222 10^5	-1.3814 10^6
G	2.1920 10^5	-1.3251 10^6
H	2.1920 10^5	-1.3712 10^6

The description of the proposed geolocation assessment methodology for this target class is provided in the Appendix C. After defuzzification step during 2016, we obtain the samples in the following Tab. 3.4.6.1.2:

Table 3.4.6.1.2: Number of visible days during 2016 for Ross ice shelf

Jan	Feb	Mar	Apr	May	Jun	Jul	Aug	Sep	Oct	Nov	Dec	**Total**
0	0	15	67	57	109	114	78	81	61	17	0	599

From Tab. 3.4.6.1.2 the total number of SSMIS available images in 2016 is 599 with geolocation assessment results summarized in Tab. 3.4.6.1.3. The mean BT contrast ΔT_B , derived from (C.3) and obtained from the 2016 dataset along the lake coastline, is about 16.4 K.

Table 3.4.6.1.3: Result for Filchner-Ronne ice shelf on 2016

Geolocation assessment parameter	**Value [km]**
Geolocation accuracy average [km]	4.17
Geolocation accuracy standard deviation [km]	2.16

3.4.6.2 Filchner-Ronne ice shelf

The whole Filchner-Ronne ice shelf covers some 430,000 km², making it the second largest ice shelf in Antarctica, after the Ross Ice Shelf, as shown in Fig. 3.4.6.1.1 by the black circle. The necessary steps to validate the geolocation accuracy for Filchner-Ronne ice shelf are the same as Ross ice shelf, as explained in Appendix C. The only difference is that the reference SAR image is different, as shown in Fig. 3.4.6.2.1.

Fig. 3.4.6.2.2 shows the same SAR image contained in the Fig. 3.4.6.2.1 projected on a polar stereographic map. The red marker shows the contour obtained with Canny algorithm on SAR image.

During 2016, there was no iceberg formation and the shape is almost the same throughout the entire year. we have focused on the following box:

- Latitude = [-75.7 ; -74.4];
- Longitude = [-64.5 ; -56.5];

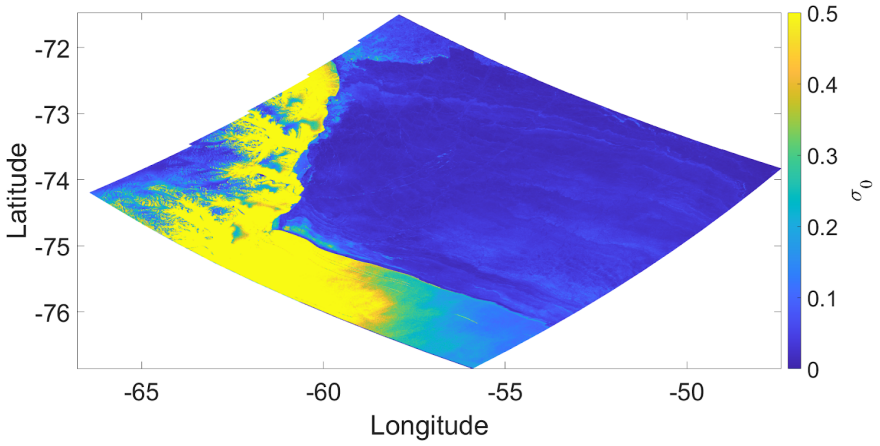

Figure 3.4.6.2.1: Example of SAR images used as reference for Filchner-Ronne ice shelf

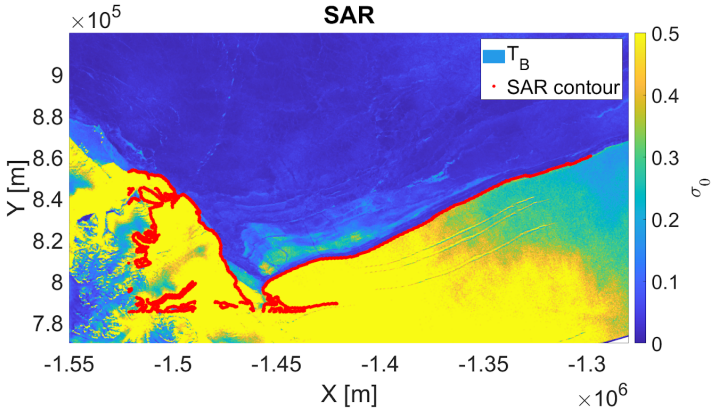

Figure 3.4.6.2.2: SAR contour extracted with Canny algorithm

BT contrast for Filchner-Ronne ice shelf has been calculated with the Eq. 3.4.6.1.1 with points in Tab. 3.4.6.2.1, expressed on a polar stereographic map.

$$\Delta T_{Bm} = \frac{(T_B - T_A)+(T_D - T_C)+(T_F - T_E)+(T_H - T_G)}{4} \qquad (3.4.6.2.1)$$

Table 3.4.6.2.1: Polar stereographic coordinates of eight points used to calculate the BT contrast for Filchner-Ronne ice shelf following the eq. C.2.

Points	X	Y
A	$-1.5011\ 10^6$	$8.3170\ 10^5$
B	$-1.5011\ 10^6$	$8.8246\ 10^5$
C	$-1.4453\ 10^6$	$7.9110\ 10^5$
D	$-1.4453\ 10^6$	$8.2663\ 10^5$
E	$-1.3794\ 10^6$	$8.0633\ 10^5$
F	$-1.3794\ 10^6$	$8.4693\ 10^5$
G	$-1.3185\ 10^6$	$8.4186\ 10^5$
H	$-1.3185\ 10^6$	$8.7739\ 10^5$

The description of the proposed geolocation assessment methodology for this target class is provided in the Appendix C. After the defuzzification step during 2016, we obtain the samples in the following Tab. 3.4.6.2.2:

Table 3.4.6.2.2: Number of visible days during 2016 for Filchner-Ronne ice shelf

Jan	Feb	Mar	Apr	May	Jun	Jul	Aug	Sep	Oct	Nov	Dec	**Total**
0	0	14	62	65	46	78	65	42	15	0	0	387

From Tab. 3.4.6.2.2 the total number of SSMIS available images in 2016 is 387 with geolocation assessment results summarized in Tab. 3.4.6.2.3.

Table 3.4.6.2.3: Result for Filchner-Ronne ice shelf on 2016

Geolocation assessment parameter	Value [km]
Geolocation accuracy average [km]	5.75
Geolocation accuracy standard deviation [km]	2.35

3.4.6.3 Amery ice shelf

The necessary steps to validate the geolocation accuracy for Filchner-Ronne ice shelf are the same as Ross ice shelf, as explained in Appendix C. The only difference is that the reference SAR image is different, as shown in Fig. 3.4.6.3.1.

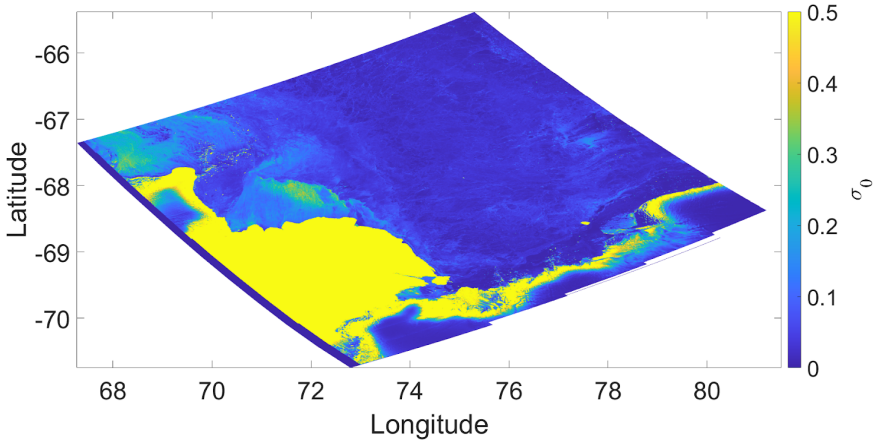

Figure 3.4.6.3.1: Example of SAR images used as reference for Amery ice shelf

Fig. 3.4.6.3.2 shows the same SAR image contained in the Fig. 3.4.6.2.1 projected on a polar stereographic map. The red marker shows the contour obtained with Canny algorithm on SAR image.

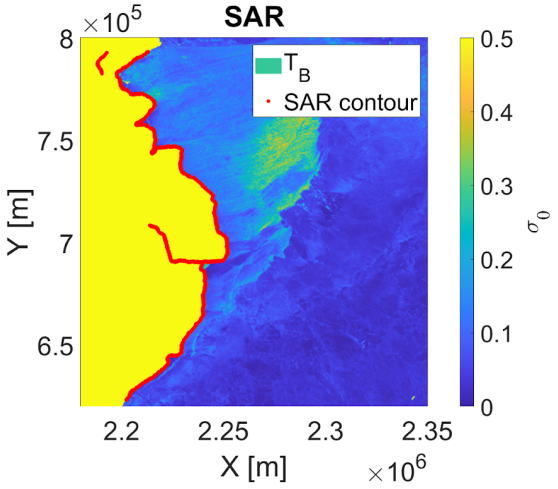

Figure 3.4.6.3.2: SAR contour extracted with Canny algorithm

During 2016, there was no iceberg formation and the shape is almost constant during the entire year. We have focused on the following box:

- Latitude = [-69.1 ; -68.0];
- Longitude = [70.8 ; 74.2];

BT contrast for Amery ice shelf has been calculated with the Eq. 3.4.6.3.1 with points in Tab. 3.4.6.3.1, expressed on a polar stereographic map.

$$\Delta T_{Bm} = \frac{(T_B - T_A)+(T_D - T_C)+(T_F - T_E)+(T_H - T_G)}{4} \qquad (3.4.6.3.1)$$

Table 3.4.6.3.1: Polar stereographic coordinates of eight points used to calculate the BT contrast for Amery ice shelf following the eq. C.2.

Points	X	Y
A	2.1984 10^6	7.6657 10^5
B	2.2356 10^6	7.6657 10^5
C	2.2303 10^6	7.1870 10^5
D	2.2675 10^6	7.1875 10^5
E	2.2515 10^6	6.7093 10^5

F	$2.2143\ 10^6$	$6.7093\ 10^5$
G	$2.1984\ 10^6$	$6.3373\ 10^5$
H	$2.2356\ 10^6$	$6.3373\ 10^5$

The description of the proposed geolocation assessment methodology for this target class is provided in the Appendix C. The number of obtained samples, after the defuzzification step during 2016, is given in Tab. 3.4.6.3.2:

Table 3.4.6.3.2: Number of visible days during 2016 for Filchner-Ronne ice shelf

Jan	Feb	Mar	Apr	May	Jun	Jul	Aug	Sep	Oct	Nov	Dec	**Total**
5	5	20	22	13	32	19	11	15	7	4	0	153

From Tab. 3.4.6.3.2 the total number of SSMIS available images in 2016 is 153 with geolocation assessment results summarized in Tab. 3.4.6.3.3.

Table 3.4.6.3.3: Result for Filchner-Ronne ice shelf on 2016

Geolocation assessment parameter	**Value [km]**
Geolocation accuracy average [km]	6.25
Geolocation accuracy standard deviation [km]	1.55

3.4.7 Titicaca lake in the southern hemisphere

Titicaca lake is a large, deep lake in the Andes on the border of Bolivia and Peru. It has a surface of about 8372 km^2 and an elevation of 3,812 m (see Fig. 3.4.7.1).

We have focused on the following box:

- Latitude = [-17.5 ; -14.5]
- Longitude = [-70.3 ; -68.0];

Figure 3.4.7.1: Titicaca lake

Note that the mean BT contrast ΔT_B is derived from the following Eq. 3.4.7.1 using points in Tab. 3.4.7.1:

$$\Delta T_{Bm} = \frac{(T_B - T_A)+(T_C - T_A)+(T_D - T_A)+(T_E - T_A)}{4} \qquad (3.4.7.1)$$

Table 3.4.7.1.: Coordinates of five points used to calculate the BT contrast for Titicaca lake following the eq. A.2.

Points	**Latitude** [deg]	**Longitude** [deg]
A	-15.8766	-69.3462
B	-15.1745	-69.3462

C	-15.8766	-68.6250
D	-16.5787	-69.3462
E	-15.8766	-70.2115

Fig. 3.4.7.2 shows two examples for Titicaca lake with SSMIS F17 at 183±6.6 GHz H.

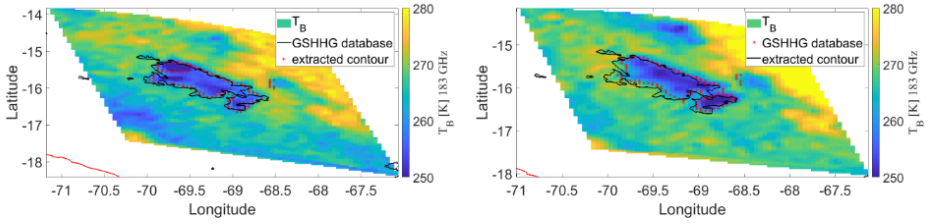

Figure 3.4.7.2: Brightness temperature image at 183±6.6 GHz H over Titicaca lake with SSMIS F17 on 2016/05/31 (left) and 2016/07/31 (right). The red markers represent the GSHHG shoreline database and black markers are provided by Canny edge detection from radiometric images.

The description of the proposed geolocation assessment methodology for this target class is provided in the Appendix A.

Table 3.4.7.2: Number of visible days during 2016 for Titicaca lake applying the cloud-masking algorithm

Jan	Feb	Mar	Apr	May	Jun	Jul	Aug	Sep	Oct	Nov	Dec	**Total**
0	0	0	2	5	8	8	9	4	2	3	0	41

From Tab. 3.4.7.2 the total number of SSMIS available images in 2016 is 41 with geolocation assessment results summarized in Tab. 3.4.7.3.

Table 3.4.7.3: Result for Titicaca lake in 2016

Geolocation assessment parameter	Value [km]
Geolocation accuracy average [km]	6.53
Geolocation accuracy standard deviation [km]	2.82

3.4.8 Andean mountains in the southern hemisphere

Andean mountains are the longest continental mountain range in the world, forming a continuous highland along the western edge of South America (see Fig. 3.4.8.1).

We have focused on the following box:

- Latitude = [-15.8 ; -18.8]
- Longitude = [-72.8 ; -69.2];

Tab. 3.4.8.1 shows the coordinates for the eight points used to calculate the BT contrast for Andean mountains following the eq. B.2.

Fig. 3.4.8.2 shows an example for Andean mountains with SSMIS F17 at 183±6.6 GHz H.

Figure 3.4.8.1: Andean mountains from Google

The BT contrast for Andean mountains is derived following the Eq. 3.4.8.1 with points in Tab. 3.4.8.1

$$\Delta T_{Bm} = \frac{(T_B - T_A)+(T_D - T_C)+(T_F - T_E)+(T_H - T_G)}{4} \quad (3.4.8.1)$$

Table 3.4.8.1.: Coordinates of eight points used to calculate the BT contrast for Andean mountains following the eq. B.2.

Points	**Latitude** [deg]	**Longitude** [deg]
A	-16.0769	-71.2432
B	-16.5385	-71.8757
C	-16.2154	-70.4162
D	-17.0000	-71.1459
E	-16.9077	-70.0270
F	-17.4615	-70.5622
G	-17.6923	-69.4432
H	-18.3846	-69.9297

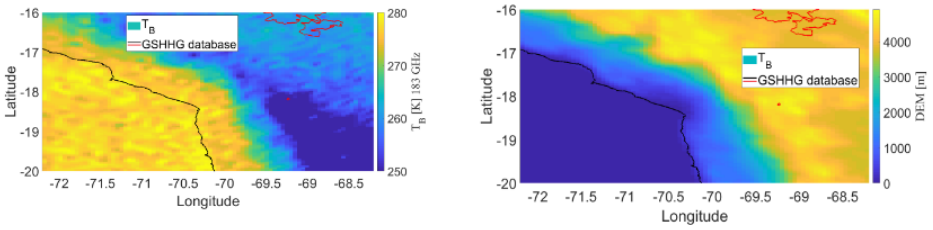

Figure 3.4.8.2: In the left there is the brightness temperature image at 183±6.6 GHz H over Andean mountains SSMIS F17 on 2016/07/14 In the right there is the reference digital elevation model. The black line represents GSHHG shoreline database

The description of the proposed geolocation assessment methodology for this target class is provided in the Appendix B.

Table 3.4.8.2: Number of visible days during 2016 for Andean mountains applying the cloud-masking algorithm

Jan	Feb	Mar	Apr	May	Jun	Jul	Aug	Sep	Oct	Nov	Dec	**Total**
0	0	0	0	4	23	20	22	21	19	14	2	125

From Tab. 3.4.8.2 the total number of SSMIS available images in 2016 is 125 with geolocation assessment results summarized in Tab. 3.4.8.3.

Table 3.4.8.3: Result for Andean mountains in 2016

Geolocation assessment parameter	**Value [km]**
Geolocation accuracy average [km]	5.32
Geolocation accuracy standard deviation [km]	3.06

CHAPTER 4

4. SENSITIVITY ANALYSIS AND FREQUENCY SCALING

The Chapter contains the sensitivity analysis of proposed methodology and an artificial neural network to frequency scaling to reconstruct 243 GHz from existing data at 150 GHz and 183 GHz

4.1 Sensitivity analysis of assessment methodology

The error budget quantification of the geolocation assessment methodology is a difficult task. A feasible approach is to follow a sensitivity analysis of the various steps of the proposed methodology and to evaluate the optimal value of each parameter as well as the related accuracy. In particular we can select the following critical parameters:

1. Interpolation-grid spatial resolution
2. Spatial interpolation method
3. Cross-correlation method

4.1.1 Sensitivity to interpolation-grid spatial resolution

The first important step is the interpolation on a grid with higher resolution. The upsampling factor can be between 2 and 3.5 and here we have focused on the evenly spaced grid at 4, 5, 6 and 7 km. Considering the dataset described in Sec 3.4.6.1. for the Ross ice shelf and validating the geolocation accuracy changing the interpolating grid, we have obtained the mean value (average) and standard deviation, reported in Fig. 4.1.1.1.

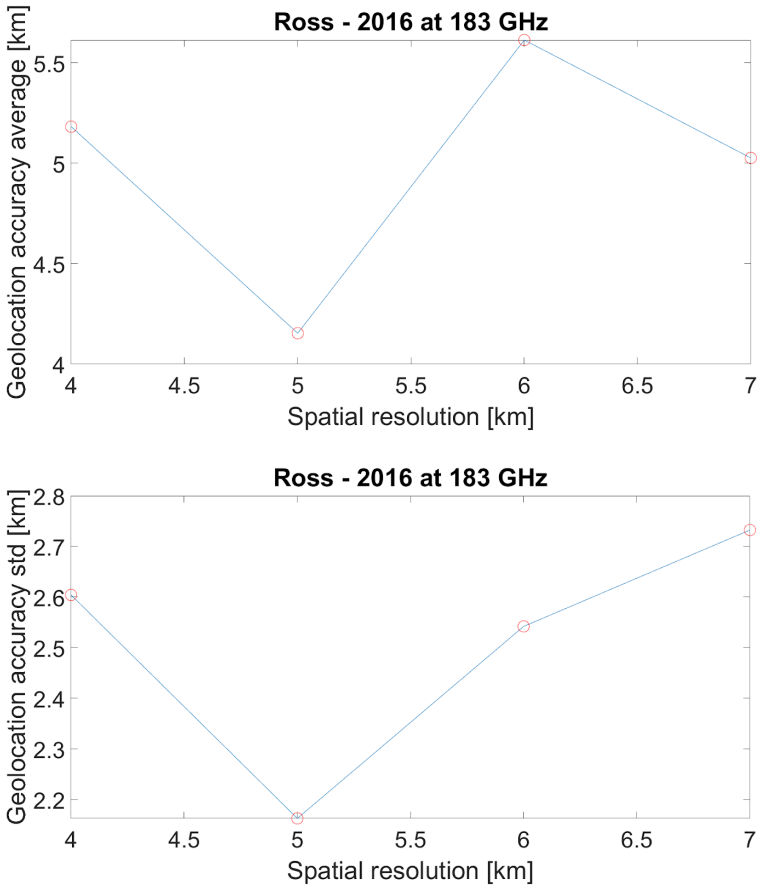

Figure 4.1.1.1: Results for Ross ice shelf in relation to resampling grid spatial resolution. In the top there is the mean value of geolocation accuracy and in the bottom the related standard deviation.

The Fig. 4.1.1.1 is also summarized in the following Tab. 4.1.1.1.

Table 4.1.1.1: Results for Ross ice shelf in relation to resampling grid spatial resolution.

Spatial resolution [km]	**4**	**5**	**6**	**7**
Geolocation accuracy average [km]	5.18	4.17	5.6	5.03
Geolocation accuracy standard deviation [km]	2.60	2.16	2.54	2.73

The minimum value of mean geolocation accuracy and, even more important, the standard deviation is obtained for 5 km of spatial resolution. For this reason

in all presented tests we have used this value in the interpolated grid. Calculating the standard deviation of the geolocation accuracy average for several spatial resolutions, it is possible to estimate the variance introduced by this step in the methodology. The obtained standard deviation is 0.62 km.

4.1.2 Sensitivity analysis to spatial interpolation method

In addition to the spatial resolution, the method of spatial interpolation is also a critical one. We have selected the following methods:

- **Linear**: Triangulation based on linear interpolation, such as using linear polynomials to construct new data points within the range of a discrete set of known data points
- **Neighbor**: Triangulation based on natural neighbor interpolation. The method is based on Voronoi tessellation of a discrete set of spatial points. This has advantages over simpler methods of interpolation, such as nearest-neighbor interpolation, in that it provides a smoother approximation to the underlying "true" function.
- **Cubic**: Triangulation based on cubic interpolation. Images resampled with cubic interpolation are smoother and have fewer interpolation artifacts with respect to linear interpolation, but it requires more computational costs.

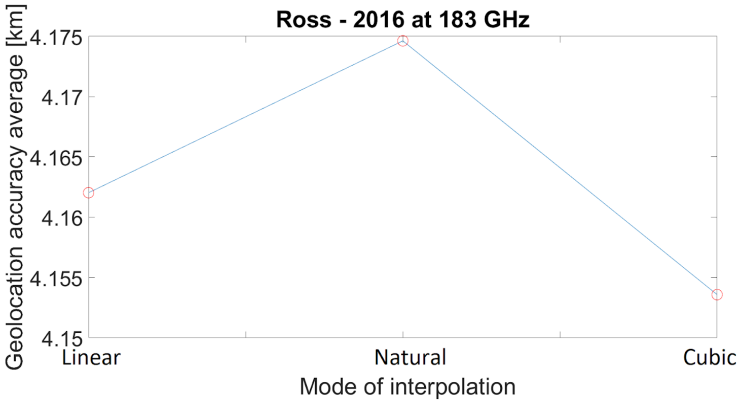

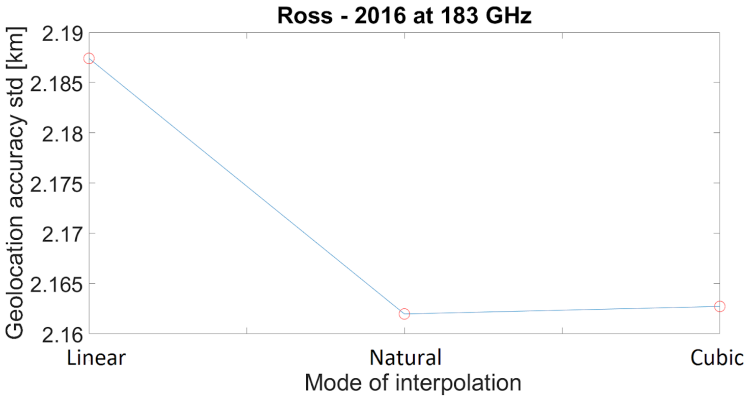

Figure 4.1.2.1: Results for Ross ice shelf in relation to upsampling methods. Geolocation accuracy average in the top and geolocation accuracy standard deviation in the bottom.

Table 4.1.2.1: Results for Ross ice shelf in relation to upsampling methods.

Interpolation method	Linear	Natural	Cubic
Geolocation accuracy average [km]	4.16	4.17	4.15
Geolocation accuracy standard deviation [km]	2.19	2.16	2.16

Calculating the standard deviation of the geolocation accuracy average for several interpolation methods it is possible to estimate the variance introduced by this step in the methodology. The obtained standard deviation is only 10 m. From observing Tab. 4.1.2.1, we can assume that the choice of interpolation method has only an insignificant impact on the results.

4.1.3 Sensitivity analysis to cross-correlation technique

The final step consists in evaluating the geolocation error using both a fast normalized cross-correlation (FNC) technique [27] and the registration in frequency domain (RFD) [29]. The cross correlation in space provides the normalized cross correlation matrix by directly correlating the two images (radiometric and SAR contours). The maximum of the correlation is then fitted by a 4th-order polynomial to reach sub-pixel accuracy. Conversely, the RFD

method correlates the two-dimensional Fourier transform of the two images with sub-pixel image registration. The two techniques are very similar so that we obtain very similar results, as shown in Fig. 4.1.3.1.

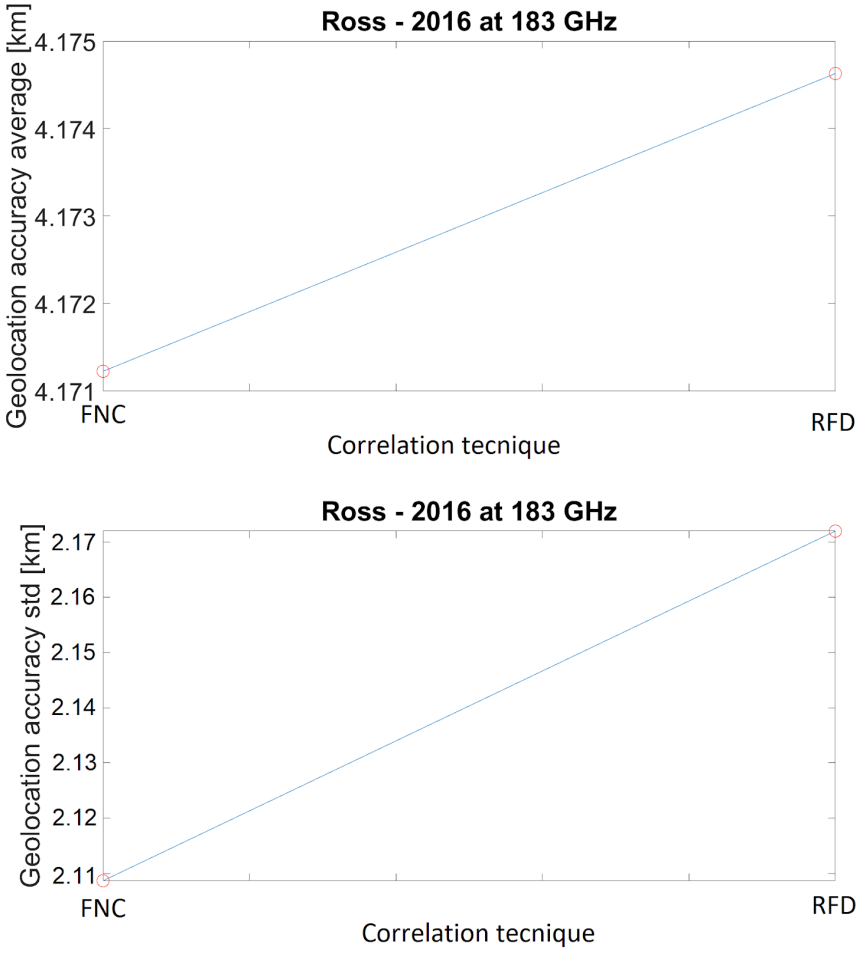

Figure 4.1.3.1: Results for Ross ice shelf in relation to correlation technique. Geolocation accuracy average in the top and geolocation accuracy standard deviation in the bottom.

Table 4.1.3.1: Results for Ross ice shelf in relation to upsampling methods.

Correlation technique	**FNC**	**RFD**
Geolocation accuracy average [km]	4.17	4.17
Geolocation accuracy standard deviation [km]	2.11	2.17

As a further parameter, we can calculate the standard deviation of the geolocation error average equal to 0.04 km. Between FNC and RFD we have almost the same results, because FNC is computed in the spatial domain whereas the RFD is computed in the frequency domain so that the small differences, highlighted in Tab. 4.1.3.1, are only due to numerics.

4.1.4 Overall sensitivity of the proposed methodology

To have an estimate of the methodology accuracy in presence of many error sources, we can recall the expression of the variance of a multivariate random function. For example, considering a random function $f(z)=x+y$ where x and y may represent additive zero-mean errors, its variance is given by:

$$\begin{aligned} < z^2 > \; = \; \sigma_z{}^2 = \; < (x+y)^2 > \; = \; < x^2 + y^2 + 2xy > \; = \\ = \; < x^2 > \; + \; < y^2 > \; + \; 2\, Cov\,(x,y) \end{aligned} \tag{4.1.4.1}$$

where the angle brackets stand for ensemble average. If it is possible to consider x and y statistically independent so that $Cov\,(x,y) = 0$, then it holds

$$< z^2 > \; = \; < x^2 > \; + \; < y^2 > \tag{4.1.4.2}$$

and the corresponding standard deviation is:

$$\sigma_z = \sqrt{(\,\sigma_x{}^2 + \sigma_y{}^2)} \tag{4.1.4.3}$$

The following Tab. 4.1.4.1 summarizes the standard deviation of the sensitivity analysis for each considered parameter, presented in Sec. 4.1.1, 4.1.2 and 4.1.3.

In all cases the number of samples of each sensitivity numerical experiment is relatively small so that the standard deviation σ should be better intended as a parametric variability Δ.

Table 4.1.4.1: Standard deviation or parametric variability derived from the sensitivity analysis to each parameter.

Sensitivity parameter	**Standard deviation or parametric variability [km]**
Interpolation-grid spatial resolution	0.62
Spatial interpolation method	0.01
Cross-correlation technique	0.04

Extending eq. (4.1.4.3) to more than 2 variables and assuming independent error contributions, it is possible to evaluate the overall accuracy of the methodology in terms of its standard deviation or parametric variability:

$$\Delta = \sqrt{(0.62^2 + 0.01^2 + 0.04^2)} \sim 0.62\ km \qquad (4.1.4.4)$$

Previous results confirm that the most important parameter in the geolocation assessment methodology is the spatial resolution of the interpolation grid. It is worth noting that this choice also influences the spatial upscaling of reference contour sources such as coastline database or SAR imagery.

It can be also important to understand the importance of the dataset size to obtain a stable geolocation error result in terms of average and standard deviation. In particular, Fig. 4.1.4.1 shows the geolocation error accuracy and its standard deviation against the number of samples, considering the Ross ice shelf (having 599 cloud-masked samples).

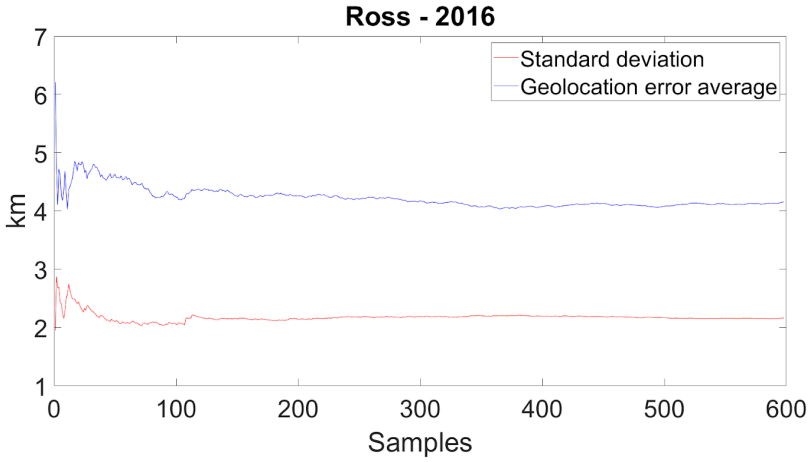

Figure 4.1.4.1. Geolocation error average (blue line) and standard deviation (red line) for Ross ice shelf using SSMIS F17 at 183± 6.6 GHz at H polarization.

Previous figure shows that the geolocation error average becomes stable with about 100 samples. To obtain a substantial stable value of the error standard deviation, about 70 samples seems to be enough.

4.1.5 Testing the nominal accuracy of geolocation error assessment

In order to evaluate the accuracy of the proposed TCM methodology, we can perform some numerical internal tests such as imposing an arbitrary and known geolocation error along latitude and/or longitude.

For example, let us consider an image over the Qinghai lake on 2016/11/11, as shown in Fig. 4.1.5.1

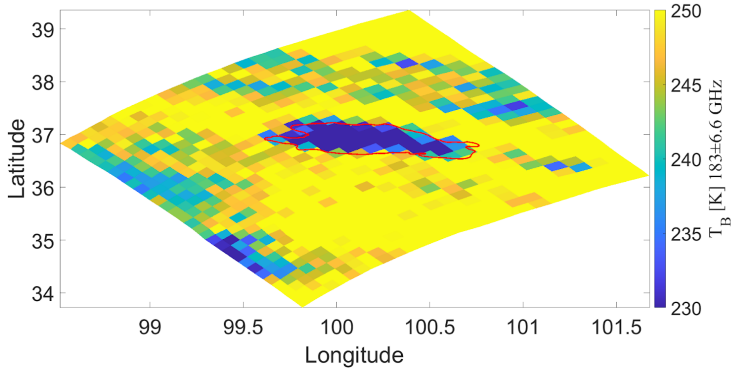

Figure 4.1.5.1: Brightness temperature image at 183±6.6 GHz H over the Qinghai lake with SSMIS F17 on 2016/11/11. The red line represents the GSHHG shoreline database.

Imposing a displacement only along latitude of +0.07°, which corresponds to about 7.78 km, we get what is shown in Figure 4.1.5.2.

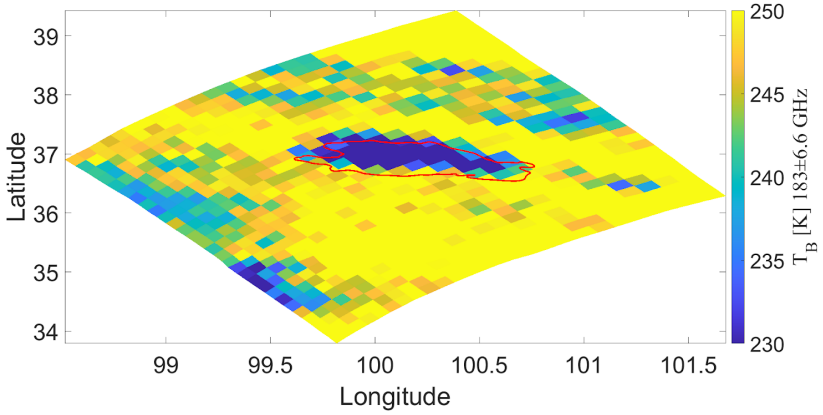

Figure 4.1.5.2: Brightness temperature image at 183±6.6 GHz H over the Qinghai lake with SSMIS F17 on 2016/11/11 with a displacement along latitude of 0.07°. The red line represents the GSHHG shoreline database.

Extracting the contours from both Fig. 4.1.5.1 and 4.1.5.2, we obtain the two curves in Fig. 4.1.5.3.

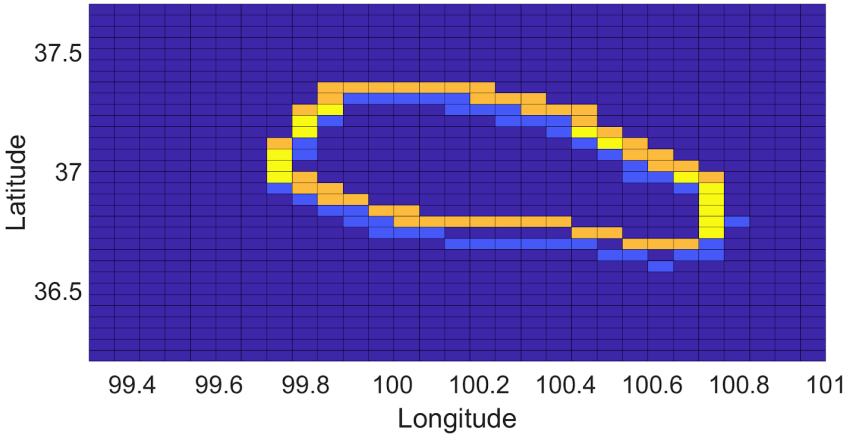

Figure 4.1.5.3: Extracted contour using Canny algorithm from original image (blue) and shifted image (yellow).

Cross-correlating the two contour curves, the proposed TCM methodology provides the following displacements:

- shift along latitude = 0.0636°
- shift along longitude = -0.0057°

The methodology returns a geolocation error of km 7.09, but with an error of 0.69 km respect to 7.78 km, that is the imposed geolocation error. Imposing also displacements both along latitude and longitude such as:

- shift along latitude = 0.06°
- shift along longitude = - 0.02 °

Using these values, we introduce an error of about 6.91 km, obtaining the two curves in Fig. 4.1.5.4.

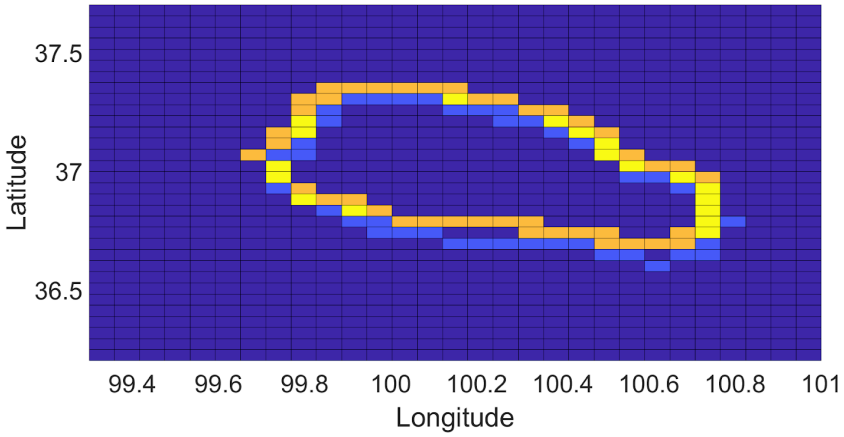

Figure 4.1.5.4: Extracted contour using the Canny algorithm from original image (blue) and shifted image (yellow).

Cross-correlating the two contour curves, the proposed methodology provides the following displacements:

- Shift along latitude = 0.0591°
- Shift along longitude = -0.0113°

The TCM methodology correctly returns the error along both directions with a displacement of 6.65 km, but with an error of 0.26 km. To better understand the accuracy of the results along longitude, we change the imposed displacements:

- shift along latitude = -0.04°
- shift along longitude = + 0.06 °

Using these values, we introduce an error of about 7.02 km, obtaining the two curves in Fig. 4.1.5.5.

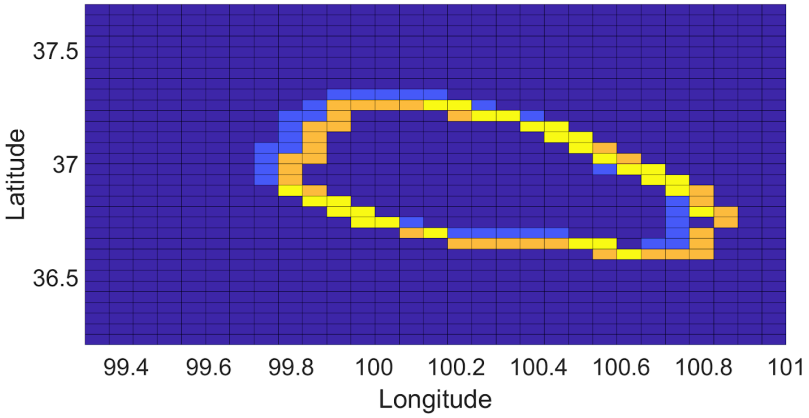

Figure 4.1.5.5: Extracted contour using the Canny algorithm from original image (blue) and shifted image (yellow).

Cross-correlating the two contour curves, the proposed methodology provides the following displacements:

- Shift along latitude = -0.0409°
- Shift along longitude = 0.0567°

The TCM methodology correctly returns the error along both directions with a displacement of 6.79 km, but with an error of 0.23 km. Imposing only a displacement along longitude:

- shift along latitude = 0.0°
- shift along longitude = - 0.08 °

Using these values, we introduce an error of about 7.25 km, obtaining the two curves in Fig. 4.1.5.6.

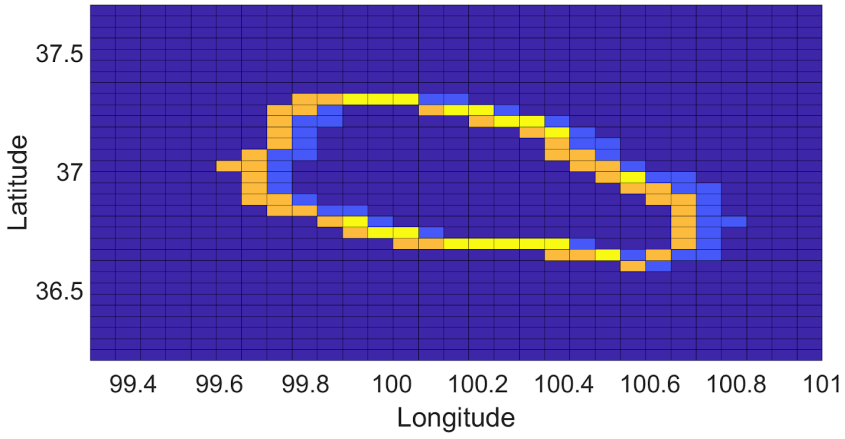

Figure 4.1.5.6: Extracted contour using the Canny algorithm from original image (blue) and shifted image (yellow).

Cross-correlating the two contour curves, the proposed TCM methodology provides the following displacements:

- Shift along latitude = 0,0°
- Shift along longitude = -0.0680°

The TCM methodology correctly returns the error along both directions with a displacement of 6.05 km, but with an error of 1.20 km. Considering another day for Qinghai lake, e.g. 2016/11/03 as shown in Fig. 4.1.5.7

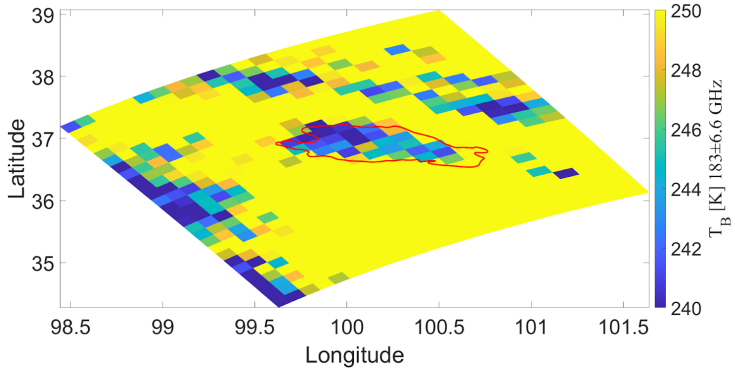

Figure 4.1.5.7: Brightness temperature image at 183±6.6 GHz H over the Qinghai lake with SSMIS F17 on 2016/11/03. The red line represents the GSHHG shoreline database.

Doing the same test again for this day, imposed a displacement only along latitude of +0.07°, which corresponds to about 7.78 km, we get what shown in Figure 4.1.5.8.

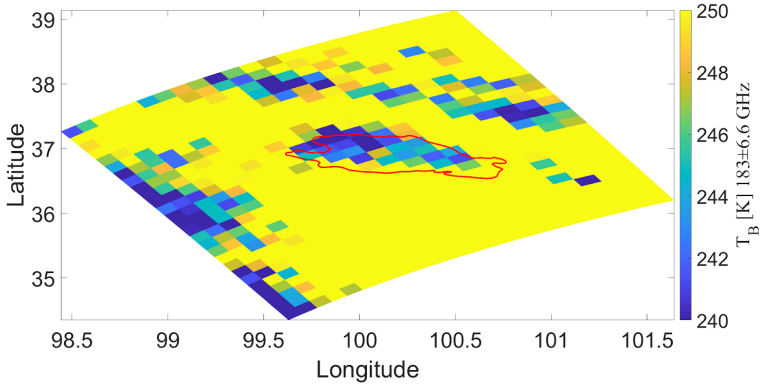

Figure 4.1.5.8: Brightness temperature image at 183±6.6 GHz H over the Qinghai lake with SSMIS F17 on 2016/11/03 with a displacement along latitude of 0.07°. The red line represents the GSHHG shoreline database.

Extracting the contours from both Fig. 4.1.5.7 and 4.1.5.8, we obtain the two curves in Fig. 4.1.5.9

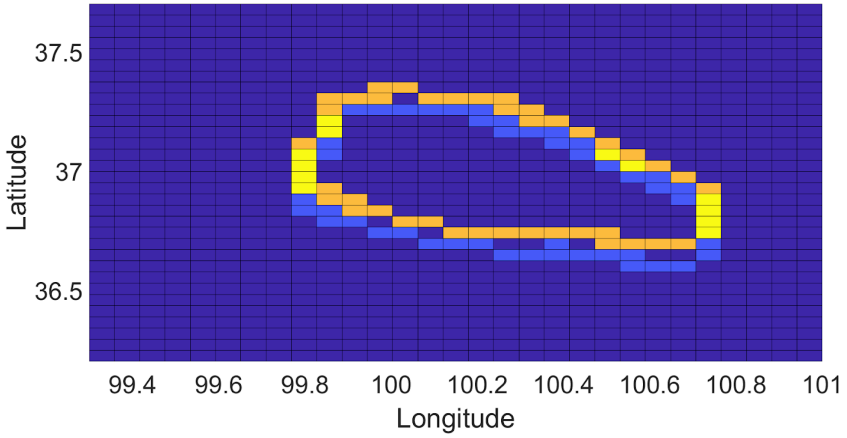

Figure 4.1.5.9: Extracted contour using Canny algorithm from original image (blue) and shifted image (yellow).

Cross-correlating the two contour curves, the proposed TCM methodology provides the following displacements:

- shift along latitude = 0.0727° (about 8.09 km)
- shift along longitude = 0.0°

The methodology correctly returns the error only along latitude, but with an error of 0.3 km. Let us impose the displacements both along latitude and longitude such as:

- shift along latitude = 0.06°
- shift along longitude = - 0.02 °

Using these values, we introduce an error of about 6.91 km, obtaining the two curves in Fig. 4.1.5.10.

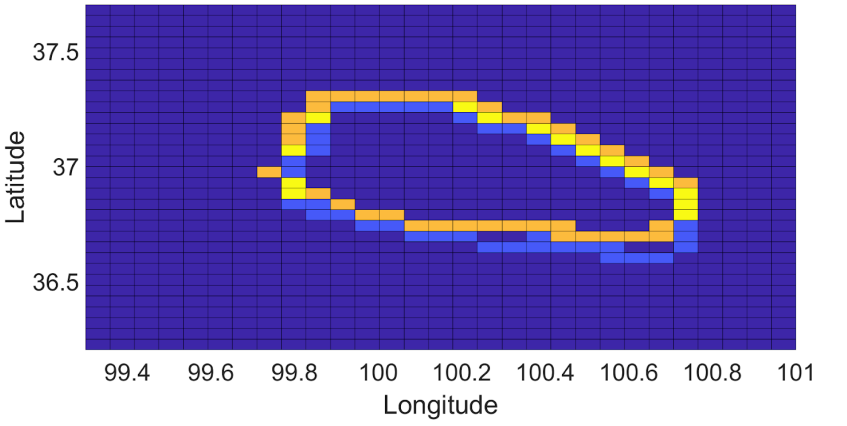

Figure 4.1.5.10: Extracted contour using the Canny algorithm from original image (blue) and shifted image (yellow).

Cross-correlating the two contour curves, the proposed methodology provides the following displacements:

- Shift along latitude = 0.0591°
- Shift along longitude = -0.0170°

The TCM methodology correctly returns the error along both directions with a displacement of 6.74 km, but with an error of 0.17 km. Let us impose the displacements both along latitude and longitude such as:

- shift along latitude = -0.04°
- shift along longitude = + 0.06 °

Using these values, we introduce an error of about 7.02 km, obtaining the two curves in Fig. 4.1.5.11.

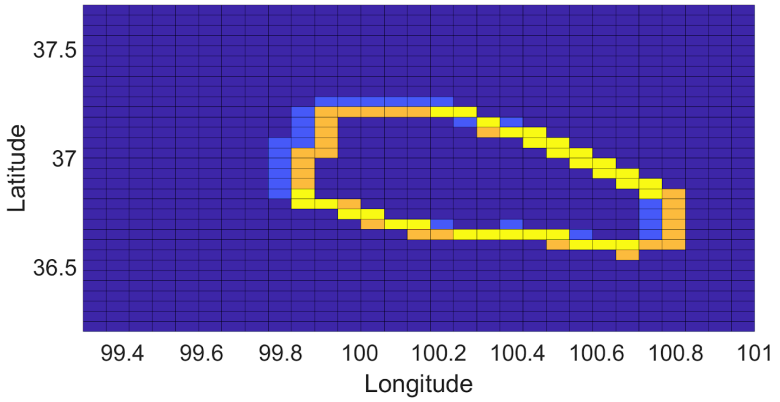

Figure 4.1.5.11: Extracted contour using the Canny algorithm from original image (blue) and shifted image (yellow).

Cross-correlating the two contour curves, the proposed methodology provides the following displacements:

- Shift along latitude = -0.0364 °
- Shift along longitude = 0.0567°

The TCM methodology correctly returns the error along both directions with a displacement of 6.46 km, but with an error of 0.56 km. Finally, imposing the displacements only along longitude:

- shift along latitude = 0.0°
- shift along longitude = - 0.08 °

Using these values, we introduce an error of about 7.25 km, obtaining the two curves in Fig. 4.1.5.12.

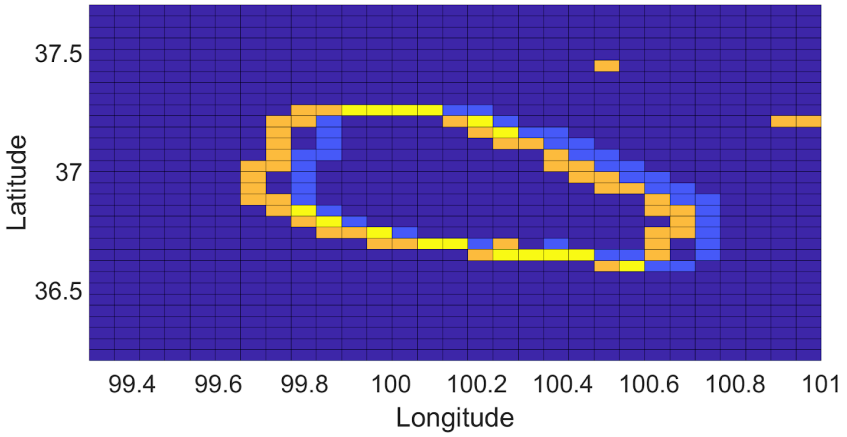

Figure 4.1.5.12: Extracted contour using the Canny algorithm from original image (blue) and shifted image (yellow).

Cross-correlating the two contour curves, the proposed methodology provides the following displacements:

- Shift along latitude = 0.0045°
- Shift along longitude = -0.0793°

The TCM methodology correctly returns the error along both directions with a displacement of 7.08 km, but with an error of 0.16 km.

Performing more robust tests for Ronne ice shelf and Qinghai lake, it is possible to generate 441 scenes adopting an arbitrary geolocation error with discrete step of 0.01° (the number 441 comes from the imposed 21 shifts along both latitude and longitude). For the Filchner-Ronne ice shelf tests, we have selected the cloud-masked images of two different days, i.e. 2016/06/21 and 2016/08/02 with high values of $I\left(\varepsilon, \Delta T_{Bm}\right)$ where I is the inference function described in detail in Appendix A, as a function of geolocation error ε and mean BT contrast ΔT_{Bm}. In particular, $I\left(\varepsilon, \Delta T_{Bm}\right)$ is 0.86 for 2016/06/21 and $I\left(\varepsilon, \Delta T_{Bm}\right)$ is 0.96 for 2016/08/02. The geolocation error estimate has been then computed for all the generated shifts.

Results are provided in 4.1.5.13 for the Filchner-Ronne (top figures) and Qinghai lake (bottom figures) as scatterplots between the imposed error and the retrieved one. The results for the Filchner-Ronne shelf on 2016/06/21 and 2016/08/02 show a mean difference between the imposed and retrieved errors of about 0.30 km and 0.25 km, respectively, with a standard deviation of about 0.52 km and 0.60 km. For the Qinghai Lake, a mean value of 0.23 km and standard deviation of 0.86 were obtained for the 2016/11/03 ($I\left(\varepsilon, \Delta T_{Bm}\right)$ =0.66) cloud-masked image and a mean value of 0.27 km and standard deviation of 0.58 for the 2016/11/10 ($I\left(\varepsilon, \Delta T_{Bm}\right)$ =0.56) cloud-masked image.

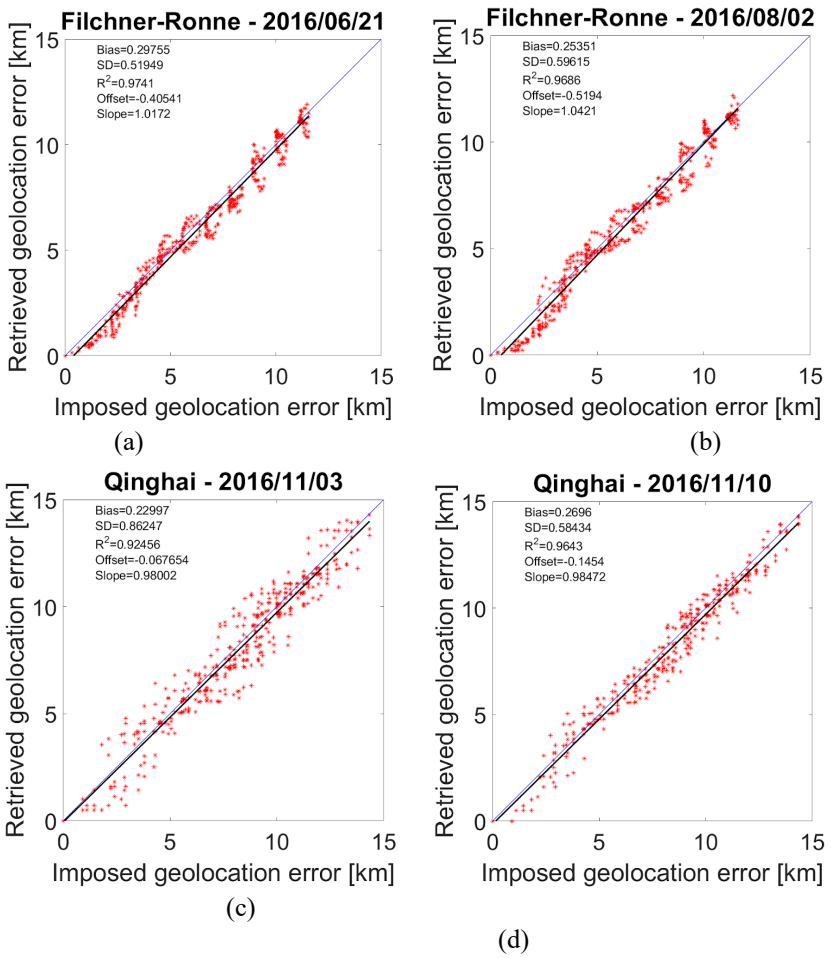

Figure 4.1.5.13: Sensitivity analysis of geolocation error assessment procedure based on TCM. a) Scatterplot between imposed geolocation error and retrieved one for Filchner-Ronne ice shelf target on 2016/04/15 and b) on 2016/05/20. c) Scatterplot between imposed and retrieved geolocation error using Qinghai lake as target on 2016/11/10 and d) on 2016/11/25.

The previous numerical tests show that the proposed TCM methodology can reconstruct with a fairly good accuracy the imposed geolocation errors, with a standard deviation lower than 1 km independently from the target. Indeed, this estimated standard deviation is lower than the requirement for an adequate error geolocation assessment of a spaceborne MW radiometer.

4.1.6 Sensitivity analysis to the target sample number

This section shows the sensitivity of the geolocation error assessment to the number of samples for all proposed targets.

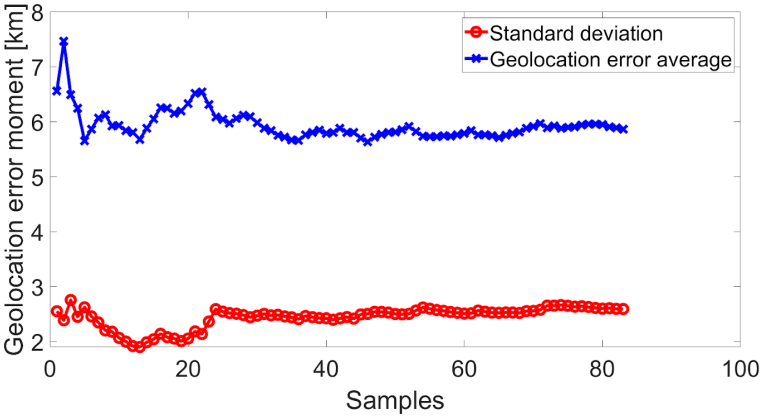

Figure 4.1.6.1: Geolocation error average (blue line) and standard deviation (red line) for Qinghai lake using SSMIS F17 at 183±6.6 GHz (H).

As an example, Fig. 4.1.6.1 reports the behaviour of the average geolocation accuracy and relative standard deviation with respect to the number of available images for Qinghai lake.

In order to estimate the minimum number of samples necessary to have the convergence of the results, we can introduce the relative difference of average mean error $\delta_\varepsilon(n)$ and the relative difference of average standard deviation $\delta_\sigma(n)$ as:

$$\delta_\varepsilon(n) = \frac{\varepsilon(n) - m_e}{m_e} 100 \quad (4.1.6.1)$$

$$\delta_{\sigma_\varepsilon}(n) = \frac{\sigma_\varepsilon(n) - m_\sigma}{m_\sigma} 100 \quad (4.1.6.2)$$

where:

- $\varepsilon(n)$ is the average of the geolocation displacement obtained considering the first n samples
- m_ε is the average of the geolocation displacement obtained considering all samples
- $\sigma_\varepsilon(n)$ is the average of the standard deviation of geolocation displacement obtained considering the first n samples
- m_σ is the average of the standard deviation of geolocation displacement obtained considering all samples

Note that both $\delta_\varepsilon(n)$ and $\delta_\sigma(n)$ are percentage values.

Setting arbitrary thresholds for both relative differences, we can impose the convergence of results when it happens simultaneously that:

$$\delta_{\varepsilon}(n) < \delta_{\varepsilon\, th} \quad (4.1.6.3)$$

$$\delta_{\sigma}(n) < \delta_{\sigma\, th} \quad (4.1.6.4)$$

where it holds:

- $\delta_{\varepsilon\, th}$ is the threshold for the average of geolocation displacement
- $\delta_{\sigma\, th}$ is the threshold for the average of standard deviation of geolocation displacement

Considering for simplicity the same percentage threshold δ_{th} for eq. (4.1.6.3) and (4.1.6.4), it is possible to write the following overall condition for the minimum optimal number n_{opt}:

$$n_{opt} = n \mid [\delta_{\varepsilon}(n) < \delta_{th} \;\&\; \delta_{\sigma}(n) < \delta_{th}] \quad (4.1.6.5)$$

The number n_{opt} of samples that satisfies the previous eq. (3.5.6.5) could be considered the minimum optimal number of target necessary samples to reach a convergence for both mean and standard deviation of the geolocation error. Moreover, considering the detectability/day number n_{dd}, summarized in Tab. 3.1.1, it is possible to transform the n_{opt} into the minimum optimal number $n_{opt\, dd}$ of necessary days, needed to satisfy eq. (4.1.6.5), in the following way:

$$n_{opt\, dd} = \frac{n_{opt}}{n_{dd}} \quad (4.1.6.6)$$

For example, in the case of lake and mountain chain targets, whose detectability/day is about 1, we obtain $n_{opt\, dd} = n_{opt}$.

Fig. 4.1.6.2 shows the relation between n_{opt} and δ_{th} where δ_{th} assuming values from 0.5% to 5% with a step of 0.5%, as shown by the marker in Fig. 4.1.6.2. As expected, relaxing the threshold, n_{opt} decreases.

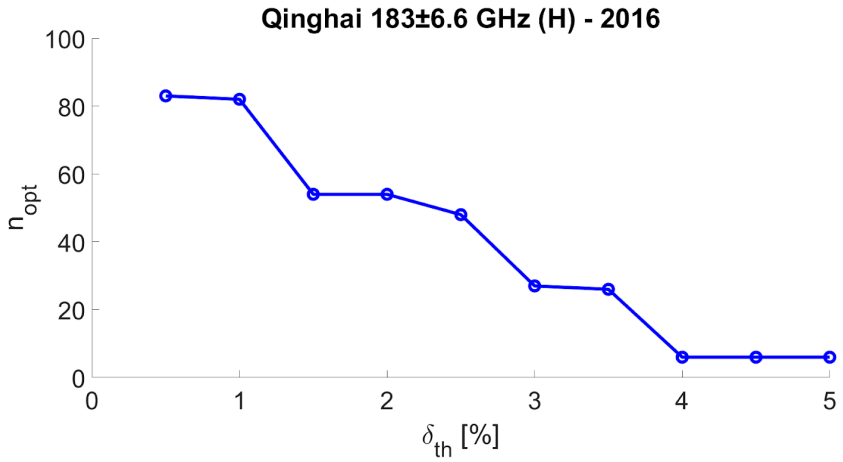

Figure 4.1.6.2: Relation between the minimum number of necessary samples (n_{opt}) *and* δ_{th} *threshold for Qinghai lake using SSMIS F17 at 183±6.6 GHz (H).*

Since δ_{th} is a percentage value, then the finite difference (in km) between $\varepsilon(n_{opt})$ and m_ε and between $\sigma_\varepsilon(n)$ and m_σ samples depends on the target, as shown in the following eq. (4.1.6.7) and (4.1.6.8):

$$\Delta\varepsilon = |\varepsilon(n_{opt}) - m_\varepsilon| = |\frac{\delta_{th}}{100} m_\varepsilon| \quad (4.1.6.7)$$

$$\Delta\sigma_\varepsilon = |\sigma_\varepsilon(n_{opt}) - m_\sigma| = |\frac{\delta_{th}}{100} m_\sigma| \quad (4.1.6.8)$$

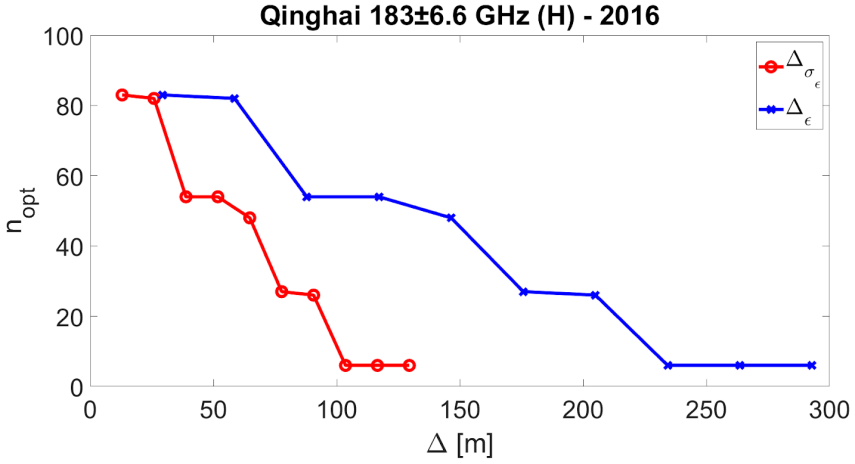

Figure 4.1.6.3: Relation between the minimum number of necessary samples (n_{opt}) *and* Δ_ε *in blue and between the minimum number of necessary samples* (n_{opt}) *and* $\Delta_{\sigma_\varepsilon}$ *for Qinghai lake using SSMIS F17 at 183±6.6 GHz (H).*

Below a similar approach is carried out for all other considered targets. In particular, grouping them depending on their different nature, e.g, lakes/bays, mountains, shelves and straits, it is possible to produce a set of three figures for each type of target, as shown in Fig. 4.1.6.4 and 4.1.6.5.

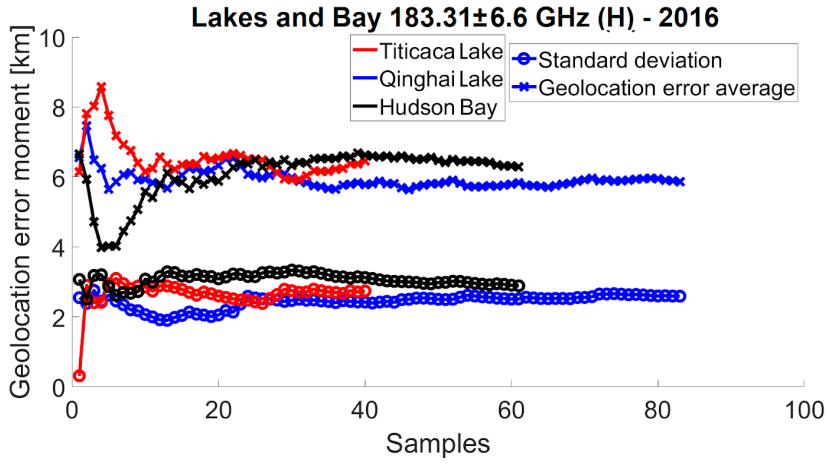

Figure 4.1.6.4: Geolocation error average (x markers) and standard deviation (o markers) for Qinghai lake (red line), Titicaca lake (blue line) and Hudson bay (black line) using SSMIS F17 at 183±6.6 GHz (H).

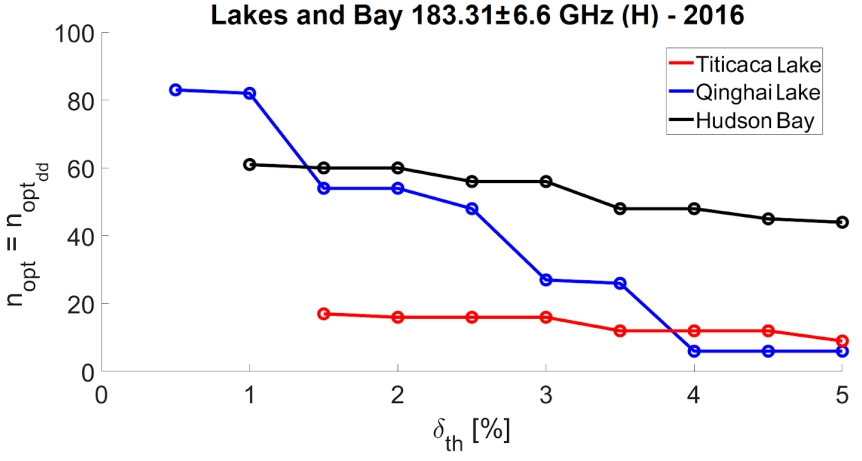

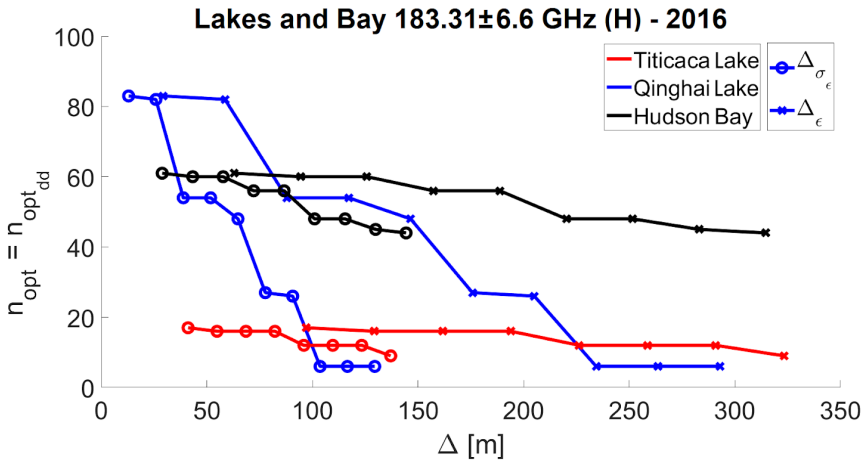

Figure 4.1.6.5: (Top panel) Relation between the minimum number of necessary samples (n_{opt}) and δ_T threshold. (Bottom panel) Relation between the minimum number of necessary samples (n_{opt}) and Δ_ε with 'x' markers and between the minimum number of necessary samples (n_{opt}) and $\Delta_{\sigma_\varepsilon}$ with 'o' markers. The results are shown for Qinghai lake with red line, for Titicaca lake with blue line and for Hudson bay with black line.

The following Fig. 4.1.6.6 and Fig. 4.1.6.7 report the results and the minimum number of necessary samples for Antarctic ice shelves.

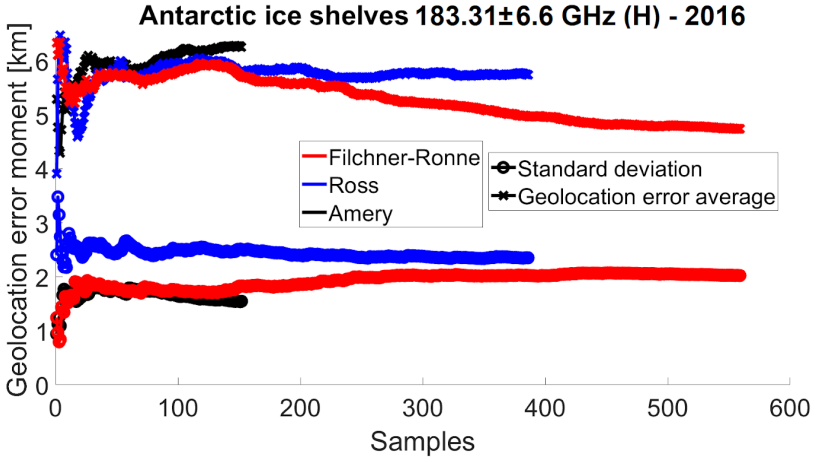

Figure 4.1.6.6: Geolocation error average (x markers) and standard deviation (o markers) for Ross ice shelf (red line), Filchner-Ronne ice shelf (blue line) and Amery ice shelf (black line) using SSMIS F17 at 183±6.6 GHz (H).

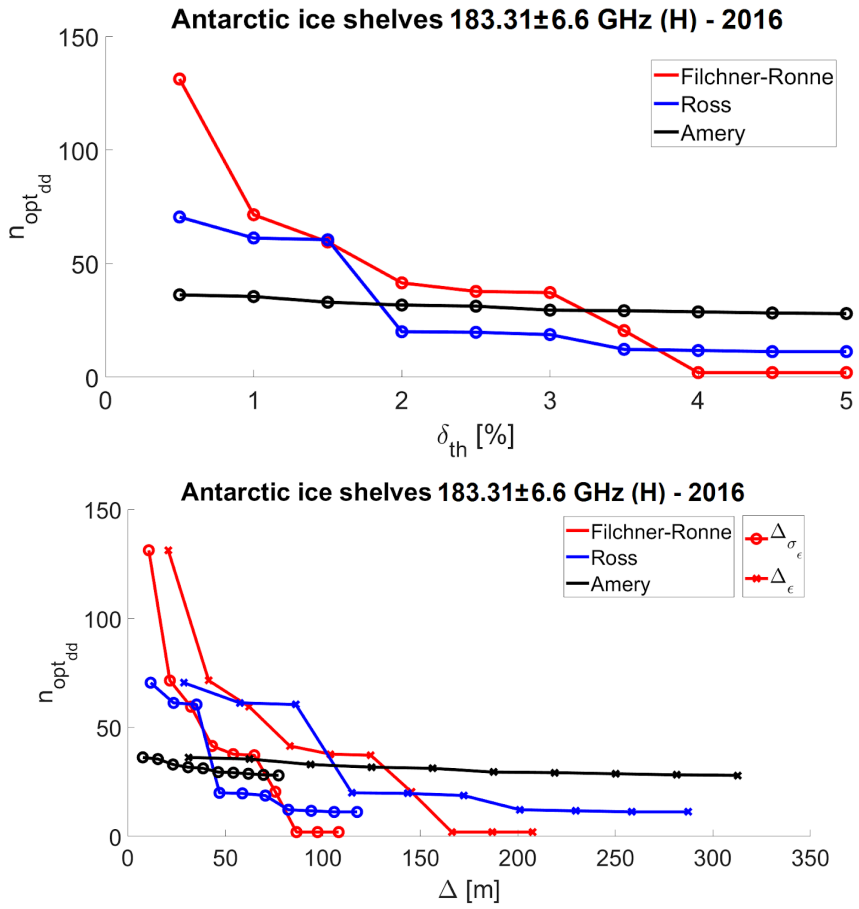

Figure 4.1.6.7: (Top panel) Relation between the minimum number of necessary samples (n_{opt}) *and* δ_T *threshold. (Bottom panel) Relation between the minimum number of necessary samples* (n_{opt}) *and* Δ_ε *with 'x' markers and between the minimum number of necessary samples* (n_{opt}) *and* $\Delta_{\sigma_\varepsilon}$ *with 'o' markers. The results are shown for Ross ice shelf with red line, for Filchner-Ronne ice shelf with blue line and Amery ice shelf with black line.*

Considering the eq. (4.1.6.6) with $n_{dd} = 4$ for ice shelves, it is possible to obtain the Fig. 4.1.6.8, that reports the minimum number of days necessary to obtain the convergence.

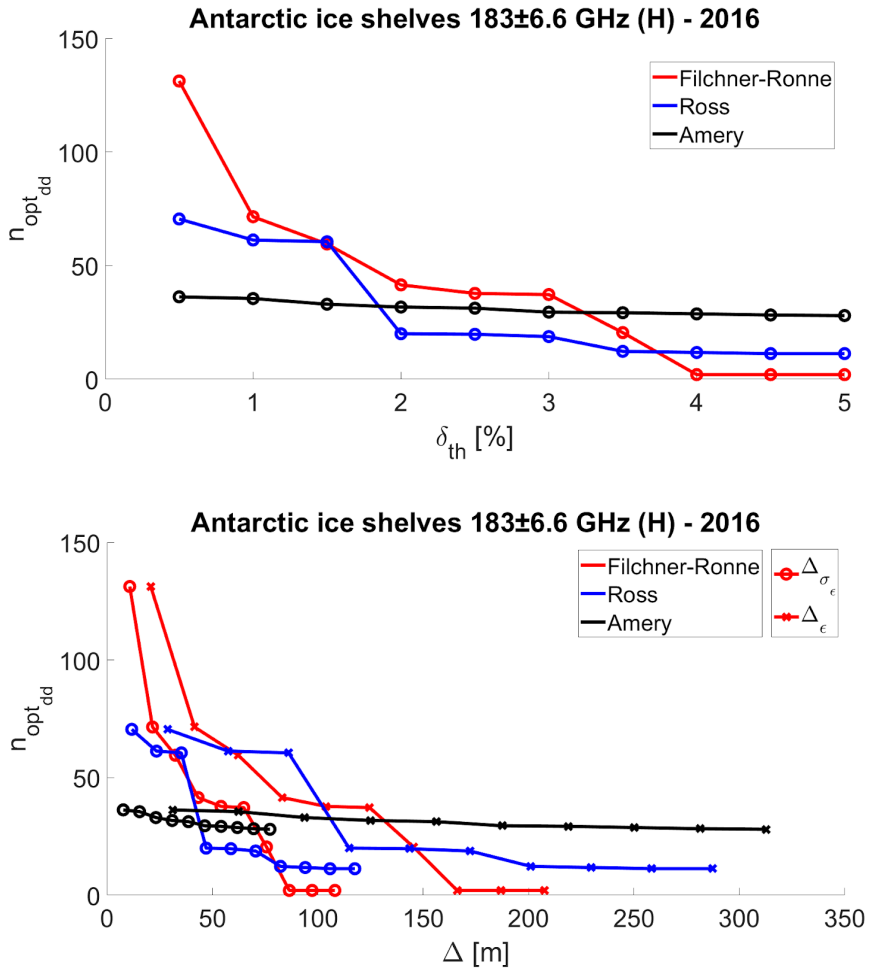

Figure 4.1.6.8: (Top panel) Relation between the minimum optimal number $n_{opt\,dd}$ of necessary days and δ_T threshold. (Bottom panel) Relation between minimum optimal number $n_{opt\,dd}$ of necessary days and Δ_ε with 'x' markers and between minimum optimal number $n_{opt\,dd}$ of necessary days and $\Delta_{\sigma_\varepsilon}$ with 'o' markers. The results are shown for Ross ice shelf with red line, for Filchner-Ronne ice shelf with blue line and Amery ice shelf with black line.

The following Fig. 4.1.6.9 and Fig. 4.1.6.10 report the results and the minimum number of necessary samples for Karakorum and Andean chains.

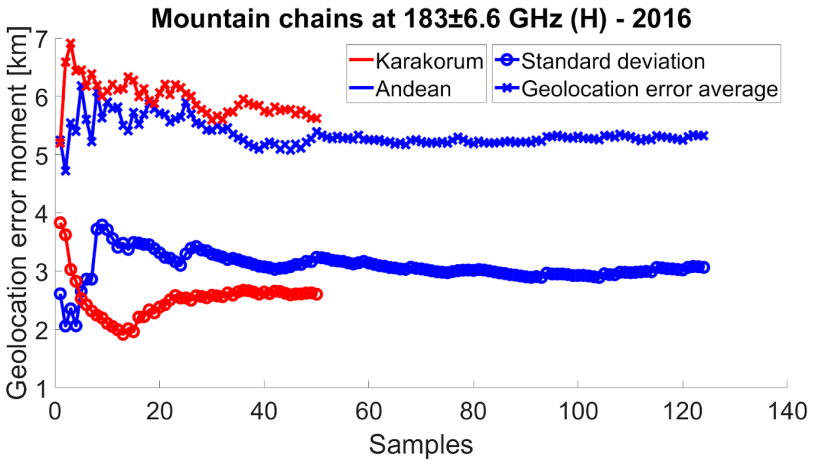

Figure 4.1.6.9: Geolocation error average (x markers) and standard deviation (o markers) for Karakorum mountains (red line) and Andean chain (blue line) using SSMIS F17 at 183±6.6 GHz (H).

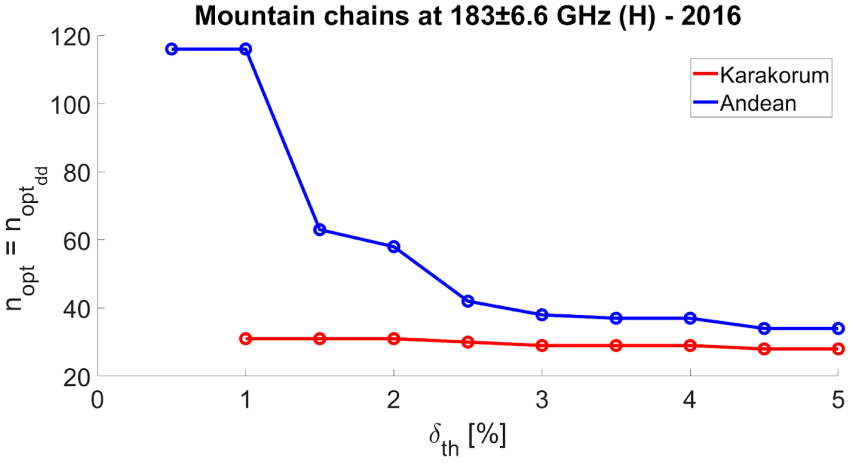

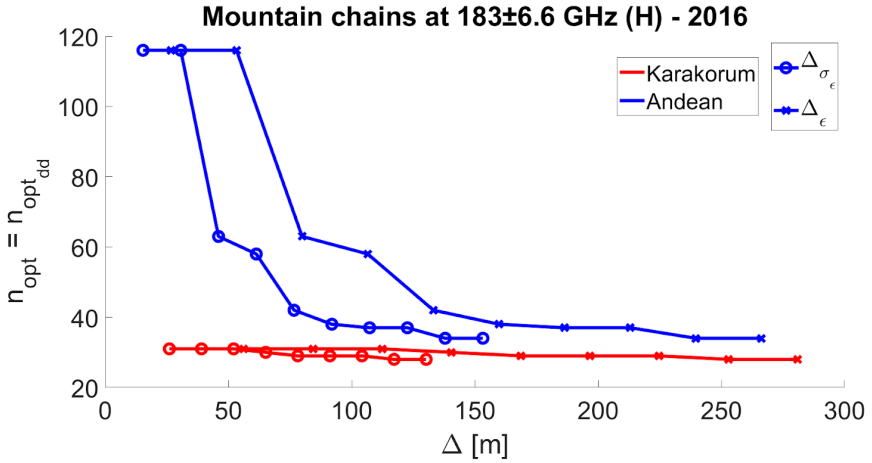

Figure 4.1.6.10: (Top panel) Relation between the minimum number of necessary samples (n_{opt}) and δ_T threshold. (Bottom panel) Relation between the minimum number of necessary samples (n_{opt}) and Δ_ε with 'x' markers and between the minimum number of necessary samples (n_{opt}) and $\Delta_{\sigma_\varepsilon}$ with 'o' markers. The results are shown for Karakorum mountains with red line and Andean mountains with blue line.

Fig. 4.1.6.11 and Fig. 4.1.6.12 report the results and the minimum number of necessary samples for Nares Strait.

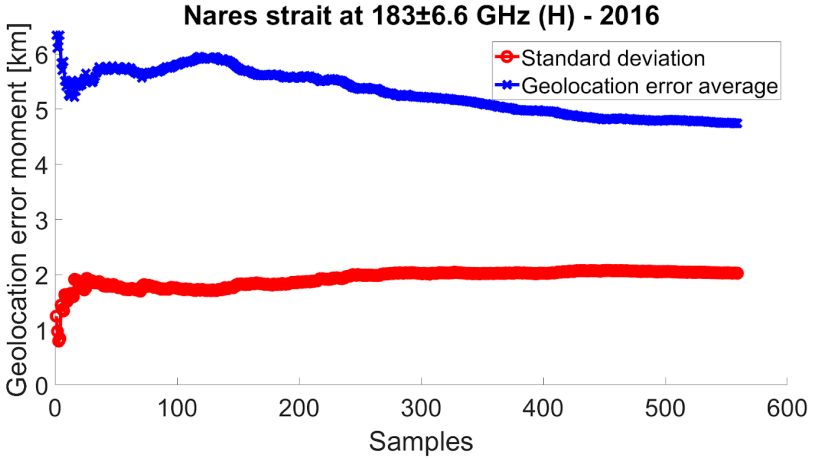

Figure 4.1.6.11: Geolocation error average (x markers) and standard deviation (o markers) for Nares Strait using SSMIS F17 at 183±6.6 GHz (H).

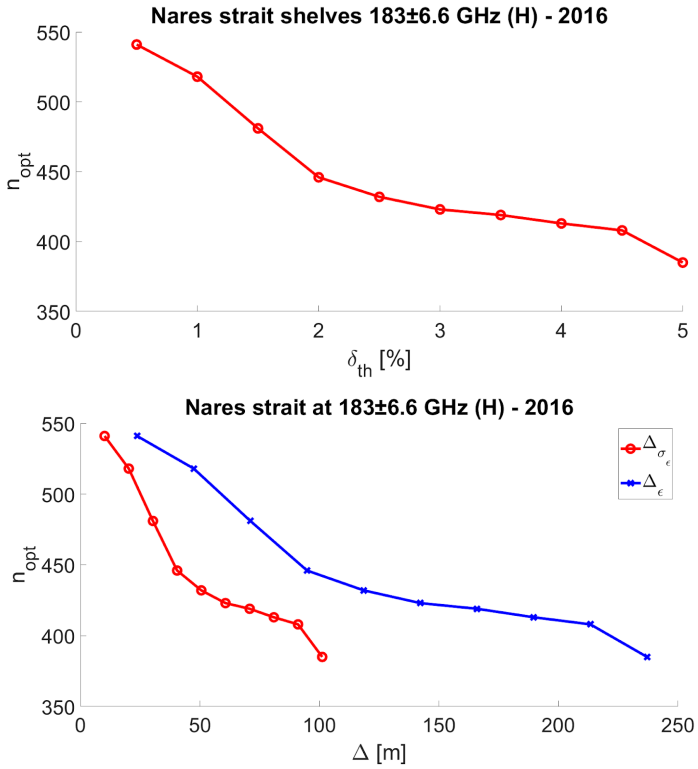

Figure 4.1.6.12: (Top panel) Relation between the minimum number of necessary samples (n_{opt}) *and* δ_T *threshold. (Bottom panel) Relation between the minimum number of necessary samples* (n_{opt}) *and* Δ_ε *with 'x' markers and between the minimum number of necessary samples* (n_{opt}) *and* $\Delta_{\sigma_\varepsilon}$ *with 'o' markers. The results are shown for for Nares Strait*

Considering the eq. (4.1.6.6) with $n_{dd} = 4$ for Nares Strait, it is possible to obtain the Fig. 4.1.6.13, that reports the minimum number of days necessary to obtain the convergence.

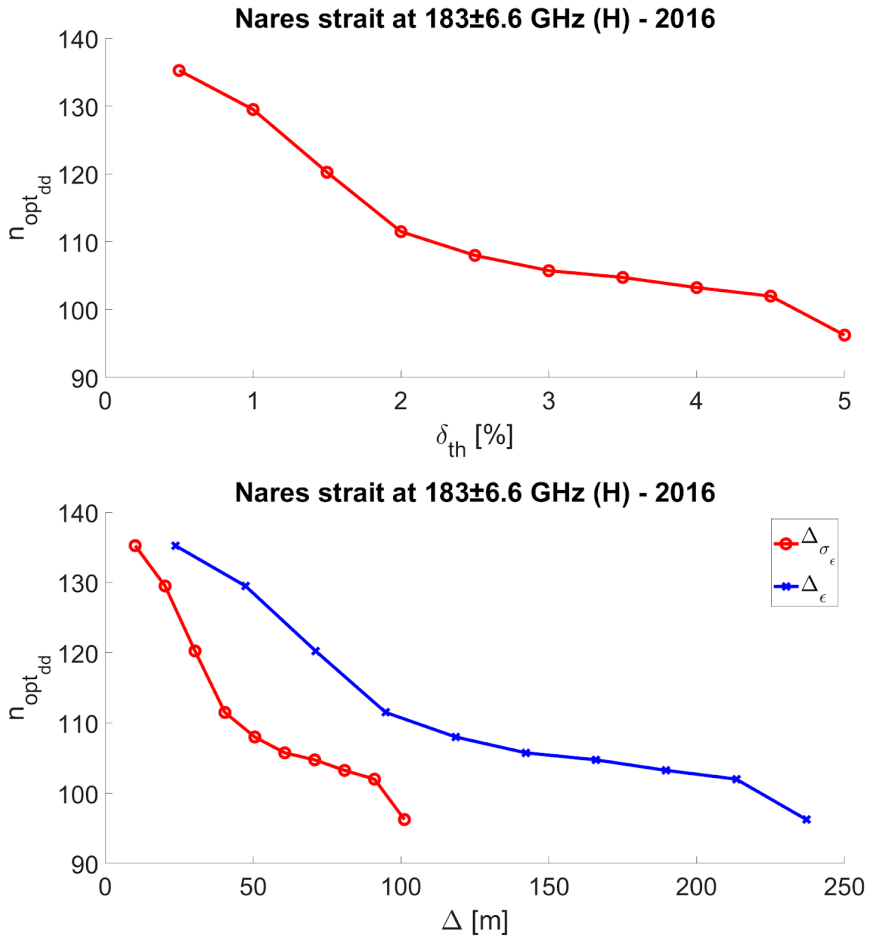

Figure 4.1.6.13: (Top panel) Relation between the minimum optimal number $n_{opt\,dd}$ and δ_T threshold. (Bottom panel) Relation between the the minimum optimal number $n_{opt\,dd}$ and Δ_ε with 'x' markers and between the minimum optimal number $n_{opt\,dd}$ and $\Delta_{\sigma_\varepsilon}$ with 'o' markers. The results are shown for for Nares Strait

In summary, the following Tab. 4.1.6.1 resumes n_{opt} and $n_{opt\,dd}$ obtained for all targets, setting the threshold δ_{th} to 1% and 2%.

Table 4.1.6.1: Summary of n_{opt} and $n_{opt\ dd}$ for all surface targets

Target	$\delta_{th} = 1\%$		$\delta_{th} = 2\%$	
	n_{opt}	$n_{op\ tdd}$	n_{opt}	$n_{opt\ dd}$
Qinghai lake	82	82	54	54
Karakorum mountains	31	31	31	31
Hudson Bay	61	61	60	60
Nares strait	518	130	446	112
Ross ice shelf	286	72	166	42
Filchner-Ronne ice shelf	245	62	80	20
Amery ice shelf	142	36	127	31
Titicaca lake	-	-	16	16

Note that in case of Titicaca lake for $\delta_{th} = 1\%$, we do not indicate n_{opt} because we need all samples to respect this threshold.

4.2. ICI FREQUENCY-SCALING ASSESSMENT

In order to simulate the spaceborne ICI BT and slant-path attenuation, we have adopted a 1D radiative transfer model (with no scattering) using ERA-5 or radiosoundings (RAOB) as input atmospheric vertical profiles. In particular:

- ERA-5 data cover the Earth on a 30-km resolution grid and resolve the atmosphere using 137 levels from the surface up to a height of 80 km. The used atmospheric radiosoundings are distributed from University of Wyoming for many stations around the world. Tab. 4.2.1 summarizes the considered data sources.
- To obtain a more realistic simulated scenario, it is essential to have a good representation of the surface emissivity. For this purpose we have adopted the surface-emissivity models TELSEM2 for water surface and TESSEM2 for land surface.

Table 4.2.1: Summary of web sites to download atmospheric information

Data	**Web Site**
ERA-5	https://cds.climate.copernicus.eu/#!/search?text=ERA5&type=dataset
Atmospheric soundings	http://www.weather.uwyo.edu/upperair/sounding.html

4.2.1 SSMIS measured imagery

Considering the existing data provided from SSMIS F17 instrument it is possible to observe the differences between 150 GHz H and 183±6.6 GHz H. Fig. 4.2.1.1 shows that difference for Titicaca lake on 15/07/2016 and the BT contrast between land and water is, as expected, greater at 150 GHz. Also Fig. 4.2.1.2 and Fig. 4.2.1.3 confirm that observation.

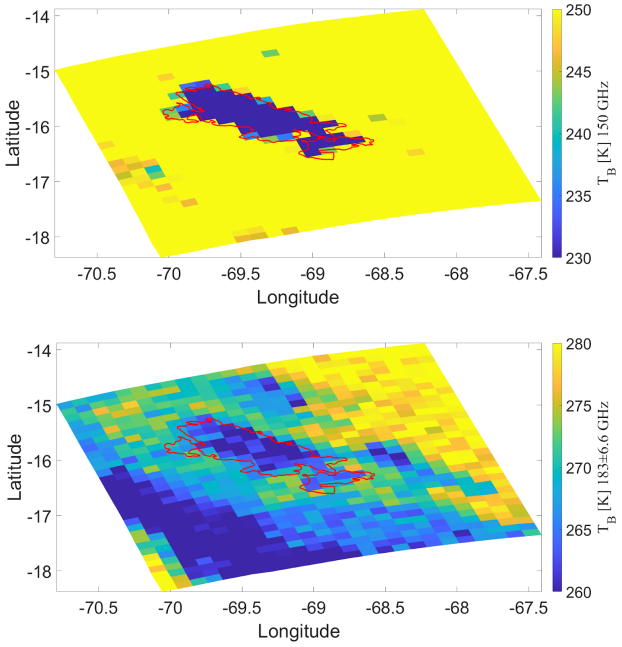

Figure 4.2.1.1: BT over Titicaca lake on 15/07/2016 at 150 GHz (left) and 183 ±6.6 GHz (right).The red line represents the Titicaca lake from GSHHG database at full resolution.

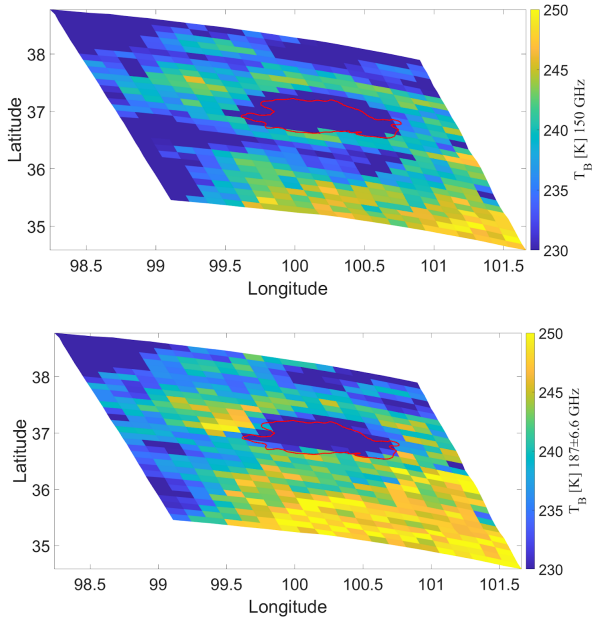

Figure 4.2.1.2: BT over Qinghai lake on 11/11/2016 at 150 GHz (left) and 183 ±6.6 GHz (right).The red line represents the Qinghai lake from GSHHG database at full resolution.

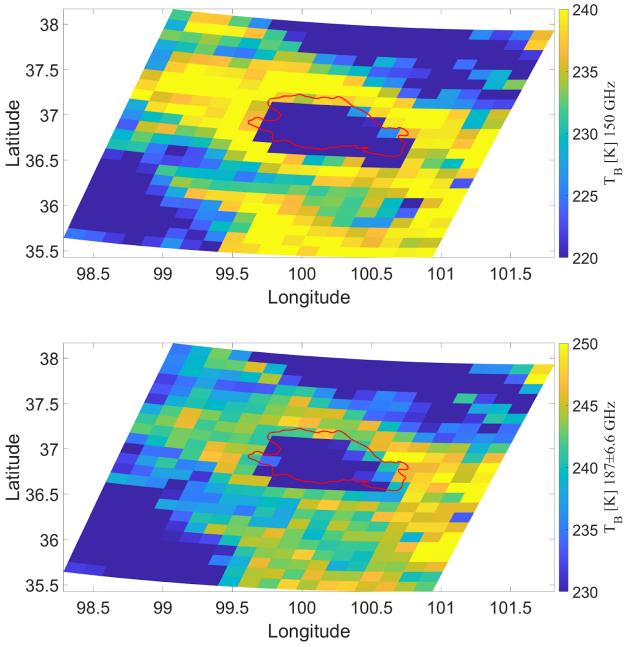

Figure 4.2.1.3: BT over Qinghai lake on 30/11/2016 at 150 GHz (left) and 183 ±6.6 GHz (right).The red line represents the Qinghai lake from GSHHG database at full resolution.

It is very useful to observe SSMIS-8 (150 GHz in horizontal polarization), because it can be used also to have an idea what we will see with ICI-4 (H) as will be explained in the next Sub-sec. 4.2.2 and 4.2.3.

4.2.2 Simulation using radiosounding profiles

Using atmospheric sounding it is possible to simulate BT in a single point, for example wanting to simulate the Antarctic area we can choose a station in Fig. 4.2.2.1.

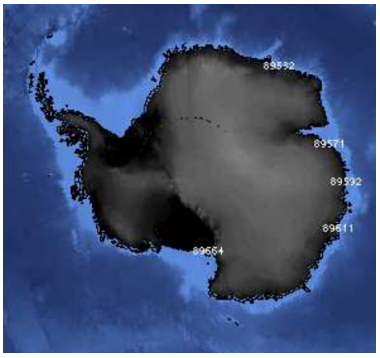

Figure 4.2.2.1: Available weather stations on Antarctica region which atmospheric sounding

Fig. 4.2.2.1 shows that a weather station is located within Ross ice shelf, i.e. the station 89664 of McMurdo. Using data available for this station, it is possible to simulate spaceborne BTs for different ICI channel frequencies. The numerical simulations in this case are provided setting a constant surface emissivity. Fig. 4.2.2.2 reports the relation between 150 GHz and 243 GHz for simulations on McMurdo station from 01 June 2016 to 31 October 2016. Within this period we have almost two radiosoundings per day, obtaining a dataset containing 299 samples.

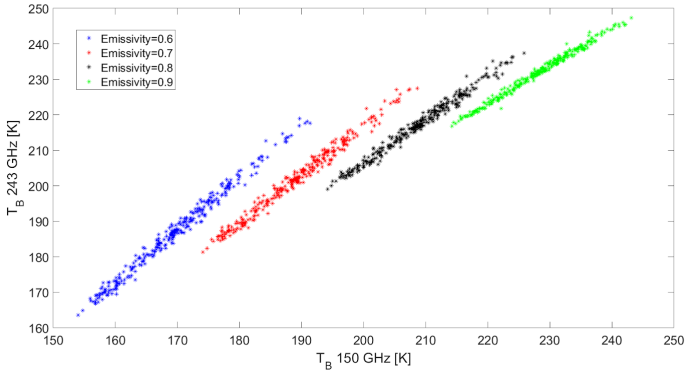

Figure 4.2.2.2: Relation between 150 GHz and 243 GHz for simulations on McMurdo station from 01 June 2016 to 31 October 2016. Blue markers are the results for 0.6 of surface emissivity. Red points indicate surface emissivity of 0.7. Black markers are the results for surface emissivity of 0.8. Green markers are the results for 0.9 of surface emissivity at 53° view angle.

Fig. 4.2.2.2 shows a linear relation between 150 GHz and 243 GHz, especially for lower values of surface emissivity. Tab. 3.6.2.1. Contains the equations of the linear regression that allow to approximate 243 GHz from 150 GHz.

Table 4.2.2.1: BT frequency-scaling relation from 150 GHz and 243 GHz for several surface emissivity

Emissivity	Equation (BT in K)
0.6	$T_{B_{243}} = 1.5\ T_{B_{150}} - 65$
0.7	$T_{B_{243}} = 1.4\ T_{B_{150}} - 56$
0.8	$T_{B_{243}} = 1.2\ T_{B_{150}} - 38$
0.9	$T_{B_{243}} = 1.1\ T_{B_{150}} - 11$

Fig. 4.2.2.3 and Fig. 4.2.2.4 show the relation between 183 GHz and 243 GHz and between 150 GHz and 183 GHz, respectively. No close linear relationships were found between these pairs of channels.

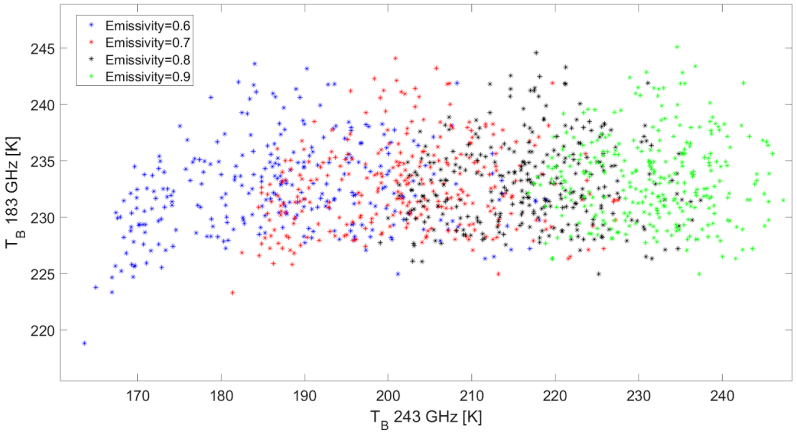

Figure 4.2.2.3: Relation between 183 GHz and 243 GHz for simulations on MCMurdo station from 01 June 2016 to 31 October 2016. Blue markers are the results for 0.6 of surface emissivity. Red points indicate surface emissivity of 0.7. Black markers are the results for surface emissivity of 0.8. Green markers are the results for 0.9 of surface emissivity at 53° view angle.

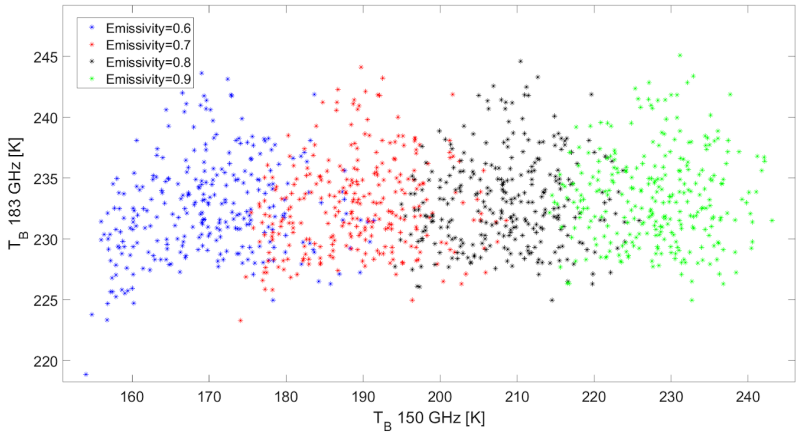

Figure 4.2.2.4: Relation between 150 GHz and 183 GHz for simulations on MCMurdo station from 01 June 2016 to 31 October 2016. Blue markers are the results for 0.6 of surface emissivity. Red points indicate surface emissivity of 0.7. Black markers are the results for surface emissivity of 0.8. Green markers are the results for 0.9 of surface emissivity at 53° view angle.

Fig. 4.2.2.5 shows the attenuation for 150 GHz, 183 GHz and 243 GHz.

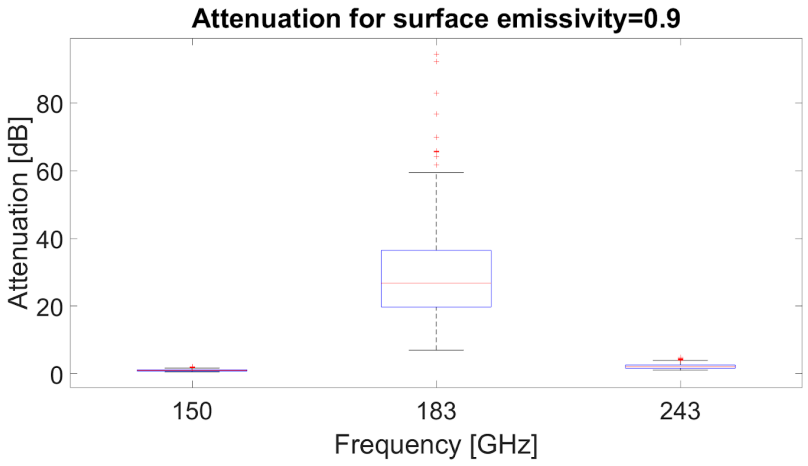

Figure 4.2.2.5: Simulated attenuation obtained using radiosaudings over MCMurdo station for an emissivity of 0.9 at 53° view angle.

The attenuation of 243 GHz is higher with respect to 150 GHz, as highlighted in Fig. 4.2.2.6. However, the attenuation at 243 GHz is lower than at 183 GHz, so it will allow to see more surface targets with higher BT contrast at 243 GHz.

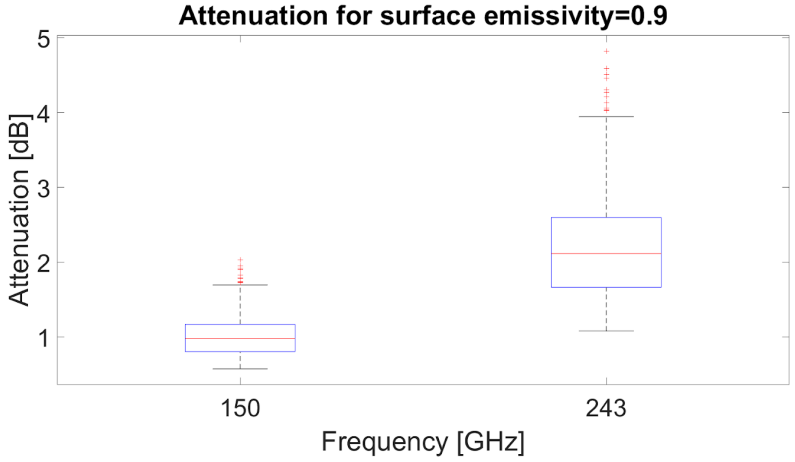

Figure 4.2.2.6: Simulated attenuation obtained using radiosaudings over MCMurdo station for an emissivity of 0.9 at 53° view angle

4.2.3 Simulation using ERA-5 clear-air scenarios

Using ERA-5 data as input for atmospheric vertical profiles, it is possible to simulate an entire scene and its BT map. In this respect, it is very important to properly characterize the surface emissivity knowing its nature as well as the observation geometry and central frequency. Input information to TELSEM2 and TESSEM2 recent and state-of-the-art models, described in [30], are listed in Tab. 4.2.3.1.

Tab. 4.2.3.1: Information needed to compute the emissivity for land and water surface

Type of surface	**Input data**
Land (TELSEM2)	Viewing angle of view, frequency, geographical coordinates
Water (TESSEMS2)	Viewing angle, frequency, surface wind velocity, surface temperature, water salinity

Providing the input data of Tab. 4.2.3.1 for the Qinghai lake at 183 GHz, we can simulate the surface emissivity as in Fig. 4.2.3.1 both at horizontal and vertical polarization using ERA5 on 1 December 2016 at 11:00 am.

Using surface emissivity maps of Fig, 4.2.3.1, it is then possible to simulate spaceborne BTs and the slant-path attenuation at 183±7 GHz, both at horizontal polarization (as the case of SSMIS) and at vertical polarization (as the case of ICI). For the ICI-1 at 183±7 GHz results for the BT and slant-path attenuation are shown in Fig. 4.2.3.2.

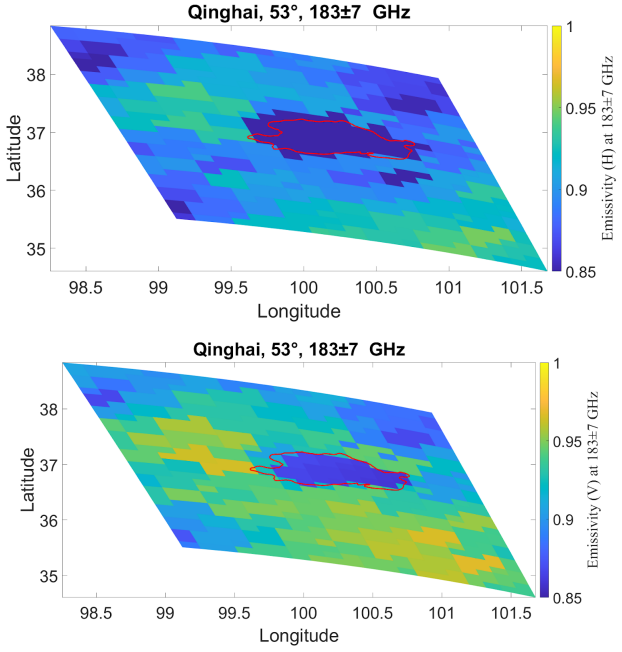

Figure 4.2.3.1: Simulated surface emissivity at 183±7 GHz using TELSEM2 and TESSEM2. The red line represents the Qinghai lake from GSHHG database at full resolution.

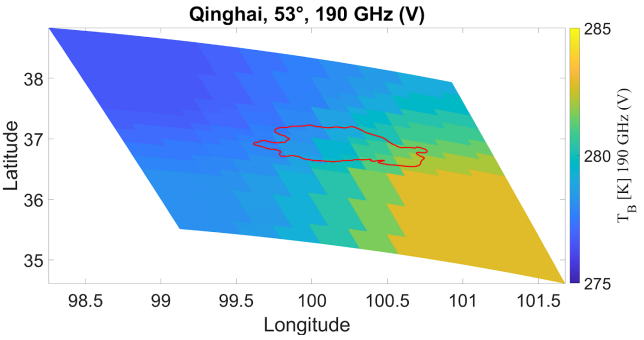
Qinghai, 53°, 190 GHz (V)
Latitude
Longitude
38
37
36
35
98.5
99
99.5
100
100.5
101
101.5
285
280
275
T_B [K] 190 GHz (V)

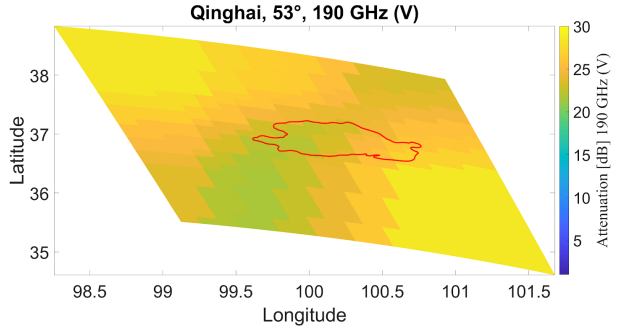
Qinghai, 53°, 190 GHz (V)
Latitude
Longitude
38
37
36
35
98.5
99
99.5
100
100.5
101
101.5
30
25
20
15
10
5
Attenuation [dB] 190 GHz (V)

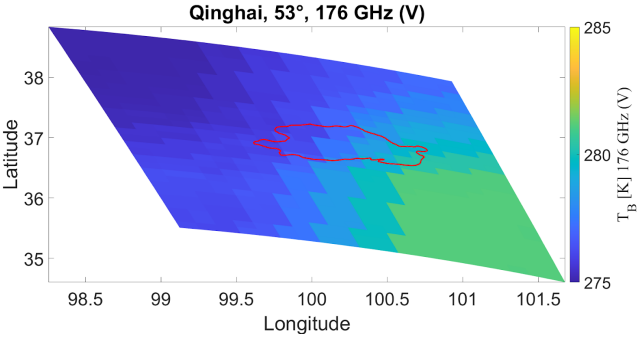
Qinghai, 53°, 176 GHz (V)
Latitude
Longitude
38
37
36
35
98.5
99
99.5
100
100.5
101
101.5
285
280
275
T_B [K] 176 GHz (V)

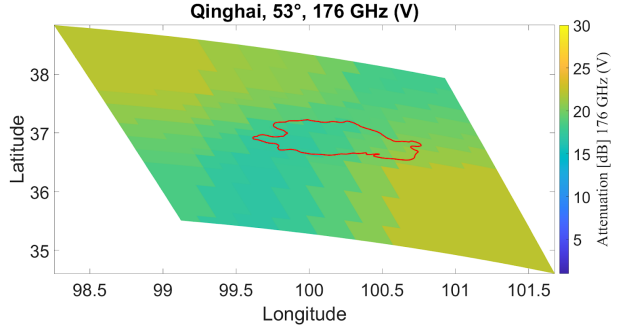
Qinghai, 53°, 176 GHz (V)
Latitude
Longitude
38
37
36
35
98.5
99
99.5
100
100.5
101
101.5
30
25
20
15
10
5
Attenuation [dB] 176 GHz (V)

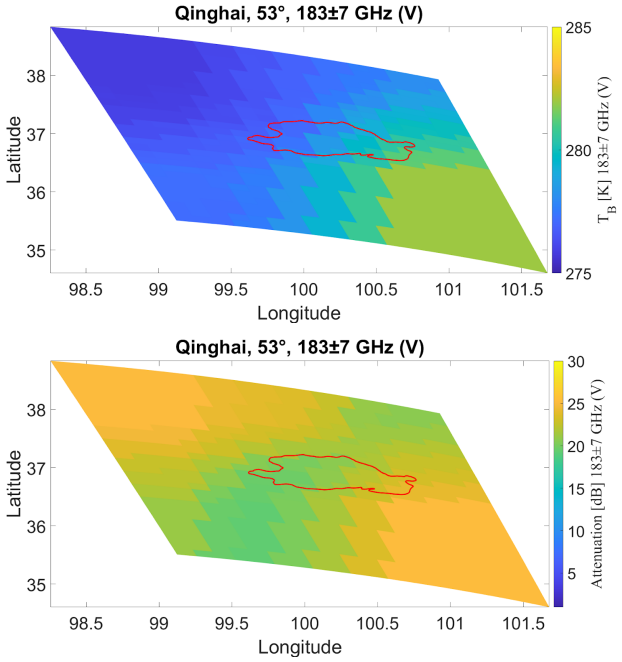

Figure 4.2.3.2: Simulated brightness temperature and attenuation along slant direction at 190 GHz (top), at 176 GHz (center) and in 183±7 GHz (bottom) in vertical polarization. The red line represents the Qinghai lake from GSHHG database at full resolution.

Fig 4.2.3.3 shows the simulation at 183±7 GHz (H) in the left and in the right there is a real image of SSMIS F17 at 183±6.6 GHz (H) (CSU_SSMIS_FCDR_V01R01_F17_D20161201_S1117_E1259_R51989).

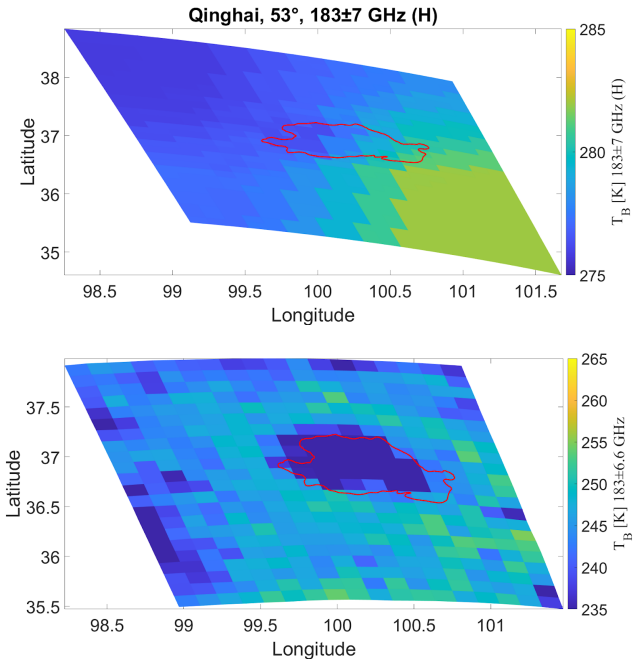

Figure 4.2.3.3: Simulated brightness temperature along slant direction at 183±7 GHz (left) in horizontal polarization and real image of SSMIS F17 at 183±6.6 GHz (H). The red line represents the Qinghai lake from GSHHG database at full resolution.

Note that both simulations at 183±7 GHz in vertical and horizontal polarization do not see the surface, differently from the real case in which SSMIS provided BT contrast for Qinghai lake.

Considering the ICI-4 channel at 243±2.5 GHz, results are reported in Fig. 4.2.3.4 both for horizontal and vertical polarizations. ICI-4 has both V than H polarization and according to Fig. 4.2.3.4 the H-polarization channel has more BT contrast over the lake as compared to the V-polarization one.

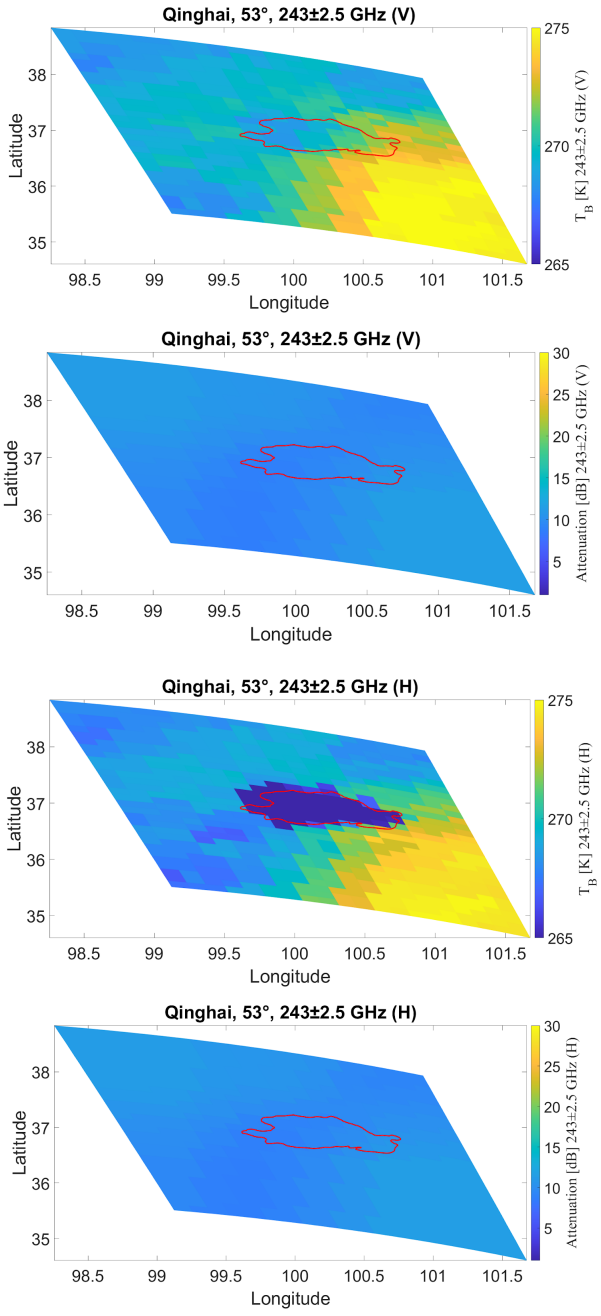

Figure 4.2.3.4: Simulated brightness temperature and attenuation along slant direction at 243.5 GHz in vertical polarization (top) and in horizontal polarization (bottom). The red line represents the Qinghai lake from GSHHG database at full resolution.

Fig. 4.2.3.4 shows that the landmark targets would be, as expected, more visible with horizontal polarization of ICI-4 channel.

4.2.4 Simulating brightness contrast and atmospheric effects

In this subsection we focus our attention on the atmospheric water vapour content and its relation with landmark targets visibility using the concept of the absolute BT contrast ΔT_B , defined as:

$$\Delta T_B(f) = |T_B(e_{s1}, f) - T_B(e_{s2}, f)| \qquad (4.2.4.1)$$

being T_B is the BT simulated at the top-of-atmosphere (TOA) and f the channel frequency, whereas e_{s1} and e_{s2} are the surface emissivities of the contiguous objects (e.g., land surface, sea water, ice shelf, lake water) characterizing each geolocation targets.

The following figures show the BT contrast considering different values of surface emissivity for 183±7 GHz and 243±2.5 GHz, using radiosounding over McMurdo station from 01 June 2016 to 31 October 2016. Fig. 4.2.4.1 reports the BT contrast using a constant arbitrary surface emissivity of 0.8 and 0.5, whereas Fig 4.2.4.2 shows the BT difference using a constant arbitrary surface emissivity of 0.9 and 0.8. If the surface emissivity difference decreases, consequently the BT contrast decreases, whereas, if the integrated water vapour increases, the BT contrast decreases more at 183 GHz than at 243 GHz. Setting a fixed value of surface emissivity at 243±2.5 GHz, we can obtain higher values of BT contrast with respect to the 183±7 GHz one so that we can expect a better landmark BT contrast for ICI-4.

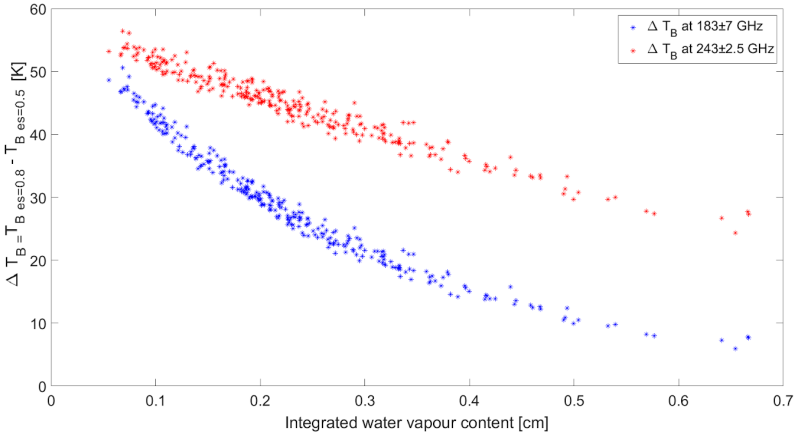

Figure 4.2.4.1: Simulated brightness temperature contrast considering landmark target with surface emissivity of 0.8 and 0.5, considering radiosounding over McMurdo station from 01 June 2016 to 31 October 2016. Red markers represent the 245±2.5 GHz and blue points are the simulation at 183±7 GHz.

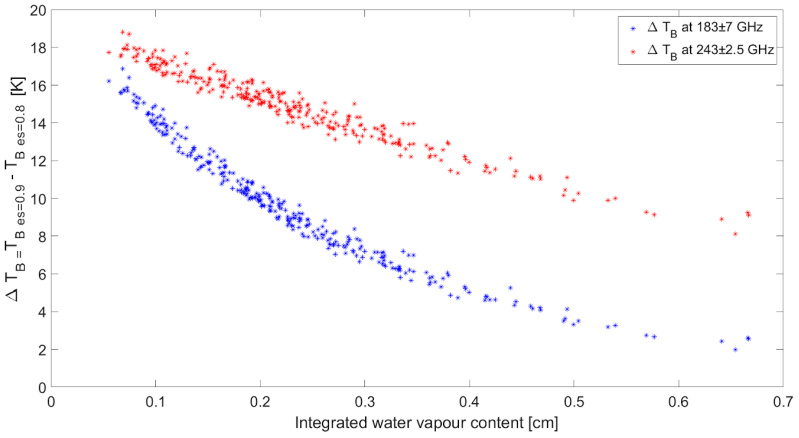

Figure 4.2.4.2: Simulated brightness temperature contrast considering landmark target with surface emissivity of 0.9 and 0.8, considering radiosounding over McMurdo station from 01 June 2016 to 31 October 2016. Red markers represent the 245±2.5 GHz and blue points are the simulation at 183±7 GHz

To simulate the behavior of the expected ICI BT contrast, we can similarly plot $\Delta T_B(f)$ using the other ICI frequencies (see Tab. 1.1), as shown in Fig. 4.2.4.3 and Fig. 4.2.4.4. Note that we have also added the results at 150 GHz for comparison as this central frequency is available for SSMIS.

As expected, the BT contrast decreases as the frequency increases up to values of less than 5 K at 664 GHz, whereas ΔT_B is larger at 150 GHz with respect to 183.3±7 GHz one which in turn is smaller than 243.2±2.5 GHz one. This means that ICI-4 exhibits an appealing potential for geolocation assessment. By reducing the surface emissivity contrast from 0.2 down to 0.05 (see Fig. 4.2.4.3 versus 4.2.4.4 and Fig. 4.2.4.5), the BT contrast is reduced if the atmosphere is unchanged.

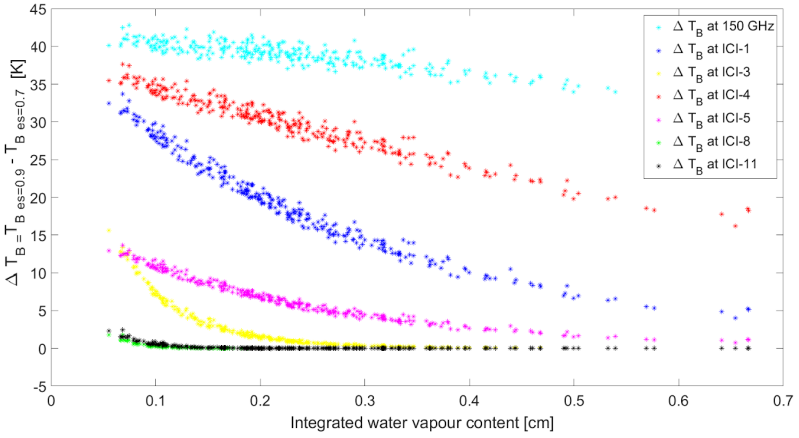

Figure 4.2.4.3: Simulated brightness temperature contrast considering landmark target with surface emissivity of 0.9 and 0.7, considering radiosounding over McMurdo station from 01 June 2016 to 31 October 2016 at several ICI frequencies and 150 GHz.

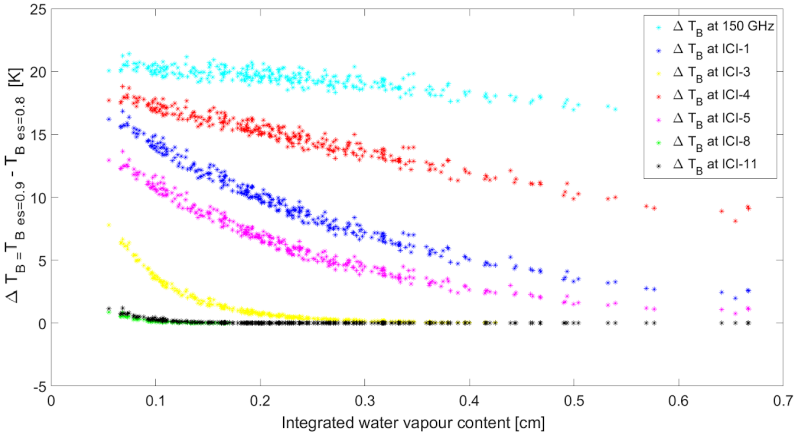

Figure 4.2.4.4: Simulated brightness temperature contrast considering landmark target with surface emissivity of 0.9 and 0.8, considering radiosounding over McMurdo station from 01 June 2016 to 31 October 2016 at several ICI frequencies and 150 GHz.

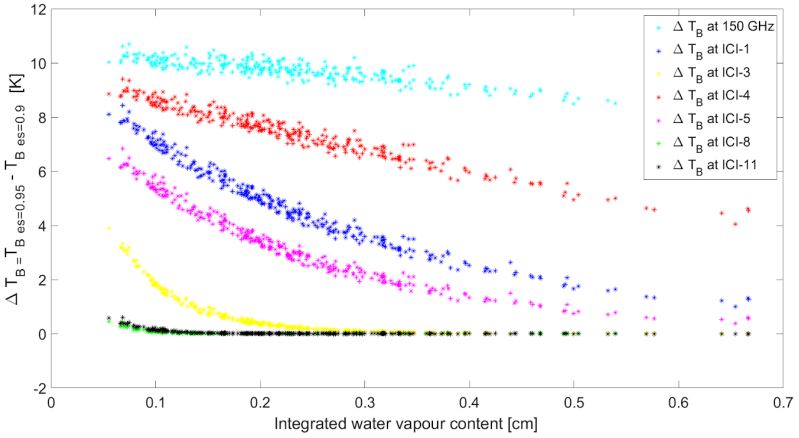

Figure 4.2.4.5: Simulated brightness temperature contrast considering landmark target with surface emissivity of 0.95 and 0.9, considering radiosounding over McMurdo station from 01 June 2016 to 31 October 2016 at several ICI frequencies and 150 GHz.

In order to simulate more realistic values of BT contrast between water and land, instead of assuming them arbitrarily constant, we can compute the surface emissivity with the TELSEM2 and TESSEM2 numerical models over the Qinghai lake, obtaining the mean values of surface emissivities, shown in Table 3. Note that TELSEM2 provides a constant value of land surface emissivity above 89 GHz, and ICI-1, ICI-5 and ICI-8 channels will have only vertical polarization.

Table 4.2.4.1: Surface emissivity for water and lake averaged over Qinghai lake provided by TELSEM2 and TESSEM2 for several frequencies

ICI channels	Frequency [GHz]	Land (H)	Sea water (H)	Land (V)	Sea water (V)
ICI-1	183±7	*No channel available*		0.93	0.87
ICI-4	243±2.5	0.89	0.57	0.93	0.90
ICI-5	325±9.5	*No channel available*		0,93	0.93
ICI-8	448±7.2	*No channel available*		0.93	0.95
ICI-11	664±4.2	0.89	0.68	0.93	0.96

The atmospheric conditions in the Qinghai lake region have been extracted from the RAOB station n. 44373, highlighted in Fig. 4.2.4.6. This station is the closest to the Qinghai lake target area and the most similar in terms of annual climatology.

Figure 4.2.4.6: RAOB station n. 44373 (red circle), available from Wyoming University over Southeast Asia. The blue spot is the region of Qinghai lake.

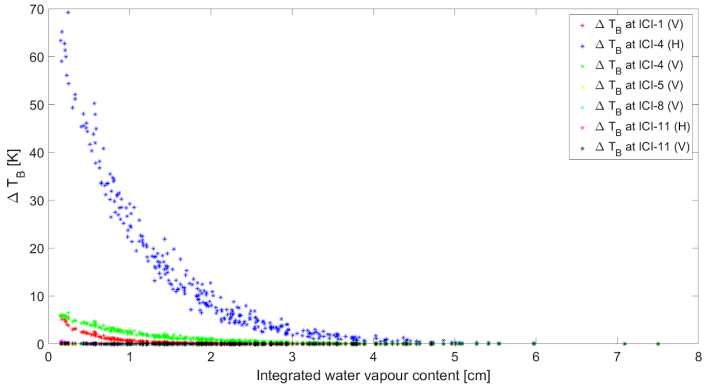

Figure 4.2.4.7: Simulated brightness temperature contrast considering landmark target with surface emissivity from TELSEM2 and TESSEM2, considering radiosounding over 44373 (Asia) station from 01 June 2016 to 31 October 2016 at several ICI channels.

Fig. 4.2.4.7 confirms what previously discussed and, in particular that, in case of targets with water/land coastline (e.g., Qinghai lake), we can expect a higher value of BT contrast using ICI-4 at horizontal polarization than using ICI-1.

Water vapour content depends on climate conditions and seasons. Following the Köppen geo-climatic classification, there are 5 main groups of climate regions, as shown in Fig. 4.2.4.8 [31]:

- A (tropical)
- B (dry)
- C (temperate)
- D (continental)
- E (polar)

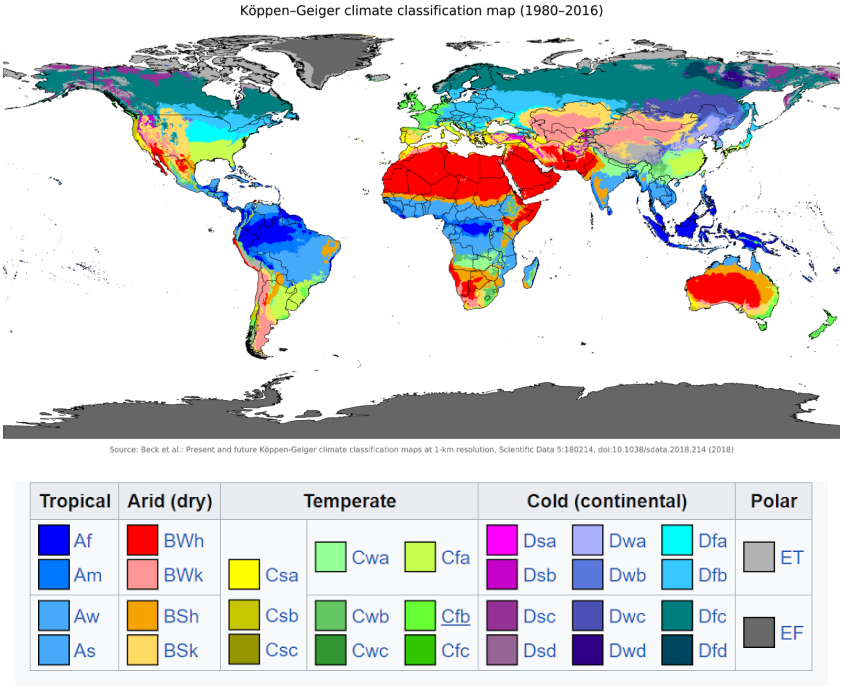

Figure 4.2.4.8: Köppen-Geiger climate classification map [30]

Selecting a RAOB station for each Köppen climate region, we can characterize the BT contrast against the integrated water vapour content using RAOB data of year 2016 (the same year of SSMIS satellite data). Tab. 4.2.4.2 shows the chosen RAOB stations from the University of Wyoming database with the corresponding number of available samples.

Table 4.2.4.2: RAOB stations for the five climate regions following Köppen climate classification

Climate region (Köppen classification**)**	**RAOB station code**	**Region** (Wyoming website)	**RAOB station latitude**	**RAOB station longitude**	**Number of atmospheric radiosounding**
A (tropical)	82917	*South America*	-10.00	-67.80	552
B (Arid-dry)	94461	*South Pacific*	-25.03	128.28	356
C (temperate)	03953	*Europe*	51.93	-10.25	728
D (Cold-continental)	30715	*Southeast Asia*	52.48	103.85	721
E (polar)	89664	*Antarctica*	-77.85	166.66	721

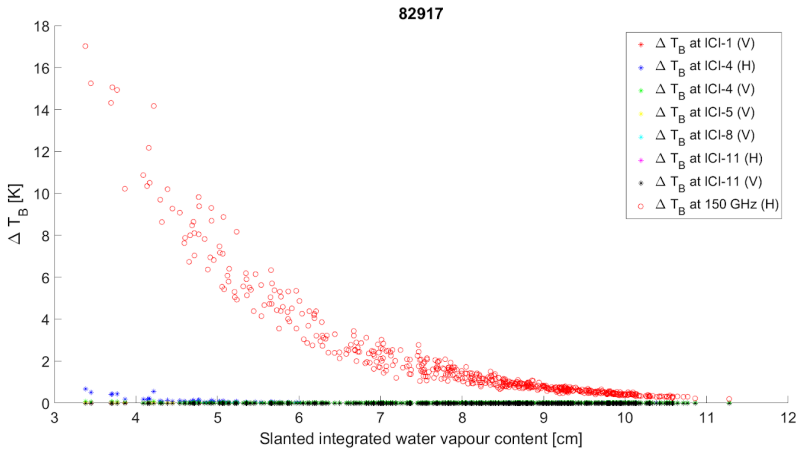

Figure 4.2.4.9: Simulated brightness temperature contrast considering landmark target with surface emissivity from TELSEM2 and TESSEM2, considering radiosounding over 82917 station (tropical) in 2016 at several ICI channels and 150 GHz H.

Fig. 4.2.4.9 shows BT contrast for a station in a tropical region, where integrated water vapour content is greater than 3 cm and we have very low BT contrast between land and water surfaces. This high value of water vapour

content can explain why we have fewer visible days for the Titicaca lake (tropical climate) than for the Qinghai lake (arid-dry climate).
Fig. 4.2.4.10 shows BT contrast for a RAOB station in arid-dry region, Fig. 4.2.4.11 shows the BT contrast for a RAOB station in a temperate region and Fig. 4.2.4.12 shows the BT contrast for a RAOB station in cold-continental region. Fig. 4.2.4.13 shows that lower values of integrated water vapour content involve an almost constant trend of $\Delta T_B\,(f)$ for window-frequency BTs (ICI-4 H), highlighted by blue markers and 150 GHz H (indicated by red points). Fig. 4.2.4.14 confirms this behavior, showing also ΔT_B at 89 GHz.

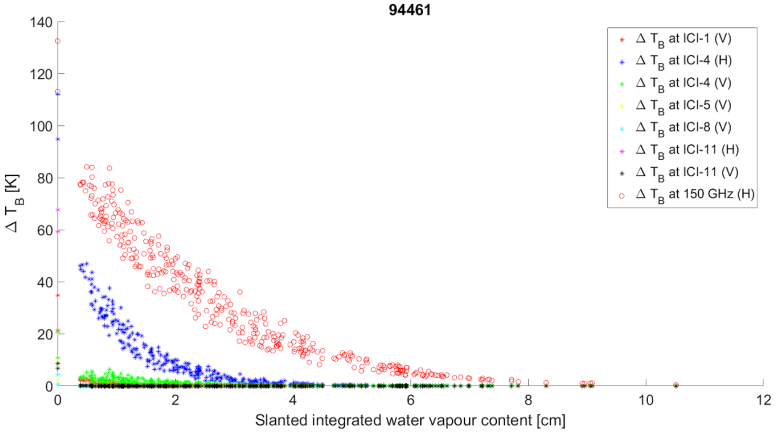

Figure 4.2.4.10: Simulated brightness temperature contrast considering landmark target with surface emissivity from TELSEM2 and TESSEM2, considering radiosounding over 94461 station (Arid-dry) in 2016 at several ICI channels and 150 GHz H.

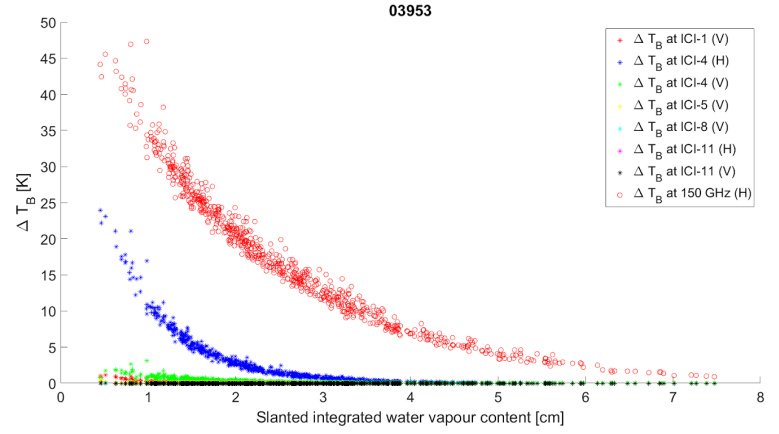

Figure 4.2.4.11: Simulated brightness temperature contrast considering landmark target with surface emissivity from TELSEM2 and TESSEM2, considering radiosounding over 03953 station (temperate) in 2016 at several ICI channels and 150 GHz H.

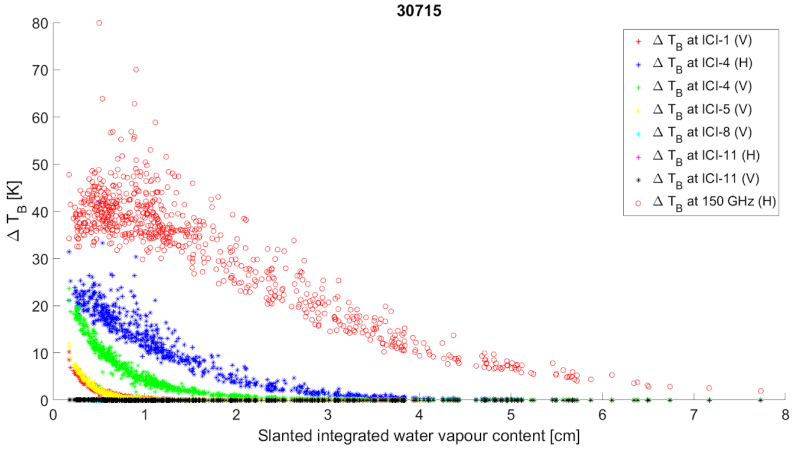

Figure 4.2.4.12: Simulated brightness temperature contrast considering landmark target with surface emissivity from TELSEM2 and TESSEM2, considering radiosounding over 30715 station (Cold-continental) in 2016 at several ICI channels and 150 GHz H.

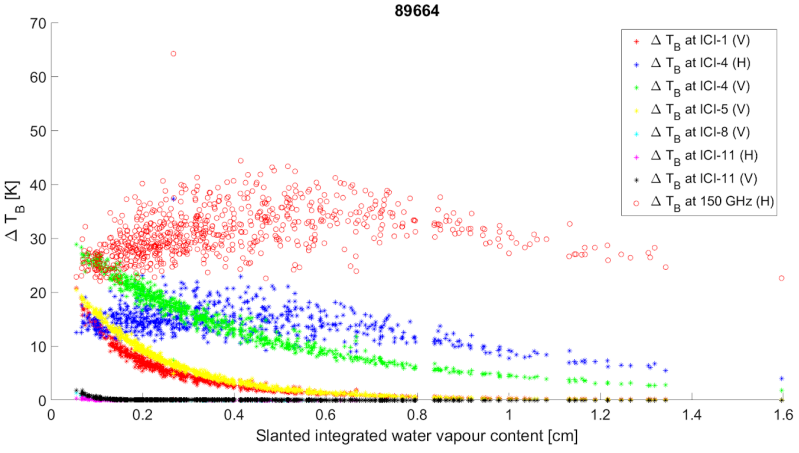

Figure 4.2.4.13: Simulated brightness temperature contrast considering landmark target with surface emissivity from TELSEM2 and TESSEM2, considering radiosounding over 89664 station (polar) in 2016 at several ICI channels and 150 GHz H.

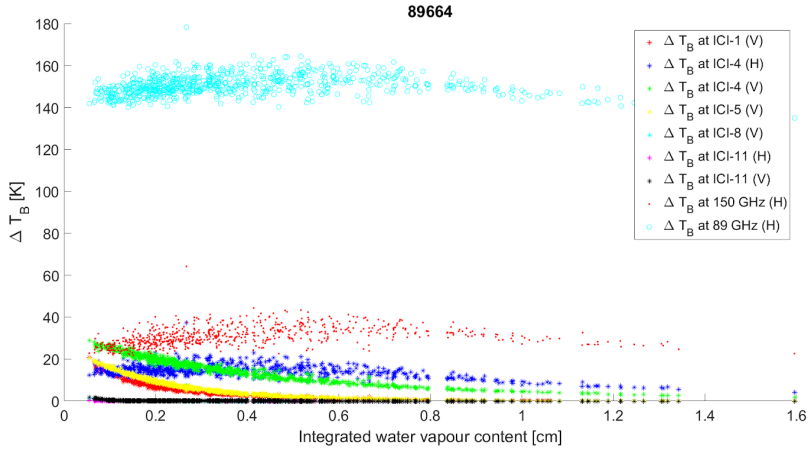

Figure 4.2.4.14: Simulated brightness temperature contrast considering landmark target with surface emissivity from TELSEM2 and TESSEM2, considering radiosounding over 89664 station (polar) on 2016 at several ICI channels, 150 GHz H and 89 GHz.

In all the previous simulations we substantially observe higher values of BT contrast for 150 GHz H and consequently for 243±2.5 GHz BT at horizontal polarization, confirming that we can better detect a surface target using ICI-4 H than 183-GHz channel. Note that, in general, we have obtained a sufficient BT contrast to extract a contour (i.e., more than 10 K) for an integrated water vapour content lower than about 1 cm.

Finally, Fig. 4.2.4.14 shows the BT simulation over a polar region, using McMurdo RAOB station, in 2016 where the water vapour content is much lower than that of the other considered regions. Looking at the BT contrast for several ICI channels, this figure confirms that in polar regions it is more probable to "see" the surface at millimeter waves and that Antarctic ice shelves are very good surface targets.

4.2.5 Geolocation accuracy test using 150 GHz

From subsection 4.2.4 we have observed that the future ICI-4 (H) BT will probably be more similar to 150 GHz H than to 183 GHz H one. To further investigate this issue, in this section we will describe some tests over the Qinghai lake in 2016.

Table 4.2.5.1: Results for geolocation evaluation accuracy using Qinghai lake as target at 150 GHz H and 183 ± 6.6 GHz H considering 84 images on 2016 from SSMIS F17

Frequency [GHz]	**Geolocation accuracy average** [km]	**Geolocation accuracy standard deviation** [km]
150 (H)	6.25	2.39
183±6.6 (H)	5.86	2.59

Considering the same dataset described in subsection 4.2.2, we have 84 samples for SSMIS F17 150 GHz H. After applying the TCM technique, the geolocation accuracy average is 6.25 km with a standard deviation of 2.39 km. Tab. 4.2.5.1 summarizes the geolocation accuracy results for 150 GHz and for 183 ± 6.6 GHz.

Tab. 4.2.5.1 shows very similar results for both frequencies, but the advantage of 150 GHz is to increase the dataset, having more visible days. We have considered all 629 images that contain the lake and, applying the fuzzy-logic approach, we have obtained 265 samples with useful BT contrast around the lake coastline to extract a contour., thus showing that 150 GHz has more surface visibility. Considering 265 images over the Qinghai lake, we obtain a geolocation accuracy average of 4.94 km with a standard deviation of 2.16 km. Using 150 GHz H we can get overall results similar to those obtained in Sect. 3.4.

Fig 4.2.5.1 shows the geolocation error accuracy and its standard deviation against the number of available SSMIS samples, considering 265 cloud-masked images at 150 GHz using the Qinghai lake target.

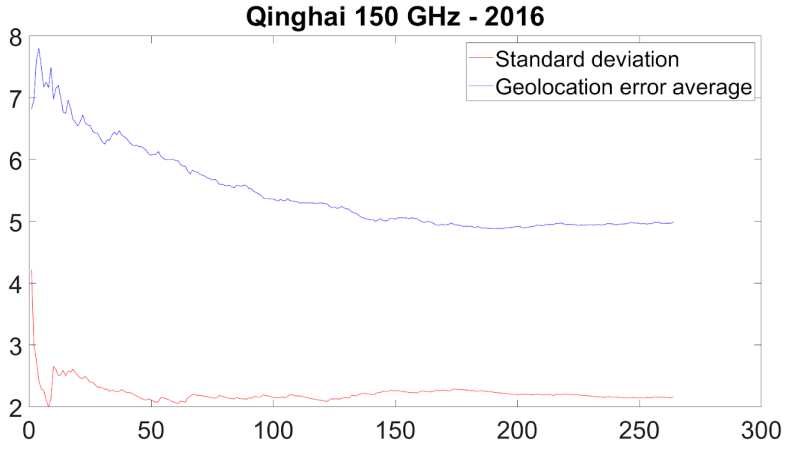

Figure 4.2.5.1: Geolocation error average (blue line) and standard deviation (red line) for Qinghai lake using SSMIS F17 at 150 GHz (H).

Fig. 4.2.5.1 shows that the geolocation error average reaches 5 km with about 140 samples. In this case, to obtain a stable value of its standard deviation, about 50 samples are sufficient. These numbers are smaller by about 30% than those shown in Fig. 4.2.5.1 for the 183-GHz channel, mainly due to different frequency vicinity to the absorption peak.

4.2.6 Frequency scaling of 243 GHz

In this section we propose a technique to simulate the 243 GHz (H) starting from existing measurements from SSMIS F17. The idea is to use an artificial neural network (ANN) to reconstruct the 243 GHz (H) using the following 5 inputs:

- BT at 150 GHz (H)
- BT at 183±6.6 GHz (H)
- transmittance at 243 GHz
- latitude
- longitude

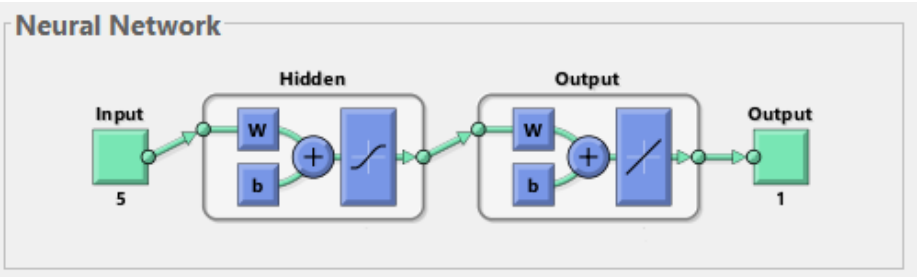

Figure 4.2.6.1: Used Artificial Neural Network (ANN)

Figure 4.2.6.1 shows the used ANN, in particular it has 1 hidden layer with sigmoid activation function. To train the ANN it is necessary to have some information regarding the 243 GHz. To obtain this information we use 1D model to simulate the brightness temperature at this frequency using ERA-5 data to provide atmospheric variables. To improve the simulation and to overcome the approximation error of the models used to calculate the surface emissivity, we propose to calculate the surface emissivity using the radiative transfer equation. In particular, the Eq. 4.2.6.1:

$$B_{sat} = B_s\, e_s\, t + B_{up} + B_{dw}(1 - e_s)\, t + B_{bg}\, t\, (1 - e_s)\, t \qquad (4.2.6.1)$$

where B_{sat} is the satellite brightness, B_s is the surface brightness, e_s is the surface emissivity and t is the transmittance. B_{up} is the atmospheric upwelling, B_{dw} is the atmospheric downwelling and B_{bg} represents the background contribution. From Eq. 4.2.6.1 it is possible to calculate the surface emissivity e_s, obtaining the following Eq. 4.2.6.2:

$$e_s = (B_{sat} - B_{up} + B_{dw}\, t + B_{bg}\, t^2)/(B_s\, t - B_{dw}\, t - B_{bg}\, t^2) \qquad (4.2.6.2)$$

Fig. 4.2.6.2 shows the obtained surface emissivity at 150 GHz, in the left, with the TB from SSMIS F17 at 150 GHz on
03/12/2016.

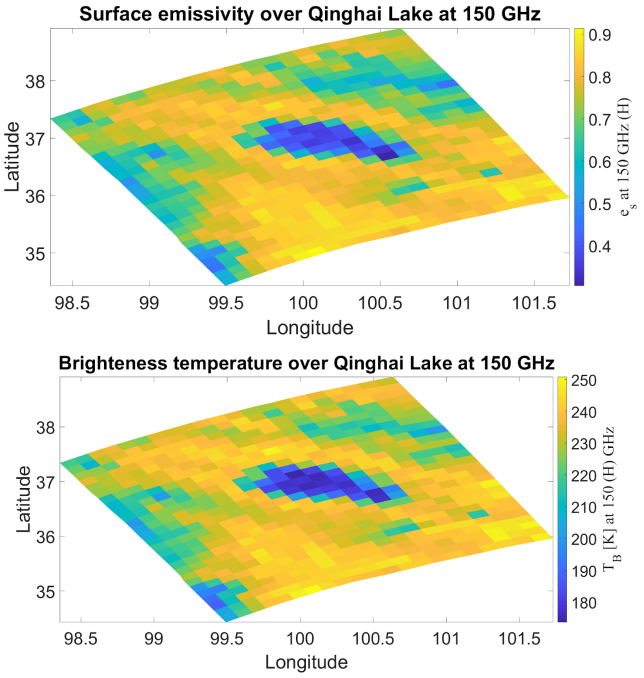

Figure 4.2.6.2: Retrieved surface emissivity using Eq. 4.2.6.2 and simulated brightness temperature on 03 December, 2016

The lake has lower surface emissivity with respect to land, as expected. To obtain the surface emissivity at 243 GHz it is possible to use TESSEM2 to find a relation between it and the surface emissivity at 150 GHz for water pixels. Fig. 4.2.6.3 shows the relationship evaluated ranging the surface temperature between 223 K and 323 K and wind from 0 m/s to 50 m/s.

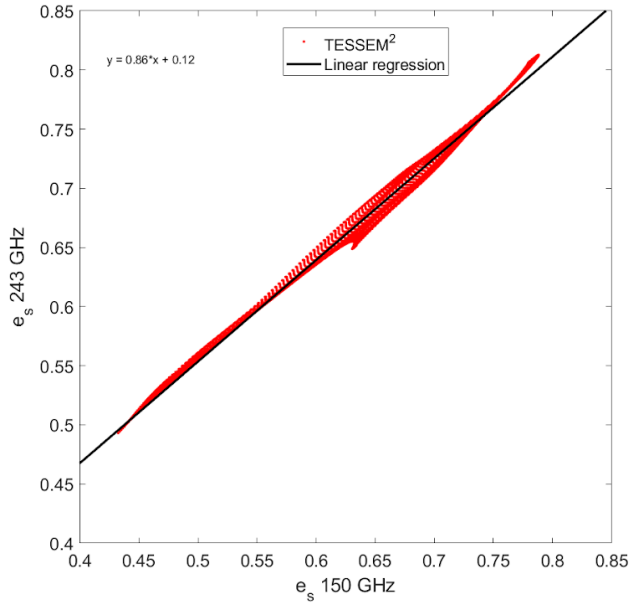

Figure 4.2.6.3: Relation between surface emissivity at 183 GHz and at 243 GHz using TESSEM²

Interpolating data with linear regression it is possible to obtain the Eq. 4.2.6.3 to obtain surface emissivity at 243 GHz for water pixels:

$$e_{S_{243GHz}} = 0.86\, e_{S_{150GHz}} + 0.12 \qquad (4.2.6.3)$$

Associating a land sea mask for each image it is possible to scale the surface emissivity at 243 GHz. For land pixels we suppose to have constant values from 183 GHz to 243 GHz, as obtained by TELSEM2, see Table 4.2.4.1. Final emissivities can be used to simulate 243 GHz in horizontal polarization to obtain reference images to train and test the ANN.

To train the ANN we used 8 images with a total of 3800 pixels and we test it using 2 different images. Fig. 4.2.6.4 shows the results obtained comparing the results for 243 GHz from ANN e 243 GHz provided by radiative transfer simulation, using 1D model. The ANN well reconstruct the image in both cases, in particular the correlation between scaled and simulated BT are 0.975 for 12 December, 2016 and 0.991 for 23 December, 2016.

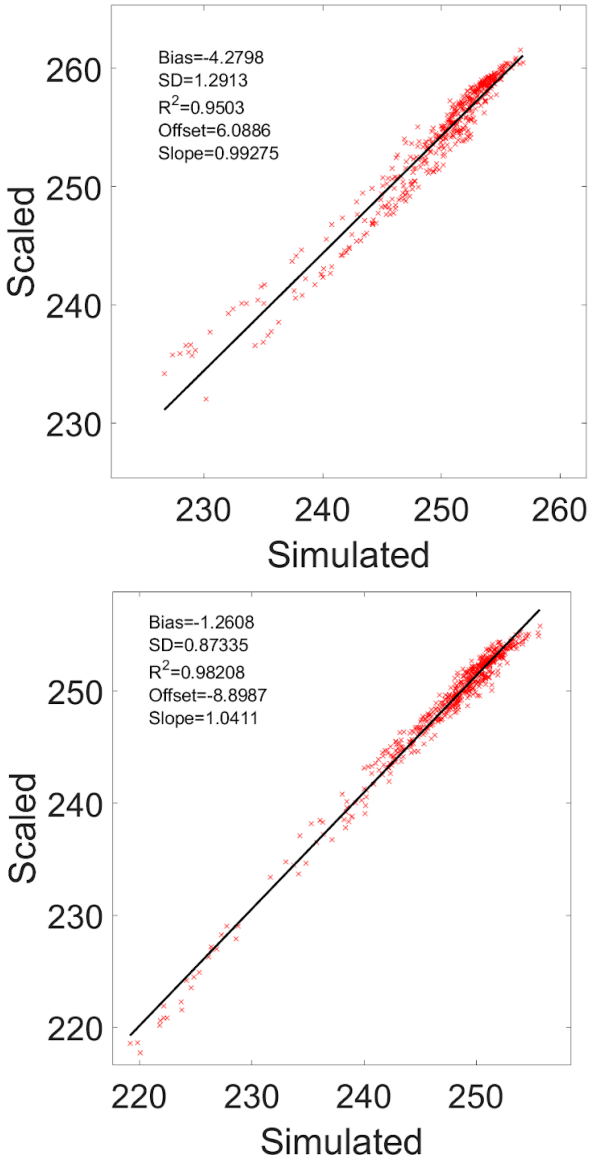

Figure 4.2.6.4: Results for ANN at 243 GHz

To better investigate the ANN, Fig. 4.2.6.5 reports the results obtained with the same two days reconstructing the 186±6.6 GHz. To scale this frequency we used as input the BT at 150 GHz (H), BT at 183±1 GHz (H), transmittance at 186±6.6 GHz, latitude and longitude. The correlation is 0.856 for 12 December, 2016 and 0.889 for 23 December, 2016.

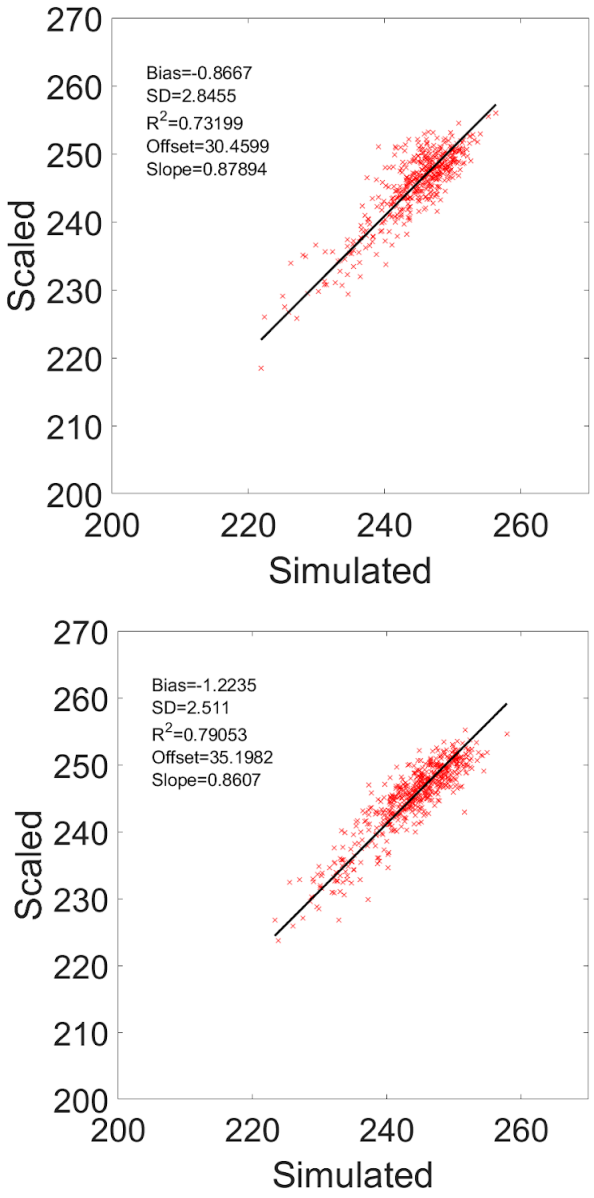

Figure 4.2.6.5: Results for ANN at 183 GHz

Qinghai lake is more visible from October to November. In particular, using the 183±6.6 GHz (H) from SSMIS, Qinghai lake was visible 43 times during this period in 2016. Table 4.2.6.1 shows the results obtained with the above 43 samples using the following three sources;

- 183±6.6 GHz (H) from SSMIS,
- 183±6.6 GHz (H) reconstructed from SSMIS data at 150 GHz and at 183±1GHz (H)
- 243.2±2.5 GHz (H) reconstructed from SSMIS data at 150 GHz and at 183±6.6 GHz (H)

Table 4.2.6.1: Results for geolocation evaluation accuracy using Qinghai lake from October to December in 2016 (43 samples)

Source	**Geolocation accuracy average** [km]	**Geolocation accuracy standard deviation** [km]
183±6.6 GHz (H) SSMIS	5.64	2.54
183±6.6 GHz (H) ANN	5.87	3.06
243.2±2.5 GHz (H) ANN	5.79	2.66

Table 4.2.6.1 shows very similar results in all three cases, demonstrating that the ANN well reconstructs the images and their geolocation error. However the scope of the ANN is to demonstrate that ICI-4 is the best candidate for geolocation assessment for the future ICI. Analyzing the entire 2016, Qinghai lake is visible 181 times obtaining an average value of 5.56 km and a standard deviation of 2.23 km. The dataset for 243.2±2.5 GHz (H) is bigger with respect to the 84 images obtained from 183±6.6 GHz (H) from SSMIS. This increase of number of samples is the consequence to the decrease of attenuation between 243 GHz and 183 GHz and confirms that ICI-4 will provide more targets than ICI-1.

CHAPTER 5

5. CONCLUSION

The goal of this work has been to propose a systematic methodology for geolocation error assessment, including the criteria regarding the search of landmark targets and the cloud-masking defuzzification step to filter the available dataset from cloud coverage contamination. The 6 appendixes discuss the details about the technical analysis of major target classes, such as high-latitude lakes, mountain ranges and ice shelves, as well as some details of the developed algorithms.

Table 5.1: Summary of geolocation error accuracy results in terms of average and standard deviation for all selected targets during 2016 using SSMIS F17 at 183±6.6 GHz at horizontal polarization. Sample yearly number and notes about target features are also reported.

Target	Geolocation accuracy mean value [km]	Geolocation accuracy standard deviation [km]	Cloud-masked yearly sample number (percentage)	Notes
Northern hemisphere (NH)				
Qinghai lake	5.86	2.59	84 (13.4%)	All shift directions are sampled due to the close contour.
Karakorum mountains	5.62	2.60	51 (7.2%)	DEM resolution may impact the results. Useful oblique pattern.
Hudson Bay	6.29	2.89	62 (13.6%)	All shift directions are sampled due to the U contour.
Nares strait	4.74	2.02	688 (26.2%)	Slightly scattered contour with oblique pattern.
NH average value	*5.2 km*	*2.3 km*		

Southern hemisphere (SH)				
Ross ice shelf	4.17	2.16	599 (25.7%)	Sharp high-resolution contour, but mainly horizontal pattern.
Filchner-Ronne ice shelf	5.75	2.35	387 (16.4%)	Sharp high-resolution contour with a V contour
Amery ice shelf	6.25	1.55	153 (12.3 %)	Sharp high-resolution contour with a nearly-vertical contour
Titicaca lake	6.53	2.82	41 (7.7%)	All shift directions are sampled due to the close contour.
Andean mountains	5.32	3.06	125 (22.5%)	DEM resolution may impact the results. Useful oblique pattern.
SH average value	*5.6 km*	*2.4 km*		

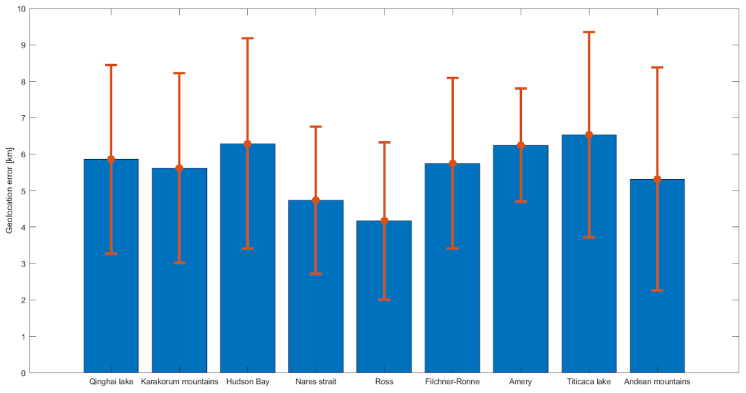

Figure 5.1: Summary of geolocation error accuracy results in term of average and standard deviation for all selected targets during 2016 using SSMIS F17 at 183±6.6 GHz at horizontal polarization.

A total number of 9 landmark targets has been selected covering both the northern and southern hemisphere in order to guarantee good temporal coverage during the driest seasons. For each target results have been provided in terms of mean value and standard deviation of the geolocation error both in the northern hemisphere and southern hemisphere.

This work demonstrates that SAR images can be used as reference to validate the geolocation error thanks to their global coverage with high spatial resolution. In addition, using SAR data it is also possible to monitor any ice coastline variations, contrary to the usage of shoreline database.

The problem of the sensitivity analysis of the TCM geolocation error assessment methodology to the most critical free parameters has been discussed as a proxy to the error budget estimate. The latter, as a matter of fact, is not easily defined for the lack of an absolute reference (we are here estimating not the geolocation error, but its accuracy or the uncertainty of the geolocation error correction procedures). The conclusion is that the interpolation-grid spatial resolution provides a parametric variability of about 0.6 km. Moreover, from the sensitivity analysis to the cloud-masked sample size, we can conclude that about 50-75 images are sufficient to assess the geolocation error statistics for all landmark targets.

The Table 5.1 and Fig. 5.1 report a summary of the geolocation accuracy validation for all targets using SSMIS F17 at 183±6.6 GHz at horizontal polarization [32] [33]. The average value of about 5.4 km with a standard deviation of about 2.3 km can be interpreted as the mean geolocation error of SSMIS selected imagery. These numbers are comparable with the values given in Poe et al. [10] and Kunkee et al. [30] for SSMIS F16 (different from F17 we have used in this work) even though they mention the estimate of 4-5 km [13] and less than 6 km [30]. Note that Poe et al. [10] refer to their estimate as 1-sigma error value, whereas Kunkee et al. [30] stress the fairly good stability of their retrieved error.

The analysis, carried out using SSMIS channel at 183±7 GHz, has been extended to ICI channels at 183 GHz and 243 GHz through a simulation-based frequency scaling. The approach has involved the analysis of SSMIS imagery at 150 GHz and 183±7 GHz as well as the radiative transfer simulation of satellite brightness temperatures and slant-path attenuation from both available radiosounding profiles and ERA5 reanalysis atmospheric profiles near the selected targets. Note that SSMIS 183±7 GHz channel is at H polarization, whereas the foreseen ICI 183±6.6 GHz one is at V polarization meaning that we

expect a slightly reduced BT contrast for ICI with respect to SSMIS one (due to the larger V-polarized surface emissivity), as described in Chapter 4.

The second scope of this work is to investigate the future ICI channels, studying their dependence on integrated water vapour. As expected, ICI-4 in horizontal polarization is the least sensitive channel to water vapor and at 243.2±2.5 GHz the atmosphere is less opaque with, consequently, more probability to see surface targets. The proposed artificial neural network aims to simulate this frequency starting from existing images. The results in Table 4.2.6.1 confirm that ANN provides stable results for the different simulations. Indeed, we also obtain the same results for 183±6.6 GHz (H) as output of proposed ANN, considering the real data provided by SSMIS F17. Finally, the ANN confirms that during a full year the Qinghai Lake is visible more times at 243.2±2.5 GHz with respect to 183±6.6 GHz (H), obtaining an average value of 5.56 km with a standard deviation of 2.23 km. Therefore, we can say that ICI-4 could see more surface targets with respect to other ICI channels and it will be the best candidate to validate the geolocation for ICI radiometer. In particular, the geolocation of all other channels will be validated in a relative way with respect to ICI-4.

APPENDICES

APPENDIX A. TCM approach for high-altitude lake targets

The inputs to validate the geolocation using a lake are the images of SSMIS F17 at 183 ± 6.6 GHz (horizontal polarization) along the whole 2016 year. Initially it is necessary to extract only the spaceborne radiometric images containing the high-altitude lake.

Unfortunately, not all images can be useful for our purpose due to possible atmospheric opacity in presence of clouds and precipitation. In order to apply the fuzzy-logic cloud masking to high-altitude lakes, referring to subsection 3.3, for $M_2(\Delta T_{Bm})$ we use the following equation:

$$\begin{aligned} M_2(\Delta T_{Bm}) &= 1 && \text{if } \Delta T_{Bm} \geq 8K \\ M_2(\Delta T_{Bm}) &= \Delta T_{Bm}/8 && \text{if } \Delta T_{Bm} < 8K \end{aligned} \tag{A.1}$$

where ΔT_{Bm} is the mean BT contract around the target.

To evaluate the mean contrast around the lake, we can compute the BT difference along vertical and horizontal directions. For example, Fig. A.1 shows the pixels A, B, C, D and E, selected to compute the BT contrast ΔT_{Bm} for Qinghai lake, using the following equation:

$$\Delta T_{Bm} = \frac{(T_B - T_A) + (T_C - T_A) + (T_D - T_A) + (T_E - T_A)}{4} \tag{A.2}$$

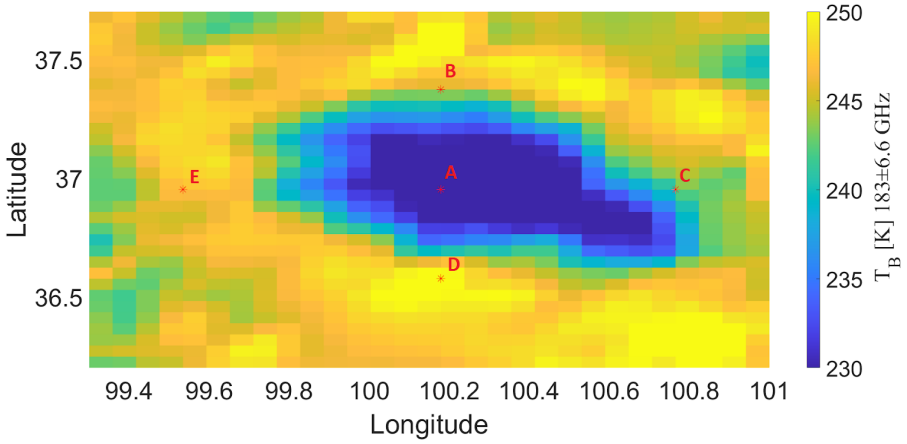

Figure A.1: Brightness temperature (BT) image at 183±6.6 GHz H over Qinghai lake from SSMIS F17 on 2016/12/01. Five points are those used to calculate the BT contrast along vertical and horizontal directions

The BT contrast is evaluated in the interpolated grid at 5 km of spatial resolution, in order to obtain the BT contrast between the same points for all images. The function $M_1(\varepsilon)$ can be calculated as:

$$\begin{aligned} M_1(\varepsilon) &= 0 && \text{if } \varepsilon \geq 15\ km \\ M_1(\varepsilon) &= -\frac{\varepsilon}{15} + 1 && \text{if } \varepsilon < 15\ km \end{aligned} \tag{A.3}$$

Computing the inference function from (A.1), the considered image is selected only if $I\left(\Delta T_{Bm}, \varepsilon\right) > 0.3$. The remaining images can be used to validate the geolocation error using the lake as target.

As mentioned in Section 3.1, before the defuzzification step, it is necessary to correct the parallax error because the lake has a high altitude. To correct this error, we must find the intersection between the line of sight of the satellite and the orography, provided by GTOPO30, that is a digital elevation model (DEM) with a resolution of 30 arcsec (approximately 1 km) To better represent the footprint, we have calculated the average of the DEM with a spatial resolution of about 13 km, as pixels dimension, and the we found the intersection between the line of sight and this average DEM , as shown in Fig. A.2. After this correction the image is shifted, depending on ascending or descending orbit and the position of the target in the satellite swath.

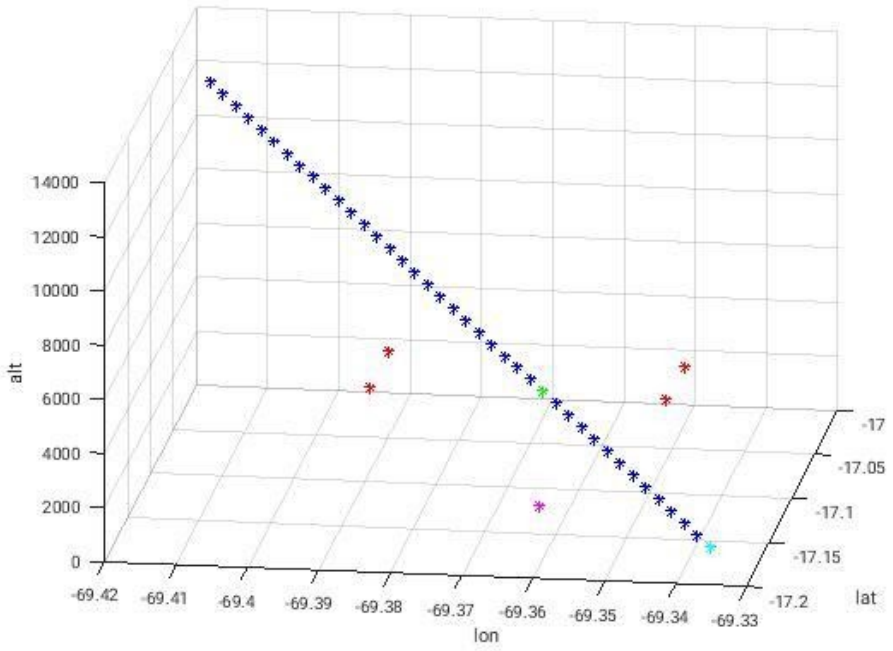

Figure A.2: Example of parallax error correction: blue markers represent the discretized satellite line of sight. The four red points are the nearest points of DEM around the intersection between DEM and line of sight. The green marker is the first point of the line of sight that has an altitude lower than DEM. The cyan point is the intersection between line of sight and earth ellipsoid (WGS84). Finally, the magenta marker represents the corrected coordinates on the surface.

To increase the BT image spatial resolution, the different samples are interpolated using cubic interpolation method in the same evenly spaced grid with 5km of spatial resolution, shown in Fig. A.3.

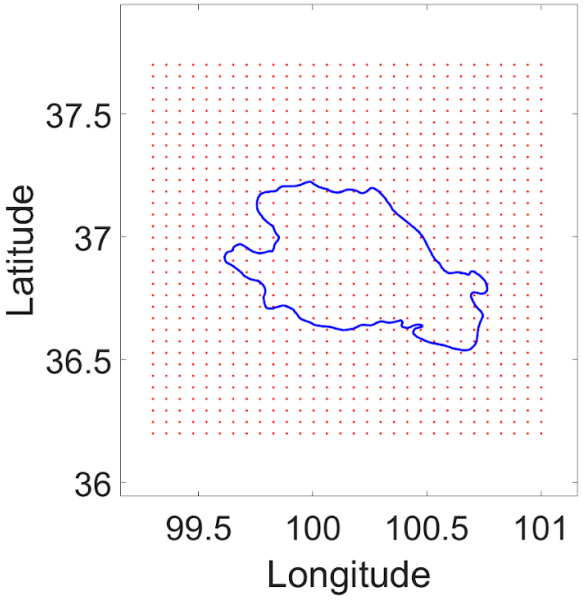

Figure A.3: Grid used to interpolate the BT data for Qinghai lake. The blue line represents the contour of Qinghai lake provided by GSHHG database.

After the interpolation step, it is possible to extract the contour and for Qinghai lake we adopt a Canny algorithm to obtain the contour line, as shown in Fig. A.4

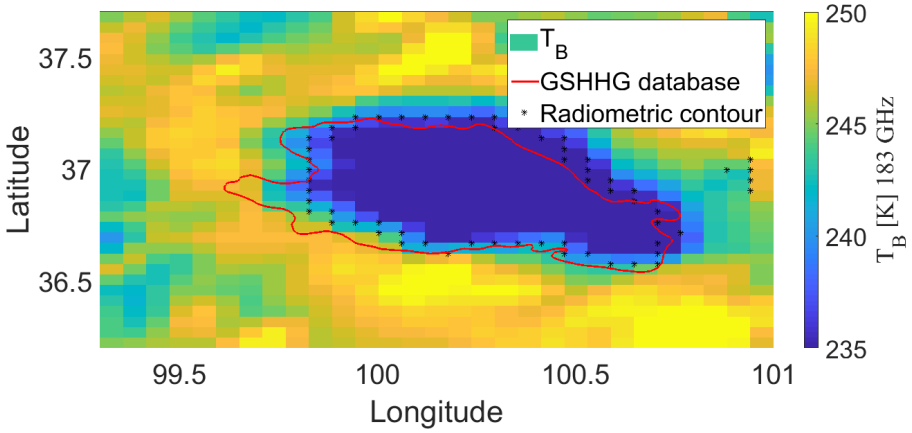

Figure A.4: Brightness temperature (BT) image at 183±7 GHz H over Qinghai lake from SSMIS F17 on 2016/12/01. The red line represents the lake coastlines from GSHHG database, described in Wessel and Smith (1996). Black markers indicate the extracted contour by Canny method.

To correlate the reference line with the satellite radiometric contour, we can project the GSSHG line on the same radiometric grid, using the nearest-neighbor technique, as shown in Fig. A.5:

The code is developed in Matlab environment and, summarizing all steps for this kind of target, we list:

1) Extract the box that contains target
2) Parallax error correction, as shown in Appendix E.
3) Interpolate data to fictitiously increase the spatial resolution, using *'griddata'* Matlab function
4) Apply Canny algorithm to extract radiometric contour, using '*edge'* Matlab function
5) Project GSHHG shoreline database on the same grid obtained at step 2, using nearest neighbour approach.
6) Calculate the normalized cross-correlation, using *'normxcorr2'* Matlab function
7) To reach sub-pixel accuracy, the maximum of the normalized cross-correlation is fitted by a 4th-order polynomial.
8) Take the coordinates of the maximum of fitted normalized cross-correlation.
9) Calculate the shift in pixels
10) Calculate the corresponding shift along latitude and longitude
11) Evaluate the displacement (in km) of the shift found in step 9.

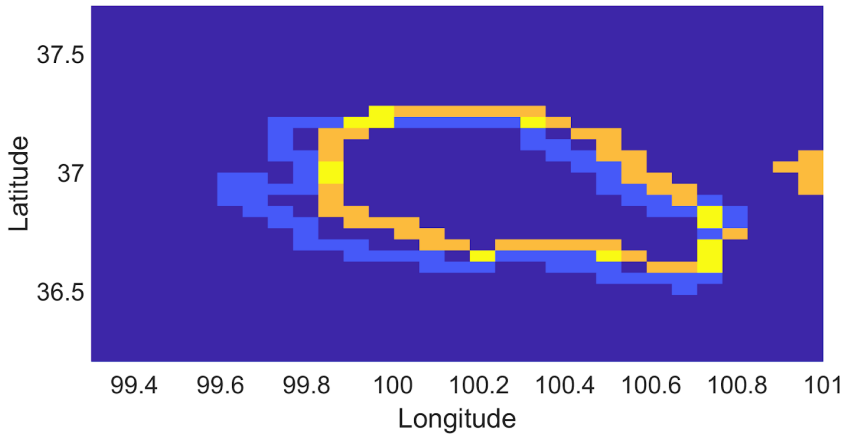

Figure A.5: The orange line is the radiometric contour; the blue line is the reference line and the yellow is the overlap of the two lines.

APPENDIX B. TCM approach for mountain-chain targets

The inputs to validate the geolocation using mountain chains are the images of SSMIS F17 at 183 ± 6.6 GHz (horizontal polarization) along the entire 2016. Initially it is necessary to extract only the images that contain the target and then it is necessary the parallax error using DEM correction. The used inference function is:

$$I\left(\Delta T_{Bm}, \varepsilon\right) = M_1(\varepsilon)\, M_2(\Delta T_{Bm}) \tag{B.1}$$

where:

- $I(x)$ = inference function
- ΔT_{Bm} = mean BT contrast around lake
- ε = geolocation error
- $M_1(\varepsilon)$ = membership function depending on the geolocation error
- $M_2\left(\Delta T_{Bm}\right)$ = membership function depending on the BT contrast

To evaluate the mean BT contrast along the mountain, we can compute the BT difference along the horizontal and vertical axis. For example, Fig. B.1 shows the selected pixels to compute the BT contrast ΔT_{Bm} for Karakorum mountains, obtained by the following equation:

$$\Delta T_{Bm} = \frac{(T_B - T_A) + (T_D - T_C) + (T_F - T_E) + (T_H - T_G)}{4} \tag{B.2}$$

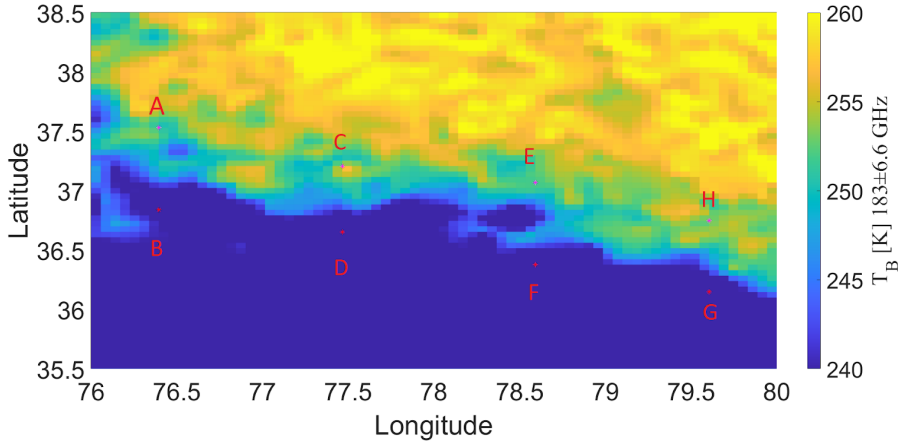

Figure B.1: Brightness temperature (BT) image at 183±6.6 GHz H over Karakorum mountains from SSMIS F17 on 2016/01/02. Eight points are those used to calculate the BT contrast along mountain chain

The BT contrast is evaluated in the interpolated grid at 5 km of spatial resolution, in order to obtain the BT contrast between the same points for all images. It is then possible to obtain the inference function and the single image is used only in case with $I(\Delta T_{Bm}, \varepsilon) > 0.3$.

After the defuzzification step, we have the complete dataset to validate the geolocation accuracy. To increase the images spatial resolution, the different samples are interpolated using cubic interpolation in the same evenly spaced grid. After the interpolation step, we have calculated the gradient of the image using Sobel filter and use a DEM as a reference.

To correlate the gradient of BT temperature with the reference, we have reprojected DEM in the same grid, applying the Sobel filter to obtain the reference gradient. Finally, it is possible to correlate the two images, obtaining the relative displacement.

The code is developed in Matlab environment and, summarizing all steps for this kind of target, we list:

1) Extract the box that contains target
2) Parallax error correction, as shown in Appendix E.
3) Interpolate data to fictitiously increase the spatial resolution, using *'griddata'* Matlab function
4) Apply Sobel filter to DEM to calculate its gradient
5) Apply Sobel filter to radiometric image to calculate its gradient
6) Calculate the fast fourier transform to both gradients, using '*fft2'* Matlab function
7) Calculate the shift in pixels between to images, using *'dftregistration'* Matlab function
8) Calculate the corresponding shift along latitude and longitude
9) Evaluate the displacement (in km) of the shift found in step 8

APPENDIX C. TCM approach for ice-shelf targets

The inputs to validate the geolocation using an ice shelf are the images of SSMIS F17 at 183 ± 6.6 GHz (horizontal polarization, H) along the entire 2016. Initially it is necessary to extract only images containing different shelves. Unfortunately, not all images can be useful for our purpose, as explained in Sec. 2.3. The proposed inference function is:

$$I\left(\Delta T_{Bm}, \varepsilon\right) = M_1(\varepsilon)\, M_2(\Delta T_{Bm}) \tag{C.1}$$

where:

- $I(x)$ = inference function
- ΔT_{Bm} = mean BT contrast around lake
- ε = geolocation error
- $M_1(\varepsilon)$ = membership function depending on the geolocation error
- $M_2\left(\Delta T_{Bm}\right)$ = membership function depending on the BT contrast

Considering that for ice shelves the BT contrast is higher with respect to other targets, like the Qinghai lake, we have increased this threshold. Therefore, for $M_1(c)$ around the lake we use the following equations:

$$\begin{aligned} M_2\left(\Delta T_{Bm}\right) &= 1 && \text{if } \Delta T_{Bm} \geq 15K \\ M_2\left(\Delta T_{Bm}\right) &= \Delta T_{Bm}/15 && \text{if } \Delta T_{Bm} < 15K \end{aligned} \tag{C.2}$$

To evaluate the contrast ΔT_{Bm} around the lake, we propose to calculate the BT contrast differently along vertical and horizontal directions. Fig. C.1 shows the point selected for calculate the BT contrast, obtained by the following equation:

$$\Delta T_{Bm} = \frac{(T_B - T_A) + (T_D - T_C) + (T_F - T_E) + (T_H - T_G)}{4} \tag{C.3}$$

$M_1(\varepsilon)$ can be calculated as:

$$\begin{aligned} M_1(\varepsilon) &= 0 && \text{if } \varepsilon \geq 15\ km \\ M_1(\varepsilon) &= -\frac{\varepsilon}{15} + 1 && \text{if } \varepsilon < 15\ km \end{aligned} \tag{C.4}$$

Finally, it is possible to obtain the inference function and the single image is used only in case with $I\left(\Delta T_{Bm}, \varepsilon\right) > 0.3$.

Ice shelves are at sea level so that it is not necessary to perform a parallax error correction using DEM. Secondly, to fictitiously increase the spatial resolution of

BT images for intercomparison purposes, data are upsampled on a regular grid through a triangulation method using a cubic interpolation. A polar stereographic map projection is used in this work. The new grid is regularly evenly spaced (about 5 km) in X-Y domain and the resulting BT, for Ross ice shelf, is shown in Figure D.2.

The limits of the box for Ross ice shelf are the following:

- Latitude = [-78.5 -76.5];
- Longitude = [170.6 178.5].

The BT contrast (Eq. C.3) is evaluated in the interpolated grid at 5 km of spatial resolution on a polar stereographic map, in order to obtain the BT contrast between the same points for all images.

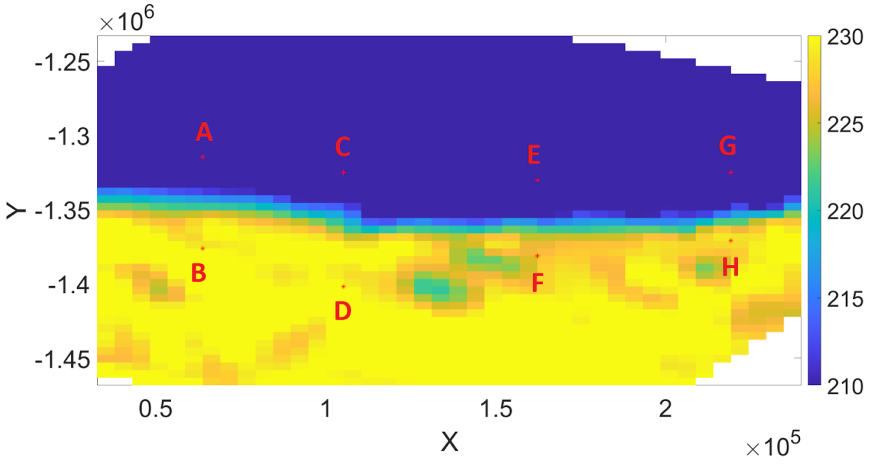

Figure C.1: Brightness temperature (BT) image at 183±6.6 GHz H over Ross ice shelf from SSMIS F17. Eight five points are those used to calculate the BT contrast along coastline

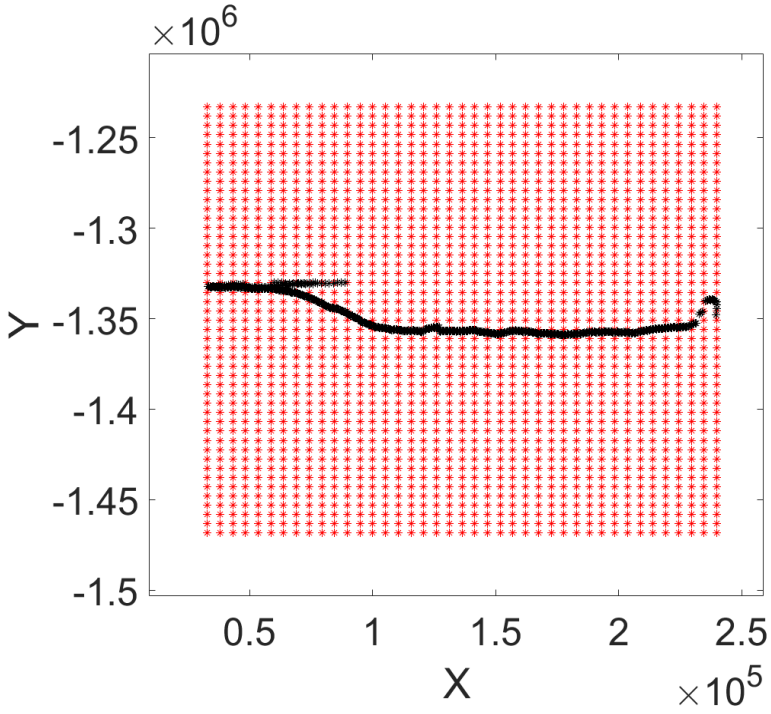

Figure C.2: Grid used to interpolate the BT data for Ross ice shelf. Black markers represent the contour of Ross extracted from the SAR image.

In the Antarctic region SAR data are available in Extra-Wide Swath Mode with a 400-km swath at 20x40 m^2 spatial resolution and it is possible to download them from the following web site: https://scihub.copernicus.eu/dhus/#/home

For example, the image in Fig. 3.6.1.3 is obtained from the data: S1A_EW_GRDM_1SSH_20160724T111725_20160724T111829_012289_0131CA_1241

This dataset contains the following fields:

- amplitude_HH
- intensity_HH
- amplitude_HV
- intensity_HV

SAR data are provided as metadata, containing also the orbit state vectors, but it is generally not accurate and can be refined with the precise orbit files which are available days-to-weeks after the generation of the product. It is necessary to apply the orbit file operator to obtain accurate satellite position and velocity

information. To do this correction and for the other necessary steps, we have adopted the SNAP toolbox, downloadable from the web site http://step.esa.int/main/download/snap-download/. For Level-1 GRD it is also necessary the thermal noise removal.

To obtain imagery in which the pixel values can be directly related to the scene radar backscatter, the calibration step has to be carried out to have sigma-nought images. At this step the resolution is very high for our purpose and it still presents a speckle noise. To reduce it, it is possible to apply a multilook operator. After these steps, it is possible to extract a contour, as shown in Fig. A.3, but to use this as reference in the validation of geolocation accuracy it is necessary a further step. This reference line must be projected in the same regular evenly spaced (about 5 km) in X-Y domain, adopting the nearest neighbour approach, as shown in the following Fig. D.3.

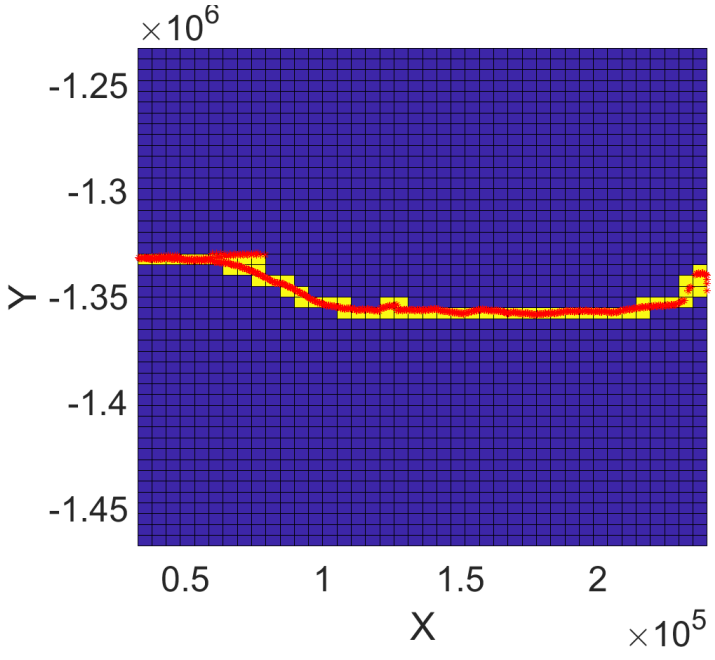

Figure D.3: The red markers indicate the contour extracted from SAR data and yellow pixels represent the reference contour in the same radiometric grid with a spatial resolution of about 5 km.

Correlating the obtained reference line with the extracted radiometric contour, it is then possible to validate the geolocation accuracy (in km).

The code is developed in Matlab environment and the steps for these targets are summarized as follows:

1) Extract the box that contains target
2) Project radiometric data on polar stereographic map, using '*polarstereo_fwd*' Matlab function
3) Interpolate data to fictitiously increase the spatial resolution, using *'griddata'* Matlab function
4) Apply Canny algorithm to extract radiometric contour, using '*edge'* Matlab function
5) Project SAR data on polar stereographic map, using '*polarstereo_fwd*' Matlab function
6) Apply Canny algorithm to extract SARcontour, using '*edge'* Matlab function
7) Project SAR contour in the same grid obtained at step 3, using nearest neighbour approach.
8) Calculate the normalized cross-correlation, using *'normxcorr2'* Matlab function
9) To reach sub-pixel accuracy, the maximum of the normalized cross-correlation is fitted by a 4th-order polynomial.
10) Take the coordinates of the maximum of normalized cross-correlation.
11) Calculate the shift in pixels
12) Calculate the corresponding shift along latitude and longitude. To reproject data on geographical coordinates (latitude-longitude) we have used the *'polarstereo_inv'* Matlab function
13) Evaluate the displacement (in km) of the shift found in step 11.

APPENDIX D. Contour extraction and cross-correlation for TCM

Using the target-contour matching algorithm, the extraction of a contour that can be carried out by applying two main methods:

- the Canny approach [25] to extract a line. This method consists of the following main steps:
    1. Convolution with Gaussian filter coefficient
    2. Convolution with Canny filter for horizontal and vertical orientation
    3. Calculating directions using atan2
    4. Thresholding

- the Sobel filter [26] to obtain a gradient map. This method consists of the following main steps:
    1. Convolution with two matrices to compute the derivative along x and y
    2. Computing the gradient magnitude

The extracted contour can be then cross-correlated with a reference to validate the geolocation error using the fast normalized cross-correlation (FNC) function $\gamma(u,v)$:

$$\gamma(u,v) = \frac{\sum_{x,y}\left[f(x,y)-\bar{f}_{u,v}\right]\left[t(x-u,y-v)-\bar{t}\right]}{\left\{\sum_{x,y}\left[f(x,y)-\bar{f}_{u,v}\right]^2 \sum_{x,y}\left[t(x-u,y-v)-\bar{t}\right]^2\right\}^{0.5}} \quad \text{(D.1)}$$

where f is the BT image under consideration and the sum is over all pixels (x,y) under the window containing the BT template t positioned at (u,v) displacements, $\bar{t}$ and $\bar{f}$ are the means of the template and function, respectively, in the region under the template.

Picking the maximum of (u,v) it is possible to obtain the lat-lon pixel displacements then converted into shifts along x and y direction. In order to have an accuracy of about 0.1 pixel, the maximum is fitted with a polynomial of 4th order. From these pixel displacements it is possible to obtain the related latitude and longitude error and the corresponding distance error in km.

An alternative way to obtain directly a displacement with sub-pixel accuracy is to use the registration in frequency domain (RFD) technique [28]. Between FNC and RFD we expect the same results, because the only difference is that

FNC is computed in the spatial domain whereas the other one RFD is computed in the frequency domain, so that differences should only be numerical.

APPENDIX E. Parallax error correction

In case of high-altitude targets, we have parallax error as shown in Fig. 3.1.2. In these cases the coordinates, provided by SSMIS F17 on WGS84 ellipsoid, must be corrected by finding the intersection between the line-of-sight of the satellite and the orography described by the DEM. The line of sight is the black line in Fig. E.1, joining the satellite position (red marker in Fig. E.1) and the footprint on WGS84 (magenta marker in Fig. E.1).

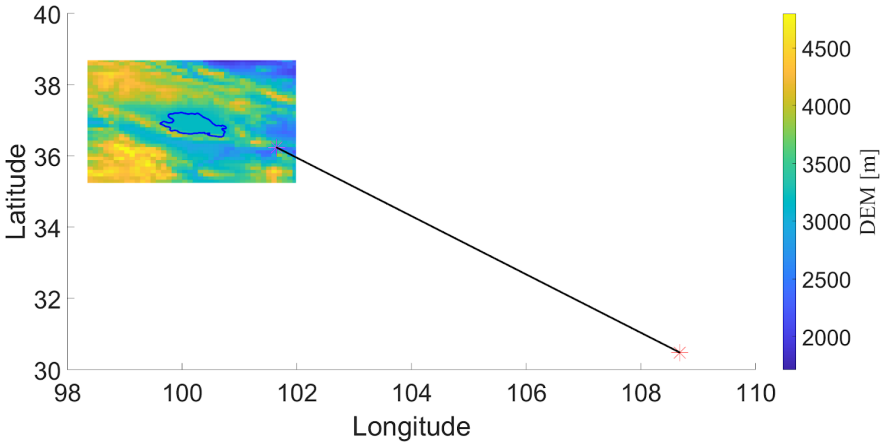

Figure E.1: Digital elevation model with spatial resolution of about 10 km over Qinghai lake. Red marker represents the satellite position and magenta marker indicates the footprint. Blue line is Qinghai lake obtained from GSHHG shoreline database.

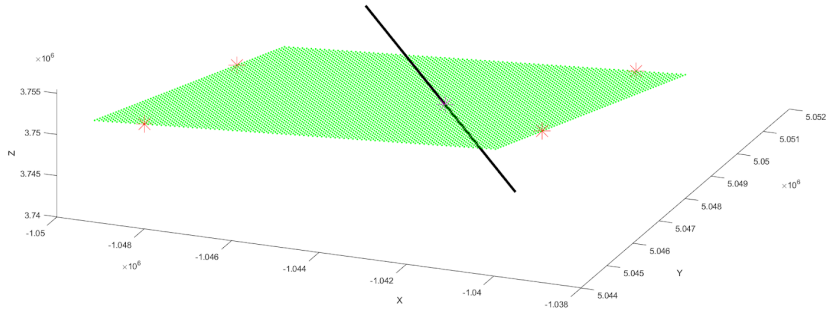

Figure E.2: The four red markers are DEM points with resolution of about 10 km. Green markers are the surface generated from DEM points. Black line is the line of sight and the magenta point is the intersection, that is the corrected coordinates.

True coordinates are provided by its intersection with the surface generated by the nearest four points of DEM, as shown in Fig. E.2. To better represent the size of footprint, we had used a DEM averaged at about 10 km.

This correction is made for each pixel of the radiometric image, as shown in Fig. E.3.

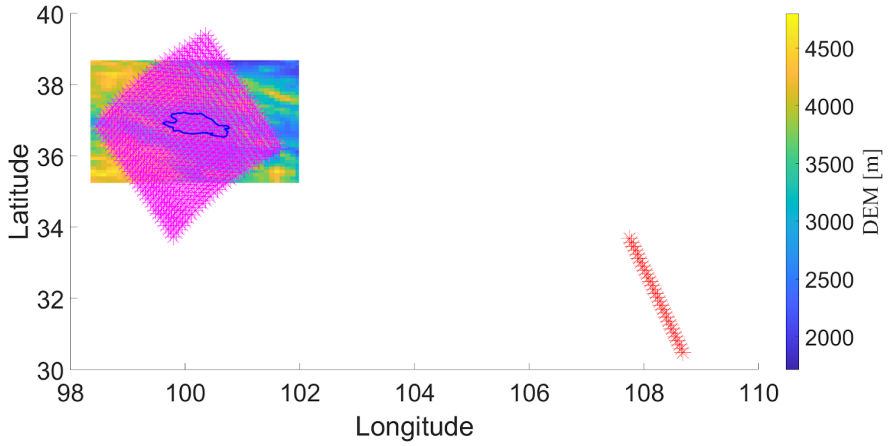

Figure E.3: The red markers indicate the satellite positions. Magenta markers represent the radiometric footprint.

After this correction the image is shifted, depending on ascending or descending orbit and the position of the target in the satellite swath.

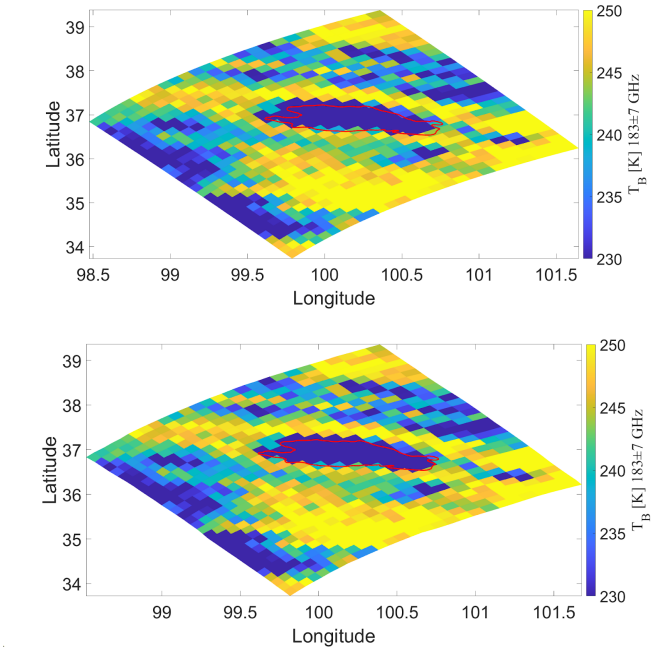

Figure E.4: In the left there is the original image (it contains parallax error) and in the right there is the corrected image.

Fig. E.4 contains an example of parallax error correction. As shown in Fig. E.3, in this example we have an ascending orbit and the target is in the left part of the swath. In this case, after the parallax error correction, the image is shifted in the south-east direction (according to line of sight direction).

APPENDIX F. Threshold for cloud-masking fuzzy-logic algorithm

To establish the threshold for $M_2(\varepsilon)$, we have considered the pixel dimension that is about 13 x 16 km^2 in case of SSMIS F17 1876.6 GHz. We can then expect a geolocation accuracy lower than this value and we had decided to put 15 km as a threshold for $M_2(\varepsilon)$ for all targets. To establish the threshold for $M_1(\Delta T_{Bm})$, we have observed the BT contrast for several targets. For example, considering the Ross ice shelf, that has 2324 samples along 2016, with BT contrast shown in Fig. F.1.

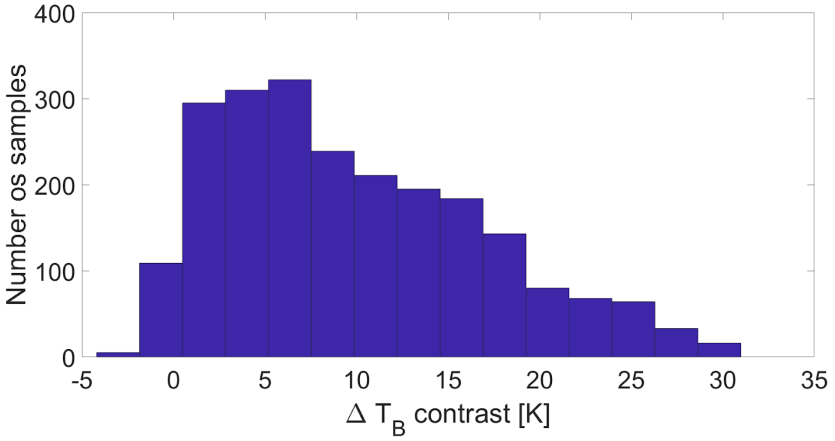

Figure F.1: ΔT_{Bm} for Ross ice shelf considering all 2324 samples

Then we have removed all images with negative value of ΔT_{Bm}, reducing the dataset to 2206 samples, as shown in Fig. F.2.

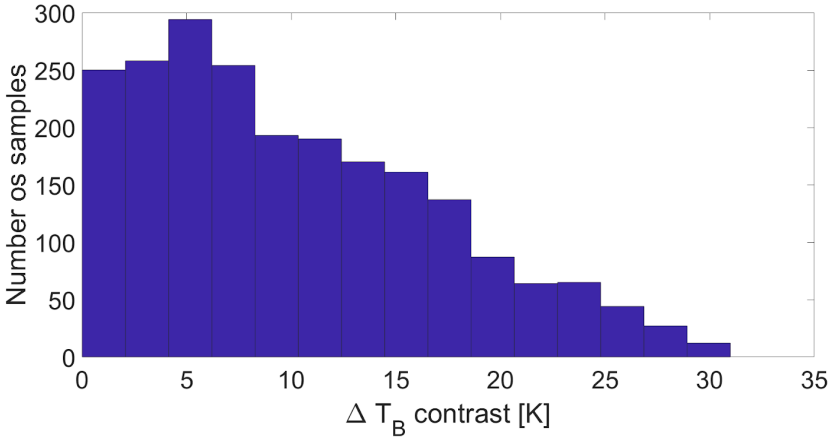

Figure F.2: ΔT_{Bm} for Ross ice shelf considering all samples with positive value of ΔT_{Bm}

Then we have applied the fuzzy-logic approach only with 0, reducing the dataset to 1349 samples with ΔT_{Bm} values shown in Fig. F.3

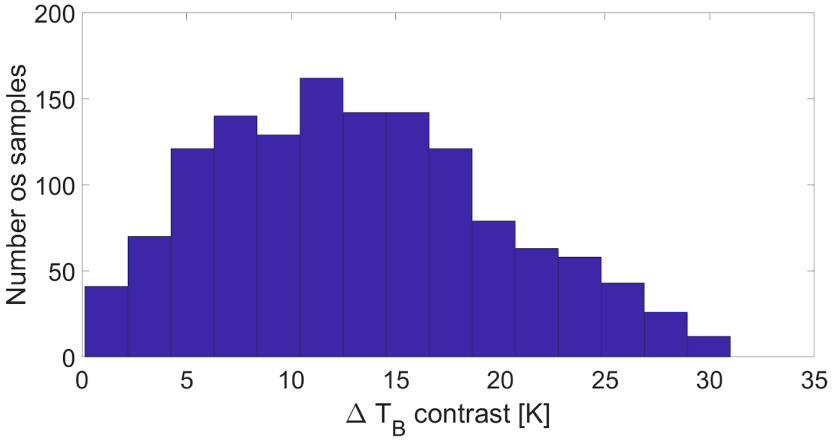

Figure F.3: ΔT_{Bm} for Ross ice shelf after defuzzification considering only $M_2(\varepsilon)$

To choose the threshold on $M_1(\Delta T_{Bm})$, we took the central value, obtaining 15 K. A similar approach it was made for other targets.

LIST OF ACRONYMS

ANN	Artificial Neural Network
AMSU	Advanced Microwave Sounding Unit
ATMS	Advanced Technology Microwave Sounder
BT	Brightness Temperature
DEM	Digital Elevation Model
EM	Electromagnetic
FNC	Fast Normalized Cross-correlation
FR	Full Resolution
GRD	Ground Range Detected
GSHHG	Global Self-consistent, Hierarchical, High-resolution Geography database
HR	High Resolution
ICI	Ice Cloud Imager radiometer
MHS	Microwave Humidity Sounders
MR	Medium Resolution
NOAA	National Oceanic and Atmospheric Administration
RAOB	RAwinsonde OBservation
RFD	Registration in Frequency Domain
SAR	Synthetic Aperture Radar
SNAP	Sentinel Application Platform
SNPP	Suomi National Polar-orbiting Partnership
SSMIS	Special Sensor Microwave Imager Sounder
SUR	Sapienza University of Rome
TCM	Target Contour Matching
TELSEM2	Tool to Estimate Land.Surface Emissivities at Microwave version 2
TESSEM2	Tool to Estimate Sea Surface Emissivities at Microwave version 2
TOA	Top Of Atmosphere
WVS II	Vector Shoreline Data Bank II

BIBLIOGRAPHY

[1] V. Mattioli, Accadia, C., Ackermann, J., Di Michele, S., Hans, I., Schlüssel, P., Colucci, P, and Canestri, A. " The EUMETSAT Polar System-Second Generation (EPS-SG) Passive Microwave and Sub-mm Wave Missions", Proc. of PhotonIcs & Electromagnetics Research Symposium-Spring (PIERS), 17-20 June 2019, Rome (Italy), pp. 3926-3933, 2019.

[2] P. Eriksson, Rydberg, B., Mattioli, V., Thoss, A., Accadia, C., Klein, U., and Buehler, S. A.: Towards an operational Ice Cloud Imager (ICI) retrieval product, Atmos. Meas. Tech., 13, 53–71, https://doi.org/10.5194/amt-13-53-2020, 2020.

[3] C. Accadia et al. (2020), Microwave and Sub-mm Wave Sensors: A European Perspective. In: Levizzani V., Kidd C., Kirschbaum D., Kummerow C., Nakamura K., Turk F. (eds) Satellite Precipitation Measurement. Advances in Global Change Research, vol 67. Springer.

[4] K. F. Evans and G. L. Stephens, "Microwave radiative transfer through clouds composed of realistically shaped ice crystals. Part I: Single scattering properties," J. Atmos. Sci. 52, pp. 2041–2057, 1995.

[5] K. F. Evans and G. L. Stephens, "Microwave radiative transfer through Clouds Composed of Realistically Shaped Ice Crystals. Part II. Remote Sensing of Ice Clouds," J. Atmos. Sci. 52, pp. 2058–2072, 1995.

[6] K. F. Evans, K. F., S. J. Walter, A. J. Heymsfield, and M. N. Deeter, "Modeling of Submillimeter Passive Remote Sensing of Cirrus Clouds," J. Appl. Meteorol. 37, pp. 184–205, 1998.

[7] S. A. Buehler et al., "A concept for a satellite mission to measure cloud ice water path and ice particle size," Q. J. R. Meteorol. Soc. 133(S2), pp. 109-128, 2007.

[8] S. A. Buehler et al., "Observing ice clouds in the submillimeter spectral range: the CloudIce mission proposal for ESA's Earth Explorer 8," Atmos. Meas. Tech. 5, pp. 1529-1549, 2012.

[9] W. E. Purdy et al., "Geolocation and pointing accuracy analysis for the WindSat sensor," IEEE Trans. Geosci. Remote Sens., vol. 44, no. 3, pp. 496-505, March 2006.

[10] G. A. Poe , E. A. Uliana, B. A. Gardiner, T. E. vonRentzell, and D. B. Kunkee, "Geolocation error analysis of the special sensor microwave imager/sounder," IEEE Trans. Geosci. Remote Sens., vol. 46, no. 4, pp. 913-922, April 2008.

[11] H. Wiebe, G. Heygster, and L. Meyer-Lerbs : Geolocation of AMSR-E data, IEEE Trans. Geosci. Remote Sens., 46 (10), pp. 3098-3103, doi : 10.1109/TGRS.2008.919272, 2008.

[12] G. Heygster, H. Wiebe, G. Spreen , and L. Kaleschke, "AMSR-E geolocation and validation of sea ice concentrations based on 89 GHz Data," J. Remote Sens. Soc. Jpn., vol. 29, no. 1, pp. 226-235, January 2009.
[13] W. Berg, M. R. P. Sapiano, J. Horsman, and C. Kummerow, "Improved geolocation and Earth incidence angle information for a fundamental climate data record of the SSM/I sensors," IEEE Trans. Geosci. Remote Sens., vol. 51, no. 3, pp. 1501-1513, March 2013.
[14] T. Bellerby et al., "Retrieval of land and sea brightness temperatures from mixed coastal pixels in passive microwave data," in IEEE Transactions on Geoscience and Remote Sensing, vol. 36, no. 6, pp. 1844-1851, Nov. 1998, doi: 10.1109/36.729355.
[15] Moradi, H. Meng, R. R. Ferraro, and S. Bilanow, "Correcting geolocation errors for microwave instruments aboard NOAA satellites," IEEE Trans. Geosci. Remote Sens., vol. 51, no. 6, pp. 3625-3637, June 2013.P.
[16] R. Bennartz, “On the use of SSM/I data in coastal regions. J. Atmos. Ocean Technol.”, 16, 417-431, 1999.
[17] Y. Han, F. Z. Weng, X. L. Zou, H. Yang, and D. Scott, ”Characterization of geolocation accuracy of Suomi NPP Advanced Technology Microwave Sounder measurements”, J Geophys Res-Atmos, 121(9), 4933-495010.1002/2015jd024278, 2016.
[18] C. Prigent, F. Aires, D. Wang, S. Fox and C. Harlow, “Sea-surface emissivity parametrization from microwaves to millimetre waves”, Q.J.R. Meteorol. Soc., vol. 143, pp. 596-605. doi:10.1002/qj.2953, 2017.
[19] Ulaby F.T., R. K. Moore, A. K. Fung, “Microwave remote sensing – Active and passive, Volume I: Microwave remote sensing – fundamentals and radiometry”, 1981.
[20] Marzano F. S., L. Pulvirenti, “Corso di propagazione elettromagnetica”, La Sapienza University of Rome, Dipartimento di Ingegneria dell’Informazione, Elettronica e Telecomunicazioni (DIET).
[21] Pierdicca N., “Telerilevamento a Microonde”, La Sapienza University of Rome, Dipartimento di Ingegneria dell’Informazione, Elettronica e Telecomunicazioni (DIET).
[22] Marzano F. S., N. Pierdicca: “Fondamenti di Antenne: Radiazione elettromagnetica e applicazioni”, Carocci 2011.
[23] Skou, N., 1989, Microwave radiometer systems: Design and analysis, Artech House.
[24] P. Wessel and W. H. F. Smith, "A global self-consistent, hierarchical, high-resolution geography database (GSHHG)," J. Geophys. Res., vol. 101, no. B4, pp. 8741-8743, April 1996.

[25] J. Canny, "A computational approach to edge detection," IEEE Transactions on pattern analysis and machine intelligence, vol. 8, no. 6, pp. 679-698, November 1986.
[26] Gupta, Samta, and Susmita Ghosh Mazumdar. "Sobel edge detection algorithm." International journal of computer science and management Research 2.2, 1578-1583, 2013.
[27] J. P. Lewis, “Fast Template Matching”, Vision Interface, p. 120-123, 1995.
[28] R.H. Thomas, D.R. MacAyeal, D.H. Eilers, and D.R. Gaylord, 1984. Glaciological Studies on the Ross Ice Shelf, Antarctica, 1972-1978. The Ross Ice Shelf: Glaciology and Geophysics Antarctic Research Series, Volume 42, Paper 2, 21-53.
[29] Manuel Guizar-Sicairos, Samuel T. Thurman, and James R. Fienup, "Efficient subpixel image registration algorithms," Opt. Lett. 33, pp. 156-158, 2008.
[30] Kunkee, David B., et al. "Design and evaluation of the first special sensor microwave imager/sounder." IEEE Transactions on Geoscience and Remote Sensing 46.4, pp. 863-883, 2008.
[31] Beck, H. E., Zimmermann, N. E., McVicar, T. R., Vergopolan, N., Berg, A., & Wood, E. F. “Present and future Köppen-Geiger climate classification maps at 1-km resolution. Scientific data”, 5, 180214, 2018
[32] M. Papa, V. Mattioli, J. Avbelj, and F. S. Marzano, “Geocalibrating Millimeter-wave Spaceborne Radiometers for Global-scale Cloud Retrieval”, Proc. of PhotonIcs & Electromagnetics Research Symposium-Spring (PIERS), 17-20 June 2019, Rome (Italy), pp. 2193-2197, 2019.
[33] M. Papa, V. Mattioli, J. Avbelj, and F.S. Marzano, “Assessing the Spaceborne 183.31-GHz Radiometric Channel Geolocation Using High-Altitude Lakes, Ice Shelves, and SAR Imagery.”, IEEE Transactions on Geoscience and Remote Sensing, doi: 10.1109/TGRS.2020.3024677, 2020.